2nd International Natural Science, Engineering and Material Technologies Conference
Sep 15-17, 2022, İğneada-Kırklareli / TÜRKİYE

ISBN: 978-605-68918-2-3

NEM 2022

FULL TEXT BOOK

2 nd International Natural Science, Engineering and Material Technologies Conference

(NEM 2022)

Sep 15-17, 2022 – İğneada-Kırklareli/ TÜRKİYE

FOREWORD

It is a pleasure for us to offer you this Book of Abstract for the 2 nd International Natural Science, Engineering and Material Technologies Conference (NEM 2022). Our goal was to create a platform that introduces the newest results on internationally recognized experts to local students and colleagues and simultaneously displays relevant Turkish achievements to the world. The positive feedback of the community encouraged us to proceed and transform a single event into a conference series. Now, NEM 2022 is honored by the presence of over 120 colleagues from various countries. We stayed true to the original NEM 2022 concept and accepted contributions from all fields of materials science and technology to promote multidisciplinary discussions. The focal points of the conference emerged spontaneously from the submitted abstracts: energy applications, advanced materials, electronic and optoelectronic devices, organic electronic materials, chemistry, physics, environmental science, medical science, applied and engineering science, computer simulation of organic structures, biomedical applications and advanced characterization techniques of nanostructured materials. Further fields of interest include e.g. new advanced and functional materials, advanced-functional composites, biomaterials, smart materials, dielectric materials, optical materials, magnetic materials, organic semiconductors, inorganic semiconductors, electronic materials, graphene, and more.

Therefore, we hope that getting first-hand access to so many new results, establishing new connections and enjoying the İğneada-Kırklareli/ TÜRKİYE ambience will make you feel that your resources were spent well in NEM 2022.

Our warmest thanks go to all invited speakers, authors, and contributors of NEM 2022 for accepting our invitation, visiting Kırklareli and using NEM 2022 as a medium for communicating your research results.

We hope that you will enjoy the conference and look forward to meeting you again in one of the forthcoming **NEM 2023** event.

Best regards,
Chairmen's of Conference

Assoc. Prof. Burhan COŞKUN

Prof. Dr. Fahrettin YAKUPHANOĞLU

Editor:

Assoc. Prof. Burhan COŞKUN

Published, October-2022

nem2022.klu.edu.tr

nem@klu.edu.tr

COMMITTEE

HONORARY PRESIDENT

Prof. Dr. Bülent ŞENGÖRÜR (Rector of Kırklareli University)

Prof. Dr. Erhan TABAKOĞLU (Rector of Trakya University)

- Prof. Dr. Mümin ŞAHİN (Rector of Tekirdağ Namık Kemal University)

Prof. Dr. Sedat MURAT / Rector of Çanakkale Onsekiz Mart University

Prof. Dr. Süleyman ÖZDEMİR / Rector of Bandırma Onyedi Eylül University

CONFERENCE PRESIDENT

Prof. Dr. Fahrettin YAKUPHANOĞLU (Fırat University)

Prof. Dr. Meryem ÇAMUR DEMİR (Kırklareli University)

Prof. Dr. Serpil AKÖZCAN (Kırklareli University)

Assoc. Prof. Burhan COŞKUN (Kırklareli University)

ORGANIZING COMMITTEE

Prof. Dr. Aydın ULUBEY / Trakya University

Prof. Dr. Bülent EKER / Tekirdağ Namık Kemal University

Prof. Dr. Feyzullah TEMURTAŞ / Bandırma Onyedi Eylül University

Prof. Dr. Hatice ŞANLIDERE ALOĞLU / Kırklareli University

Prof. Dr. Murat TÜRKYILMAZ / Trakya University

Prof. Dr. Okhan AKDUR / Çanakkale Onsekiz Mart University

Prof. Dr. Sermet KOYUNCU / Çanakkale Onsekiz Mart University

Asst. Prof. Dr. Muhammet ATALAY / Trakya Üniversiteler Birliği Secretary General

Assoc. Prof. Dr. Ayşegül DERE / Fırat University

Assoc. Prof. Dr. Berna AKGENÇ HANEDAR / Kırklareli University

Assoc. Prof. Dr. Cemile ÖZCAN / Kırklareli University

Assoc. Prof. Dr. Emel PELİT / Kırklareli University

Assoc. Prof. Dr. Fatma KURŞUN BAYSAK / Kırklareli University

Assoc. Prof. Dr. H. Hale KARAYER / Kırklareli University

Assoc. Prof. Dr. Mehmet Mümin KOÇ / Kırklareli University
Assoc. Prof. Dr. Mustafa ARSLAN / Kırklareli University
Assoc. Prof. Dr. Nurdan KURNAZ YETİM / Kırklareli University
Assoc. Prof. Dr. Ümit GÜLYÜZ / Kırklareli University
Dr. Nihat AKKURT / Kırklareli University
Dr. Osman ÜNER / Kırklareli University
Dr. Selin ÖZDEN / Kırklareli University
Dr. Ufuk PAKSU / Kırklareli University

SCIENTIFIC COMMITTEE

Prof. Dr. Abdel Salam Hamdy MAKHLOUF / University of Texas / UNITED STATES
Prof. Dr. Abdullah G. AL-SEHEMI / King Khalid University / SAUDI ARABIA
Prof. Dr. Ahmed A. ALGHAMDI / King Abdulaziz University / SAUDI ARABIA
Prof. Dr. Ali DİŞLİ / Gazi University / TÜRKİYE
Prof. Dr. Asa H. BARBER / London South Bank University / UNITED KINGDOM
Prof. Dr. Azar AHMADOV / Baku State Gazi University / AZERBAIJAN
Asst. Prof. Bahadır BEKAR / Trakya University / TÜRKİYE
Assoc. Prof. Dr. Bayram ÇETİN / Kırklareli University / TÜRKİYE
Prof. Dr. Bekir SARI / Gazi University / TÜRKİYE
Prof. Dr. Burç MISIRLIOĞLU / Sabancı University / TÜRKİYE
Prof. Dr. Canan AKSU CANBAY / Fırat University / TÜRKİYE
Prof. Dr. Chung GWIY-SANG / Ulsan University / KOREA
Prof. Dr. Denis NIKA / Moldova University / MOLDOVA
Prof. Dr. Dilek NARTOP / Düzce University / TÜRKİYE
Prof. Dr. Elias STATHATOS / Tecnological-Educational Institute of Patras / GREECE
Prof. Dr. Elizabeth BLACKBURN / University of Birmingham / UNITED KINGDOM
Asst. Prof. Erdinç KESKİN / Kırklareli University / TÜRKİYE
Asst. Prof. Evren ÇAĞLAER / Kırklareli University / TÜRKİYE
Assoc.Prof. Harun URAN / Kırklareli University / TÜRKİYE
Prof. Dr. Hatice ÖĞÜTCÜ / Kırşehir Ahi Evran University / TÜRKİYE

Asst. Prof. İsmail KILIÇ / Kırklareli University / TÜRKİYE

Asst. Prof. Macide CANTÜRK RODOP / Yıldız Technical University / TÜRKİYE

Prof. Dr. Müjdat ÇAĞLAR / Eskişehir Anadolu University / TÜRKİYE

Prof. Dr. Mustafa ERKOVAN / Beykoz University / TÜRKİYE

Assoc. Prof. Mustafa KURBAN / Ahi Evran Gazi University / TÜRKİYE

Prof. Dr. Niyazi ÖZDEMİR / Fırat University / TÜRKİYE

Prof. Dr. Numan AKDOĞAN / Gebze Technical University / TÜRKİYE

Prof. Dr. Nurşen SARI / Gazi University / TÜRKİYE

Assoc. Prof. Ömer Suat TAŞKIN / Istanbul University / TÜRKİYE

Prof. Dr. Ram K. GUPTA / Pittsburg State University / UNITED STATES

Prof. Dr. Raşit TURAN / Middle East Technical University / TÜRKİYE

Prof. Dr. S. MANSOURI / University of Gabès / TUNUSIA

Asst. Prof. Sena Esen BAYER KESKİN / Kırklareli University / TÜRKİYE

Asst. Prof. Sencer Süreyya KARABEYOĞLU / Kırklareli University / TÜRKİYE

Assoc. Prof. Taner DAŞTAN / Cumhuriyet University / TÜRKİYE

Assoc. Prof. Tarık ASAR / Gazi University / TÜRKİYE

Prof. Dr. W. Aslam FAROOQ / King Saud University / SAUDI ARABIA

Prof. Dr. Yasemin BAKIRCIOĞLU KURTULUŞ / Trakya University / TÜRKİYE

Assoc. Prof. Yashar Azizian KALANDARAGH / University of Mohaghegh Ardabili / IRAN

Dr. Zöhre GÖRÜNMEZ GÜNGÖR / Kırklareli University / TÜRKİYE

FULL TEXT PRESENTATIONS

2nd International Natural Science, Engineering and Material Technologies Conference
Sep 15-17, 2022, İğneada-Kırklareli / TÜRKİYE

FLOW VISUALIZATION EXPERIMENTS OF STOKES FLOW IN A V-SHAPED CHANNEL

E. F. Kent

Department of Thermodynamics, Faculty of Mechanical Engineering, Istanbul Technical University, Gümüşsuyu, İstanbul, TÜRKİYE

E-mail: kente@itu.edu.tr

Abstract

In this work, flow visualization experiments of cellular Stokes flow induced by rotation of a circular cylinder in a V shaped channel bounded by a cylindrical surface have been performed. The source of motion in the channel is the inner rotating cylinder positioned at the center of the cylindrical surface, as well as at different locations inside this channel. Many interesting flow patterns have been visualized using solid tracers of magnesium illuminated by a thin sheet of light coming from a laser device by means of long time exposure photography. Some quantitative data have been deduced from these visualization photographs.

Keywords: Stokes flow, flow visualization, V-shaped channel

1. INTRODUCTION

In this work, flow visualization experiments of cellular Stokes flow in a V shaped channel bounded by a cylindrical surface have been performed. Many problems of physical interest involve the flow of fluids at low Reynolds numbers, i.e., Stokes flow. Much work has been devoted the study of cavity flow, to separation phenomena and to viscous cells. The most studied case is naturally a cavity of a rectangular shape. Due to its simple geometry, this problem serves also as a test case for numerical algorithms. This type of flow in which viscous cells occur is important not only from a fundamental point of view, i.e., academic interest, but is encountered in many practical applications, cited in [1-3]. The first two considered the cavity flow driven by an external stream while the latter investigated thermocapillary effects in liquid bridges and the flow driven by surface traction. In addition to enormous numerical investigations, experimental observations of the streamlines were recorded by [4] and [5]. The former used a flat belt arrangement and the latter a circular drum for the driven surface. For three-dimensional representations of the lid-driven cavity flow, there is a very interesting report by [6] in which the cavity has been taken as a test for the numerical calculations and the corresponding experiments as a reference. [7] also examined the three-dimensional lid-driven cavity flow. [8] and [9] studied numerically and experimentally the cellular structure of the two-dimensional creeping flow induced by rotation of a circular cylinder set in the center of a rectangular channel.

Although the rectangular cavity flow has been investigated extensively, very few papers have been published on the subject of the triangular cavity. It is worth to note that triangular cavity is more common in practice than rectangular cavity. The practical applications of the triangular grooves are described by [10], who investigated numerically steady recirculating viscous flow inside an equilateral triangular cavity generated by translating one side. [11] numerically investigated the steady and oscillating axisymmetric laminar flows through a straight concertina-shaped tube with application to arterial prostheses. The interested reader may refer to [2] for further practical applications in the industrial environment and in natural systems where low-Reynolds number flows are important in quite arbitrary geometries. On the other hand, from the experimental point of view, the gap in the literature is more serious. There is one visualization photograph of Taneda [12], who visualized the first two cells in the flow confined by two 28‘ 5' intersecting planes and driven by a rotating cylinder at the fluid surface. A comparison of visualization of Stokes flow in a V-shaped and rectangular channel was given by [13] and in a V-shaped channel bounded by a cylindrical surface was

given by [14]. This is the main motivation to conduct a flow visualization experiment in a V shaped channel. To this end, a special V-shaped channel bounded by a cylindrical surface has been constructed. The inner rotating cylinder which induces the motion is positioned at the at the center of the cylindrical surface, as well as at different locations inside this channel and flow visualization photographs have been obtained by means of long time exposure photography.

2. EXPERIMENTAL SET-UP AND METHOD

The sketch of the apparatus constructed to visualize the flow and horizontal cross-section of the channel is shown in Figure 1a and 1b, respectively.

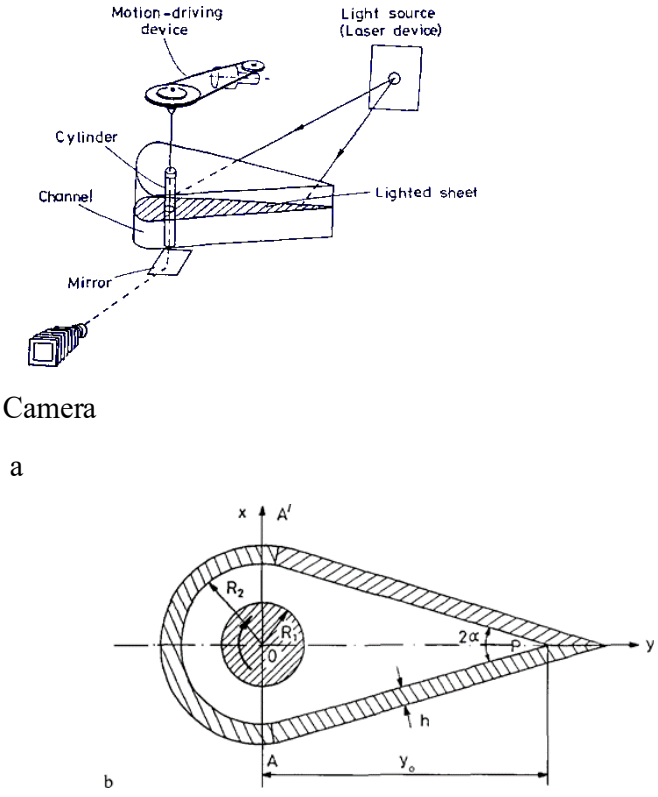

Figure 1. Sketch of the apparatus and the horizontal cross-section of the channel.

This special geometry of the outer boundary of the vchannel permits to investigate both the flow in the wedge and in the circular cavity and has only one sharp corner at P. The cylindrical surface and wedge are matched at A and A'. So there are no sharp corners at A and A'. In the experiments, the rotating cylinder which

induces the motion is positioned at the center of the cylindrical surface O and at different locations along the y-axis. The location of the cylinder at different positions inside the channel also enables to determine the effects of the outer geometry on the cellular flow structure. The radius of the inner rotating cylinder R_1 and the cylidrical surface R_2 are 1 cm and 2 cm, respectively. The distance y_o between the center of the outer cylindrical surface and the corner is 7.5 cm. The wedge angle 2α is 30 °. The thickness h of the Altuglass used to construct the channel is 0.5 cm. This channel is filled with a highly viscous silicon oil of viscosity $\nu = 300$ cm^2/s. The motion is induced by a very slow rotation of a circular cylinder positioned in the channel at a constant rotational speed of $n = 3$ min^{-1}. Thus the Reynolds number of the flow, defined by $Re = (w_o R_1^{\,2})/\nu$, was about 0.001.

The purpose of this work is to show the detailed flow structure experimentally in a V-shaped channel. This is realized experimentally by a flow visualization technique. Flow visualization experiments are carried out using solid tracers of magnesium of about 40 µm in length and 4 µm in thickness. They are illuminated by a thin sheet of light coming from a laser device. By means of very long time exposure photography, we obtain the flow visualization photographs.

3. EXPERIMENTAL RESULTS

In the first experiment, the inner rotating cylinder was positioned at the center of the cylindrical surface. The visualization photograph by means of very long time exposure is presented in Figure 2.

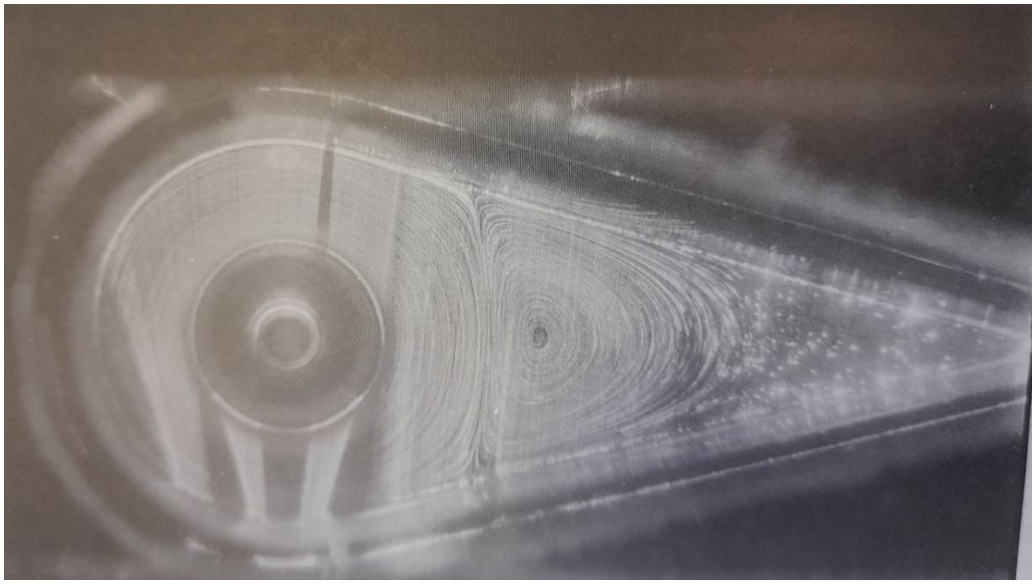

Figure 2. The visualization photograph, the cylinder was positioned at the center of the cylindrical surface.

The streamlines of the main flow, i. e., the flow directly driven by the rotation of the cylinder and the first cell which occurred beyond the main flow visualized in the wedge. The streamlines of the main flow are circular near the inner cylinder, but the outer wedge-shaped channel walls affect the flow near the separating line. It is worth to note that no separation is detected in the circular cavity.

In figure 3 the inner rotating cylinder was positioned 2 cm ahead along the symmetry axis towards the corner from its central position. There is a large recirculating eddy filling much of the circular cavity. Both the upper and lower separating streamlines are located at 1.5 R_1 (measured along the symmetry axis) from the center of the inner rotating cylinder.

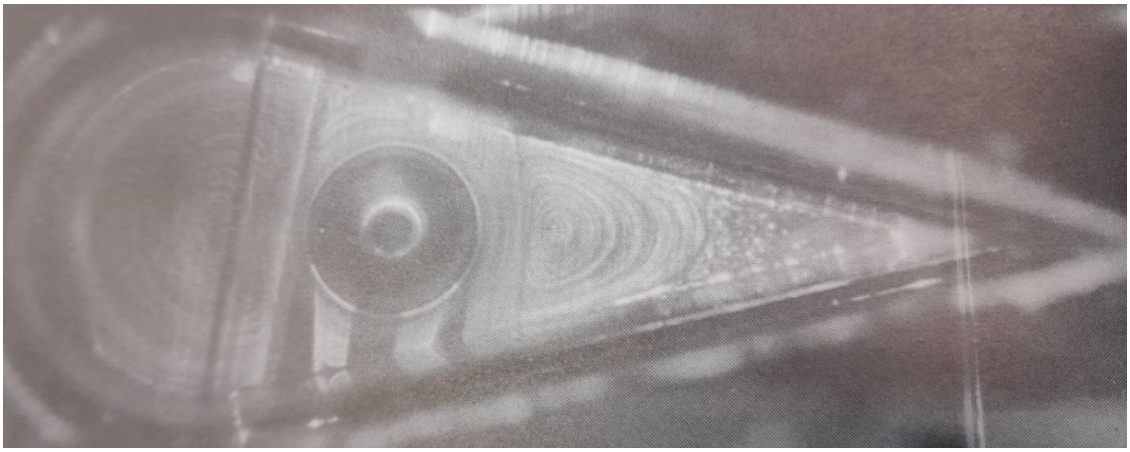

Figure 3. The visualization photograph, the cylinder was positioned 2 cm ahead towards the corner from its central position.

In Figure 4, the cylinder was positioned 1 cm ahead towards the corner from its central position.

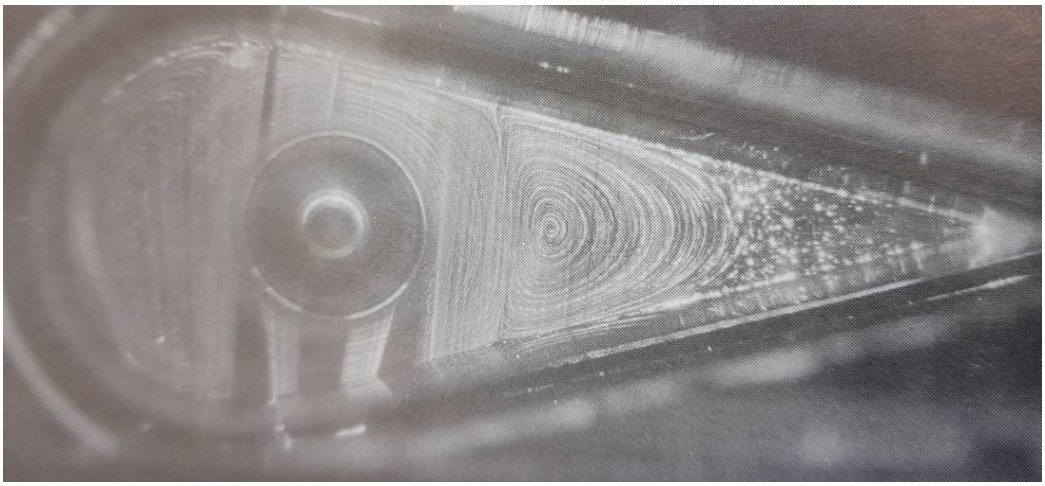

Figure 4. The visualization photograph, the cylinder was positioned 1 cm ahead towards the corner from its central position.

In this case, a cellular motion is observed in the circular cavity abovr the rotating cylinder. The upper and lower saparating streamlines are located at 2.18 R1 and 1.9 R_1 (measured along the symmetry axis) from the center of the inner rotating cylinder, respectively.

3. CONCLUSIONS

Flow visualization experiments of cellular Stokes flow induced by rotation of a circular cylinder in a V shaped channel bounded by a cylindrical surface have been carried out by means of long time exposure photography. The inner rotating cylinder which induces the motion is positioned at the at the center of the cylindrical surface, as well as at different locations inside this channel. The special geometry of the outer boundary of the channel permits to investigate both the flow in the wedge and in the circular cavity. It has been experimentally verified that the flow in the circular cavity is very sensitive to the cavity depth. No separation is detected in the circular cavity fot the central position of the inner rotating cylinder, a small recirculating eddy is seen in the circular cavity as the cylinder is placed 1 cm ahead towards the corner, and a large recirculating eddy fills much of the entire the circular cavity wnen the cylinder is placed 2 cm ahead towards the corner.

ACKNOWLEDGMENTS

The experiments in this work were carried out at the Laboratory of Fluid Mechanics of the Poitiers University in France. The author would like to thank Professor M. Coutanceau for her useful advice and interest, as well as Dr. M. Hajjam for interesting discussions during the research. The author received financial support from The Scientific and Technical Research Council of Turkey (TUB- ITAK) during the study at the Laboratory of Fluid Mechanics of the Poitiers University in France.

REFERENCES

[1] Shen, C. and Floryan, J. M., Low Reynolds number flow over cavities, Physics of. Fluids 28, 3191-3202, 1985.

[2] Higdon, J. J. L., Stokes flow in arbitrary two dimensional domains: shear flow over ridges and cavities, Journal of Fluid Mechanics, 159, 195-226, 1985.

[3] Rybicki, A. and Floryan J. M., Thermocapillary effects in liquid bridges. I. Thermocapillary convection, Physics of. Fluids 30, 1956-1972, 1987.

[4] Mills, R. D., On the closed motion of a fluid in a square cavity, J. Roy. Aerosol. Soc. 69, 116-120., 1965.

[5] Pan, F. and A. Acrivos A., Steady flows in rectangular cavities, Journal of Fluid Mechanics, 28, 643-660, 1967.

[6] Deville, M., Le, T. H. and Y. Morshoisne, Y., (Eds.), Numerical simulation of 3-D incompressible unsteady viscous laminar flows, GAMM Workshop, 1992.

[7] Koseff, J.R. and R.L. Street, R. L., (1984) The lid-driven cavity flow: A synthesis of qualitative and quantitative observations, Journal of Fluid Engineering, 106, 390 398, 1984.

[8] Hellou, M. (1988) Etude numerique et experimentale de l'ecoulement a structure cellulaire, engendre par la rotation d'un cylindre dans un canal, These de l'Université de Poitiers, 1988.

[9] Hellou, M. and M. Coutanceau, M., (1992) Cellular Stokes flow induced by rotation of a cylinder in a closed channel, Journal of Fluid Mechanics 236, 557-577, 1992.

[10] Ribbens, C.J., Watson L. T. and Wang, C. Y., Steady viscous flow in a triangular cavity, J. Computational Physics 112, 173-181, 1994.

[11] Savvides, C. N. and Gerrard, J.H., Numerical analysis of the flow through a corrugated tube with application to arterial prostheses, Journal of Fluid Mechanics 138, 129-160, 1984.

[12] Taneda, S., Visualization of separating Stokes flow, Journal of the Physical Society of Japan 49, 1935-1942, 1979.

[13] Kent, E. F., A comparison of visualization of Stokes flow in a V-shaped and rectangular channel, Fluid Dynamics Research 18, 307-312, 1996.

[14] Kent, E. F., Flow visualization experiments in a V-shaped channel bounded by a cylindrical surface, Journal of the Physical Society of Japan 68 (6), 1887-1890, 1999.

2nd International Natural Science, Engineering and Material Technologies Conference
Sep 15-17, 2022, İğneada-Kırklareli / TÜRKİYE

CHAIN TYPE TORQUE TRANSMISSION SYSTEM DESIGN FOR A HYBRID ELECTRIC VEHICLE

A. T. Ergenç[1], Ö. Işın[1], D. Yıldız[1], H. Arıkan[1], M. Kabakçı[1], S. Bektaş[2], H. Aslan[1], M. Tufan[1]

[1]*Department of Mechanical Engineering, Yıldız Technical University, İstanbul, TÜRKİYE*
[2]*Department of Mechatronic Engineering, Yıldız Technical University, İstanbul, TÜRKİYE*

E-mail: aergenc@yildiz.edu.tr

Abstract

The effects of global warming have led to emission restrictions on land vehicles, and researchers are working hard to reduce the CO_2 production per kilometer of internal combustion engines. This situation brings hybrid vehicles to the forefront and studies in this field are increasingly continuing. Power transmission in hybrid vehicles is basically carried out in three different ways: serial hybrid, parallel hybrid and power split.

In hybrid powertrain systems, the internal combustion engine can either contribute directly to the powertrain or operate independently. The important thing at this point is to ensure that both the internal combustion engine and the electric motor transmit the torque to the gearbox or directly to the wheels without any problems.

In this study, the transmission of torque from the electric motor to the gearbox is carried out with a chain gear mechanism. In this system, instead of the traditional clutch, electromagnetic powder clutch, in which partial clutch and full clutch can be controlled by electronic signals, is used in the transmission of motion from the internal combustion engine to the automatic transmission. In the connection of the electric motor with the gearbox, a one-way clutch is used to transmit the motion independently of the internal combustion engine. With this clutch system, the electric motor is prevented from turning the internal combustion engine and independent power transmission is possible with both clutches.

Keywords: Hybrid, Torque transmission, electromagnetic clutch, one way clutch, chain drive.

1. INTRODUCTION

Global warming is increasing rapidly today with intense carbon emissions. In order to reduce carbon emissions, emission limits are restricted in vehicles. At this point, despite all the restrictions, the only way to meet the limit is through the use of hybrid vehicles [1, 2].

In hybrid vehicles, internal combustion engine and electric motor are used together. In some hybrid vehicles, the internal combustion engine does not directly contribute to power transmission, while in some mechanisms, the internal combustion engine can provide power transmission directly to the wheels of the vehicle [3,4,5].

Hybrid vehicles are divided into three main groups: series hybrid, parallel hybrid and power-split hybrid. In series hybrid vehicles, the internal combustion engine is used to support the electric motor. Power transmission to the wheels are provided by electric motor only. Since the internal combustion engine does not contribute directly to power transmission, it can be controlled at the most efficient point. Since the internal combustion engine does not contribute directly to power transmission, it can be controlled at the most efficient point.

Less CO_2 is produced per unit kilometer in series hybrid vehicles. However, since only the electric motor provides the vehicle's movement and energy conversions in serial hybrid vehicles, its efficiency is lower than other hybrid systems [6,7].

In parallel hybrid vehicles, both the internal combustion engine and the electric motor transmit power to the wheels and are mechanically coupled. In the parallel hybrid system, some of the power flow transmitted to the wheels can be diverted to the battery. For this reason, the parallel hybrid system is more efficient than the serial hybrid system. If your vehicle needs power, both the internal combustion engine and the electric motor provide power to the wheels. However, in parallel hybrid systems, since the internal combustion engine does not work continuously at the most efficient point, its thermal efficiency is lower and its emission value is higher [6,7].

In the power split hybrid system, the internal combustion engine and electric motors are mechanically connected to each other by a planetary gear mechanism. The internal combustion engine provides power transmission when the electric motor rotates. Both electric motors are capable of charging the battery. This type of hybrid system provide better fuel economy and electric driving efficiency [6].

2. MATERIAL AND METHODS

The aim of this study is to design a hybrid power transmission system, so that the internal combustion engine and the electric motor can transmit power to the gearbox independently of each other. In design process, choosing the chain system and one-way bearing is important for the electric motor to transmit its power to the gearbox. An electromagnetic powder clutch is used to engage the transmission to the internal combustion engine. This type of clutch transmits torque by filling the gap with the particles under the influence of the magnetic field created by the excitation current.

The gearbox input shaft is connected to the inner ring, and the engine output is connected to the outer ring. There is a certain amount of ferromagnetic iron powder between the inner ring and the outer ring. In the outer ring, there is a coil that magnetizes the ferromagnetic powders with the effect of voltage. When the amount of applied voltage is increased, the amount of torque transmitted from the engine to the gearbox increases in direct proportion [8,9].

In the real scenario, the power of the electric motor is 15 kW and the engine speed is 1500 rpm. According to the given values, firstly the length of the chain to be used for the hybrid power group design was determined. The number of links of the chain is calculated using the formula 1.1 and the length calculated using formula 1.2.

$$X = 2 * \frac{a}{p} + \frac{z_1+z_2}{2} + \left(\frac{z_2-z_1}{2*\pi}\right)^2 * \frac{p}{a} \quad (1.1)$$

$$L = X.p \quad (1.2)$$

where;

X : number of links
z_1 : number of teeth of the gear 1
z_2 : number of teeth of the gear 2
a : distance between the centers of the gears
p : knot length of the chain.

After calculating the chain length, the forces applied on the chain-gear system were found. This forces are calculated with the help of the following equations (1.3 -1.6). After calculating the total force, whether the chain-gear system is safe or not is calculated with the help of the formula 1.7

$$F_\Sigma = F_u + F_{cgf} + F_q \quad (1.3)$$

$$F_u = \frac{p}{v} \quad (1.4)$$

$$F_{cgf} = q * v^2 \quad (1.5)$$

$$F_q = 6.25 * q * g * a \quad (1.6)$$

$$S_{mev} = \frac{F_k}{K.F_\Sigma} \quad (1.7)$$

where;

F_{top} : total force acting on chain
F_u : circumferential force
F_{cgf} : centrifugal pulling force
F_q : pulling force due to the weight of the chain
F_k : maximum force acting on chain

K : operating factor

Then the forces acting on the one-way bearing are calculated. First of all, the axial (Fa) and radial (Fr) forces that will act on the bearing must be calculated. Later Fa/Co and Fa/Fr values need to be calculated. Since Fa/Fr>e, dynamic radial factor (X) and dynamic axial factor (Y) values are found. Equivalent dynamic load (F_{edl}) is found with the help of equation 1.8

$$F_{\text{edl}} = X * F_R + Y * F_a \quad (1.8)$$

The life expression in operating hours (L10h) is found with the help of equation 1.9.

$$L_{10\text{h}} = \frac{10^6}{60*n} * (\frac{C}{F_{edl}})^p \quad (1.9)$$

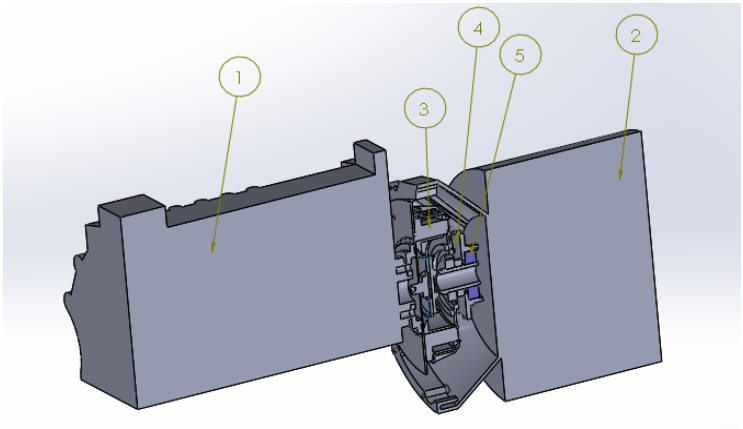

Figure 1. Consept design (1. Combustion engine, 2. Electric motor , 3. Electromagnetic powder clutch , 4. Sprocket 5. One way bearing)

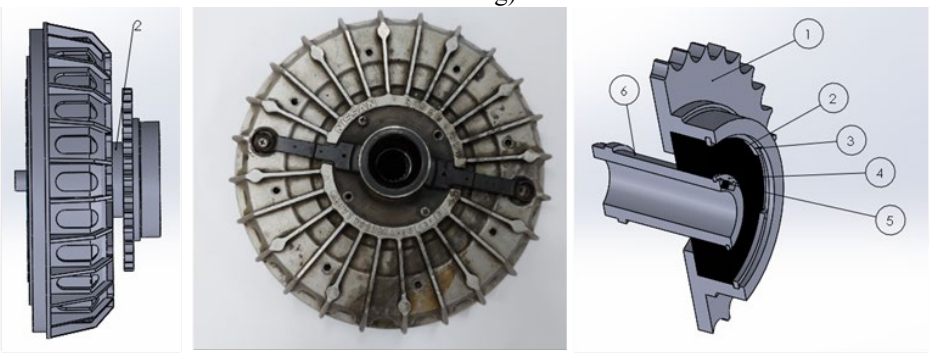

Figure 2. Electromagnetic powder clutch and one way bearing (1. Shaft, 2. One way bearing,3. Circlip 4. Circlip 5.Woodruff key)

3. RESULTS AND DISCUSSION

A chain-gear mechanism will be used for the electric motor to transmit power to the gearbox. In the design of this chain system, necessary calculations were made for the selection of the appropriate chain and a bearing with one-way clutch was selected for the electric motor to transmit one-way motion. The

electromagnetic clutch for the power transmission of the internal combustion engine has been revised considering the hybrid system requirements. The test system is shown in figure-3.

In this setup, a 15 kW Femsan brand direct current motor is used as the electrical power group, and the Honda Gx 270 type single-cylinder engine is internal combustion used as engine power group. In order to create a load at the gearbox output, a Kemsan brand 10 kW direct current motor was connected by revising the axle shaft.

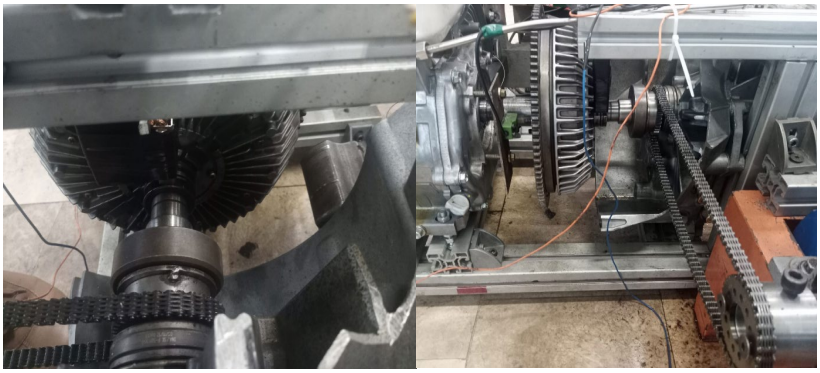

Figure 3. Experimental test system

In the experimental study, a 15 kW electric motor was started by a direct current motor driver and rotated. In the meantime, the field winding of the direct current motor at the gearbox output will be stimulated with a variable power supply between 0-200 V and the armature winding connected to the fixed resistors will produce voltage. With the current flowing through the resistors, the electric motor that rotates the gearbox will slow down. Cranking the internal combustion engine while this operating mode is in progress. Smooth power transmission conditions will be studied by connecting the clutch. The clutch voltage and current change are seen in table-1 . At 12,5 volt winding voltage, the magnetic clutch is fully engaged. When the voltage drops under 8.5 volts, the magnetic clutch is disengaged. In figure-4, the voltage drop point of the transmissions ouputshaft hall sensor is determined as torque starting point. In right picture, after 12,5 volt, the torque transmission of the electromagnetic clutch is uniform.

Table 1. Voltage-current change of elctromagnetic powder clutch

Volt	Amper
12.5	1.2
11.80	1.2
10.6	1
10	1
9.5	0.9
9	0.8
8.5	disengaged.

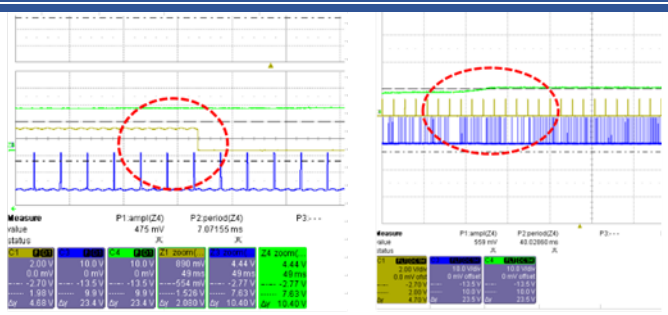

Figure 4. Torque transmission starting point of electromagnetic clutch

4. CONCLUSION

In order to carry out the preliminary experimental study, firstly, the circumferential and tensile forces on the chain were calculated. As a result of the calculations, it has been determined that it is appropriate to use a silent chain and two gears of the same diameter with 34 teeth. From the 15 kW electric motor to the bearingThe axial and radial forces acting on it were calculated. Based on these calculations, the electric motor CSKP35 series one-way bearing to provide one-way power transmission independently decided Formulas in which it is sufficient to use CSK12 series one-way bearings in the pre-experimental working system was determined using an electromagnetic clutch used in the automotive industry is used on the internal combustion engine side. Magnetic clutch, separation at the desired time with electronic signals and it is preferred to perform the binding function. After starting the motion transmission with the electric motor, the magnetic clutch will allow vibration-free transition in the transition to the internal combustion engine. In addition, in case of a possible problem, the clutch will be solved by cutting the voltage of the clutch. In order to control the partial clutch and full clutch states of this clutch, it will be necessary to apply a voltage in the range of 0-12 V. In this context, a variable voltage source will be used in the system. There is a linear relationship between the amount of applied voltage and the power transmitted over the electromagnetic clutch.

ACKNOWLEDGMENTS

This study was supported by TÜBİTAK under project number: ARDEB **216 M 253**.

REFERENCES

[1] G., Xiaolin Tang, Dejıı Zhang, Teng Liu, Amir Khajepour, Haisheng Yu (2019)" Research on the Energy Control of Dual-Motor Hybrid Vehicle During Engine Start-Stop Process

[2] Yoon Hyuk Shin, Sung Chul Kim, Min Soo Kim (2013) "Use of Electromagnetic Clutch Water Pumps

in Vehicle Engine Cooling Systems to Reduce Fuel Consumption"

[3] Mihael Cipek, Danijel Pavkovic ,Josko Petric (2013)"A Control-Oriented Simulation Model of A Power-split Hybrid Electric Vehicle,

[4] Kunqi Ma, Zahizhou Wang, Hai Liu, HangzhengnanYu, Changyin Wei (2019)" Numerical Investigation on Fuzzy Logic Control Energy Management Strategy of Parallel Hybrid Electrical Vehicle

[5] A. Haj-Fraj, F. Pfeiffer (2001) "Optimal Control of Gear Shift Operations in Automatic Transmissions" Ivar Roskifte Leikarnes (2017) "Modelling and Simulating a Hybrid Electric Vehicle"

[6] M. Jianning Zhao (2017)"Design and Control Co-Optimization for Advanced Vehicle Propulsion Systems

[7] K.David Huang, Sheng-Chung Tzeng (2004) "A New Parallel Type Hybrid-Electric Vehicle

[8] Naila Mikhaeil-Boules (1994)"Design Analysis of Electromagnetic Particle Clutch"

[9] A.Ergenc, A.Ergenc (2015)"A New Control Scheme for Automated Manual Transmission with Electromagnetic Powder Clutch"

2nd International Natural Science, Engineering and Material Technologies Conference
Sep 15-17, 2022, İğneada-Kırklareli / TÜRKİYE

PREPERATION AND CHARACTERIZATION OF NOVEL MODIFIED GRAPHENE OXIDE REINFORCED NANOCOMPOSITE MATERIALS BY SLA 3D PRINTER

E. Akın[1], M. Çakır[1], B. Berberoğlu

[1]*Department of Metallurgical and Materials Engineering, Faculty of Technology, Marmara University, İstanbul, TÜRKİYE*

E-mail: emre.akin@marmara.edu.tr

Abstract

As well known, epoxy acrylate resins have been widely used in SLA 3D printers applications. Epoxy acrylate systems have generally consisted of bisphenol-A glycerolate diacrylate (epoxy acrylate resin) and 1,6-Hexanediol diacrylate (HDDA, reactive diluent resin). The purpose of this study is to develop novel epoxy acrylate systems for 3D SLA printers and observe the properties of produced materials. For this reason, novel modified graphene oxide phases were synthesized. First, graphene oxide was synthesized by Hummers method. Then aromatic diisocyanates (TDI;toluendiisocyanate and IPDI; isophorone diisocyanate) and 2-Hydroxyethyl methacrylate (HEMA) were reacted with graphene oxides in THF solvent. These modified graphene oxide solutions were entegrated into epoxy acrylate system. Tensile, izod impact resistance, shore-D hardness, abrasive and density tests were applied to the produced materials. Considering of the results, substantial increases were observed in terms of tensile strength and modulus, izod impact resistance, taber abrasive resistance and shore-D hardness. Moreover, densities of the produced novel samples presented considerable increases.

Keywords: SLA type 3D Printer, epoxy acrylate, modified graphen oxide, reinforced nanocomposite

1. INTRODUCTION

Currently, ultraviolet (UV)-curable products have received great interest due to both technological advances and the increasing environmental pressure to decrease the emission of volatile organic compounds (VOC) [1]. In comparison with conventional solvent-based products, UV-curable products present the advantage of low VOC emission, rapid curing at ambient temperature, low energy consumption, high productivity and high degrees of cross-linking (cause to outstanding scratch, chemical resistance). Therefore, these products provide a wide range of economic and ecological benefits. UV-curable coatings usually contain four main components the oligomer, the reactive diluent, the photoinitiator and various additives [2].

Epoxy acrylate (EA) is a common oligomer in UV-curable coatings, which is the most principal component for film formation [3]. There have been two kinds of epoxy acrylate oligomers that have been widely used. These are bisphenol diglycidyl ether and epoxy novolac based epoxy acrylate oligomers. As reactive diluents, hexanediol diacrylate (HDDA) and tripropylene glycol diacrylate (TPGDA) have been generally used in epoxy acrylate systems. These reactive diluents adjust the viscosity and crosslinking density of epoxy acrylate systems [4]. However, epoxy acrylate products cannot been used as high performance material due to their lower mechanical and thermal properties. They have been widely used in decorative coatings, jewellery and filler materials. For these reasons, there have been various studies on improving epoxy acrylate systems in literature. Pan et al. [5] cellulose nano cyrstals reinforced epoxy acrylate system and investigate mechanical and thermal properties. Wang et al. [6] obtained high performance UV curable epoxy acrylate nanocomposite coatings reinforced with aramid fibers. When compared to neat EA, the tensile strength of the 0.05 wt% ANF-reinforced nanocomposites increased by 36%, and the elongation at break of the 0.1 wt% ANF-reinforced nanocomposites increased by 194%. Desai and Jagdap [7] improved epoxy acrylate systems reinforced with three types of synthetic fibers such as glass fibers, nylon fibers, and polyester fibers. They improved the neat epoxy acrylate system substantially. On the other hand, another reinforcing system is graphe oxide. Graphene oxide has been mostly used in polymers as reinforcing material. Sreenivasulu et al. [8] prepared review about graphene reinforced polymer composites. They mentioned that graphene reinforced polymer composites present high performance properties by using proper method. Uysal et al. [9] prepared modified graphe oxide reinforced epoxy acrylate systems with 3-(methacryloyloxy) propyl trimethoxysilane

(MEMO) and obtained improved mechanical properties. Cakir et al. [10] prepared graphene oxide reinforced polyimide foams and they presented high thermal properties.

In the light of these informations, this study presents modified graphene oxide reinforced epoxy acrylate systems. Graphene oxide (GO) was modified by two kinds of aromatic functional monomers obtained from the reactions of two kinds of diisocyanates (Toluene diisocyanate (TDI) and isophorone diisocyanate (IPDI)) and 2-Hydroxyethyl methacrylate (HEMA). These functional monomers were synthesized in our laboratory. These modified GO was incorporated into epoxy acrylate system in various ratios and the properties of produced epoxy acrylate systems were investigated. Tensile, izod impact, shore-D hardness, taber abrasive and density tests were applied to the produced samples. Substantial increases were observed in terms of tensile strength and modulus, izod impact resistance, taber abrasive resistance and shore-D hardness.

2. MATERIAL AND METHODS

2.1. Materials

Bisphenol A glicerolate diacrylate (Bisphenol A based epoxy acrylate oligomer) and hexanediol diacrylate (HDDA) was purchased from Sigma-Aldrich. Irgacure 819 was used as photoinitiator. IPDI and TDI were used as aromatic monomeric diisocyanate that purchased from Covestro, 2-Hydroxymethyl methacrylate (HEMA) was used to react with IPDI and TDI. The product that obtained from the reaction of TDI and IPDI with HEMA was used to modified GO. GO was synthesized by Hummers method. Dibutyltin dilaurate (T12) was used as catalyst for the synthesis of the functional monomer obtained from the isocyanates and HEMA. Tetrahidrofuran (THF) was used as solvent in this reaction.

2.2. Synthesis of graphene oxide

Graphene oxide nanoparticles were obtained by the improved Hummers method. For this method, a 9:1 mixture of concentrated H_2SO_4/H_3PO_4 was incorporated into a mixture of graphite flakes and and $KMnO_4$, producing a slight exothermal reaction to 35–40 °C. The reaction was then heated to 50 °C and stirred for 12 h. Then, a little distilled water was slowly added. Heat was released as the reaction was exothermic. The solution was stirred for 2 h. Then the rest water was added and stirred for 1 h. After that 30% H_2O_2 was added and stirred for 2h in order to precipitate GO and finish reactions. When the solution reached ambient temperature, the GO solution was obtained before the purification. During the purification step of the GO solution, the GO solution

was firstly centrifuged at 6000 rpm. The subsided GO was filtered and washed with 30% HCl three times. After washing with HCl, the GO solution was washed with ethanol three times. After each washing process, GO solution was centrifuged at 6000 rpm and filtered. After the washing with HCl and ethanol, the solvent of the filtered GO solution was exchanged with THF by washing with THF and centrifuging. Therefore, the GO was prepared in THF solvent.

2.2. Synthesis of the functional monomer to modify graphene oxide

HEMA was added in a flask and THF solvent was poured into the flask. The solution was magnetically stirred. After that IPDI or TDI was added drop by drop into the flask. Then, the tin catalyst (T12) was added and stirred magnetically at 60 ºC in a nitrogen atmosphere for two hours. The reaction was applied in equal molar. The mole ratio of disocyanates and HEMA was 1/1. The functional monomer was terminated both urethane acrylate and isocyanate. The weight ratio of THF/solid in solution was ½. This functional monomer solution was used to modify GO particulates. The flowchart of the functional monomer synthesis was given in Figure 1.

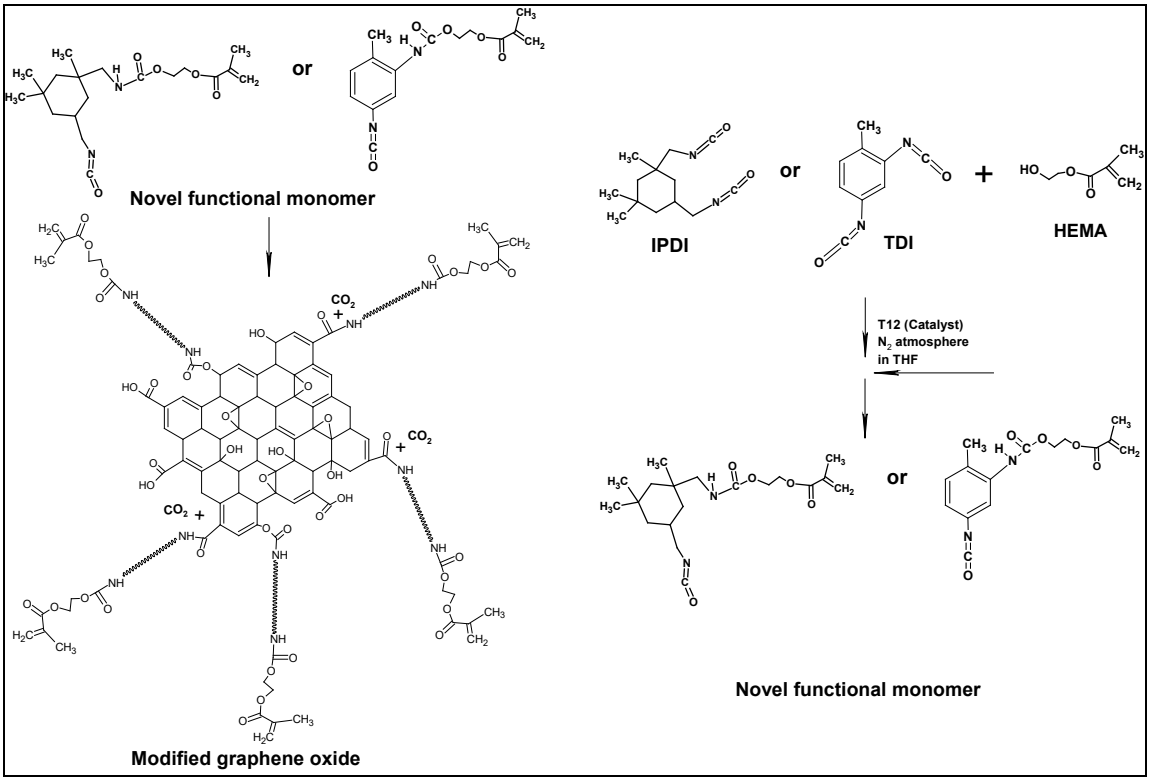

Figure 1. The synthesis scheme of functional monomer and mGO

2.3. Preparation of modified graphene oxide solution and modified graphene oxide reinforced epoxy acrylate nanocomposites

The purified GO solution in THF was incorporated into the functional monomer solution as 10% in total solution by weight. After incorporating process, the new solution was stirred for 5 h to obtain homogeneous solution and complete reactions. This mGO solution was centrifuged to remove excess functional monomer solution and purifiy mGO. The purified subsided GO solution in centrifuged tubes was incorporated into pure epoxy acrylate system in the range between 0% and %1 by weight in order to prepare epoxy acrylate nanocomposites according to solid content of the purified mGO solution. The subsided or purified GO was like mud. The solid content of the purified mGO solution in THF was determined as 5.43% after drying in a vacuum oven at 80 ℃ for 3 days. The synthesis scheme of mGO was also given in Figure 1. Pure epoxy acrylate resin was prepared consisting of %50 of bisphenol A glicerolate diacrylate resin and %50 of HDDA resin. This ratio of pure epoxy acrylate was used to obtain mGO reinforced epoxy acrylate nanocomposites. After the preparation of all sample solutions, each solution was added into the resin tank of SLA type 3D printer and exposed to UV to be cured. In conclusion, the final nanocomposite products were prepared.

2.4. Measurements

Measurements were carried out for film and coating samples. Coating samples were used to characterize abrasion resistance. Film samples were used for the other tests. Fourier transform infrared spectroscopies (FT-IR) were conducted by Shimadzu 8303 FT-IR Spectrometer. The samples were characterized mechanically by standard tensile test in order to determine in terms of tensile strength, failure strain and young modulus according to ASTM D638. Tensile test was carried out by using a crosshead speed of 5 mm/min. Izod impact resistance was measured using unnotched samples according to ASTM D 4812-99 (ASTM D 256) using Zwick B5113.30 with hammer of 5.4J at a striking rate of 3.96 m/s. For each sample three measurements were taken and the average value was used for the calculations. Hardness of the samples were measured according to Shore D method. Coating samples were also produced besides film samples for abrasion test. Taber abrasion test were applied to the produced coating samples. Density was measured according to archimed principle for film samples.

3. RESULTS AND DISCUSSION

The FT-IR spectras of novel functional monomers (TDI+HEMA or IPDI+HEMA) consisting of urethane acrylate and NCO bondings are given in Figures 2 and Figure 3. This monomer was synthesized to modify GO particulates. The absorption bands were given at around 3200-3500, 1720 and 810 cm^{-1} relate to –NH stretching, C=O stretching and C=C twisting of acrylate, respectively.

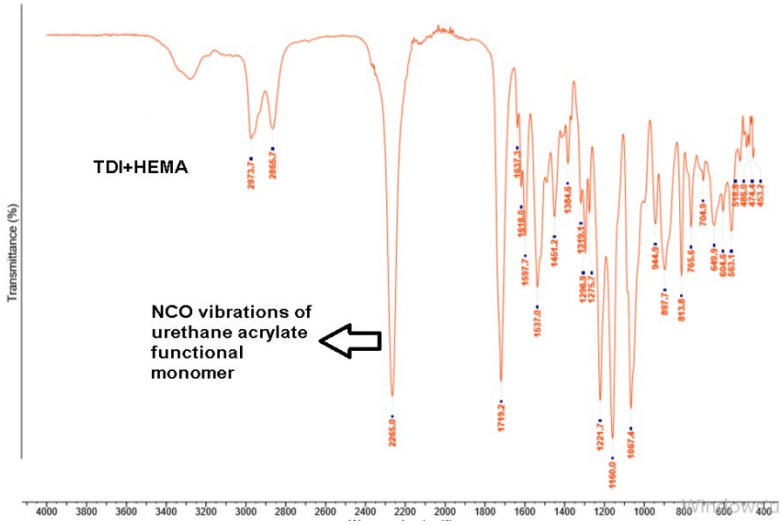

Figure 2. FT-IR results of novel functional monomer obtained from the reaction of TDI and HEMA

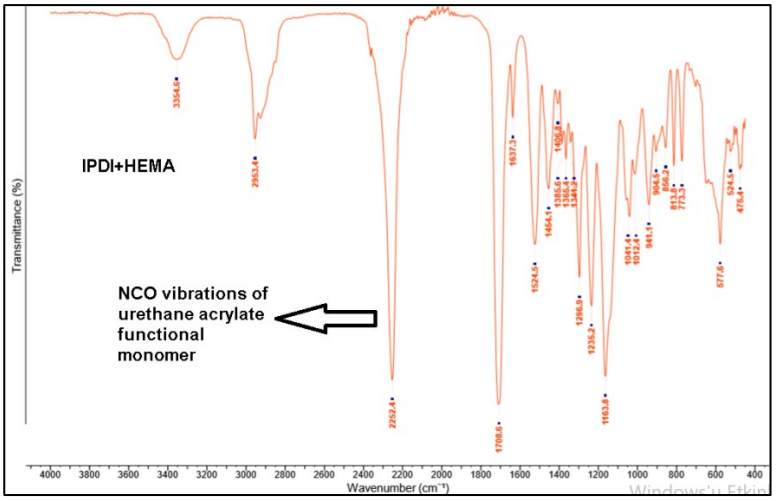

Figure 3. FT-IR results of novel functional monomer obtained from the reaction of IPDI and HEMA

From the IR spectra in Figure 4 and 5, the disappearance of the characteristic absorption band at 2250-2270 cm^{-1} related to isocyanate group (-NCO) indicates the completion of the reaction. In addition to this, the

absorption bands at around 2850 and 2900 belonging to CH and CH_2 bonding in Figure 2 and 3 became larger and longer. These results show that the functional groups of GO particulates (OH or COOH groups) reacted with NCO functional groups on the novel functional monomers (TDI+HEMA or IPDI+HEMA). As a result of these reactions, amide and urethane functional groups were occurred.

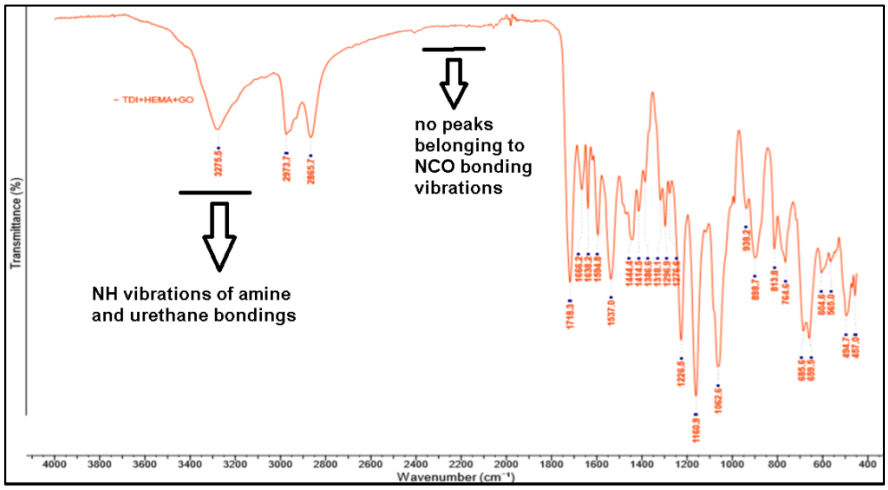

Figure 4. FT-IR results of GO containing novel functional monomer obtained from the reaction of TDI and HEMA

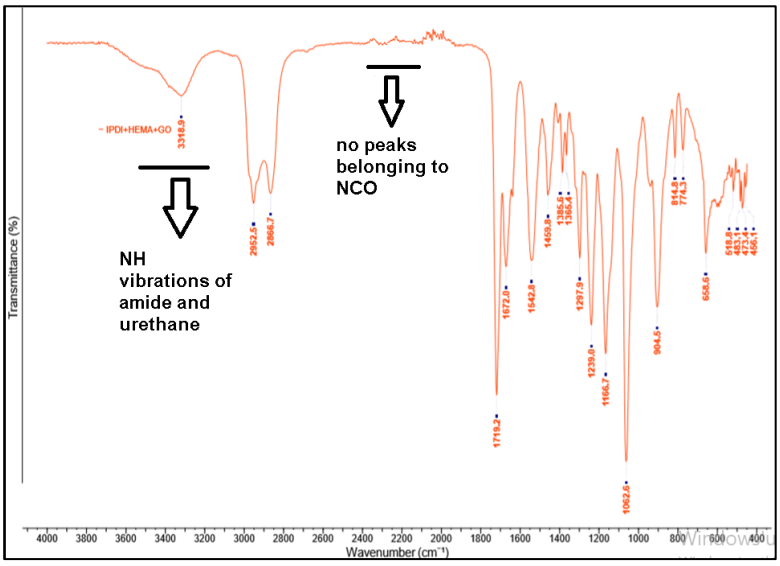

Figure 5. FT-IR results of GO containing novel functional monomer obtained from the reaction of IPDI and HEMA

Pure epoxy acrylate system was prepared by using bisphenol A glicerolate diacrylate and 1,6-Hexanediol diacrylate (HDDA) reactive diluent resin. These components were used as 1/1 by weight. They were

mechanically stirred in flask and homogeneous resin was obtained. The structures of these components were shown in Figure 6 and Figure 7. Modified GO (mGO) was chemically bonded this pure epoxy acrylate system by curing UV.

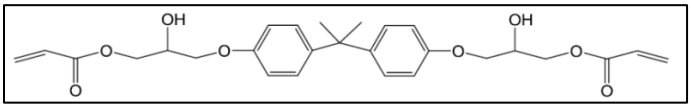

Figure 6. Bisphenol A diglycidyl ether based epoxy acrylate

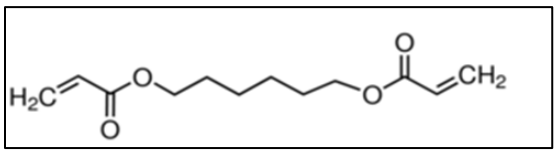

Figure 7. 1,6 Hexanediol diacrylate

GO was modified by the novel functional monomer with TDI or IPDI. Therefore urethane acrylate groups covalently bonded GO solution was obtained. This solution was added into the pure epoxy acrylate in the ratios of %0.25, %0.5, %0.75, %1, %1.25 and %1.5.

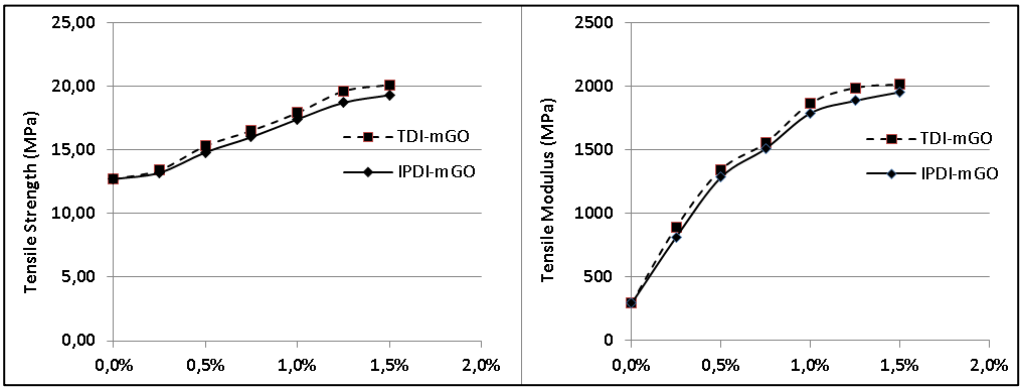

Figure 8. Tensile strength and modulus values of the produced samples

Mechanical tests were performed to determine the properties of mGO reinforced epoxy acrylate samples. As mentioned, modifying of GO was applied by two kind of functional monomer obtained from the reaction of HEMA and TDI or IPDI. Therefore two kinds of mGO reinforced epoxy acrylate samples were obtained and the properties of them were compared each other and pure epoxy acrylate sample.

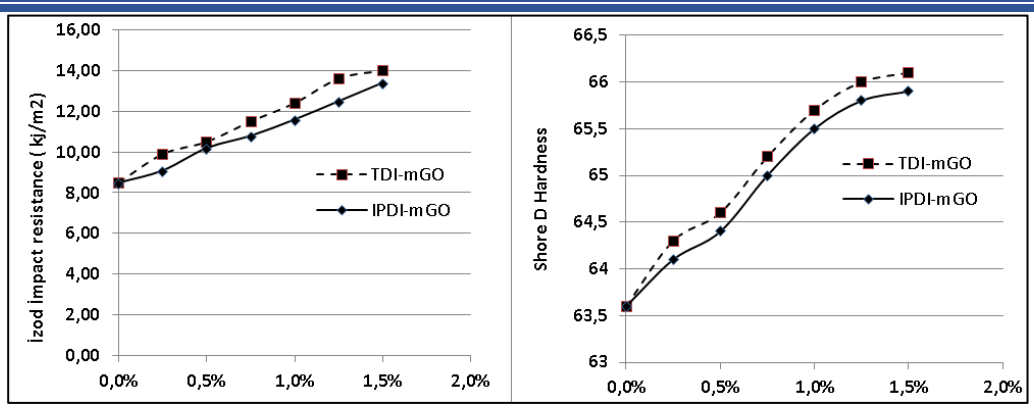

Figure 9. Izod impact resistance and hardness values of the produced samples

The ultimate tensile strength of the mGO reinforced samples with TDI+HEMA (mGO-TDI) showed an increase of %58 while the mGO reinforced samples with IPDI+HEMA (mGO-IPDI) showed an increase of %52. Moreover tensile modulus values of mGO-TDI and mGO-IPDI samples showed huges increases of % 587 and %567, respectively. Besides the increasing in strength values, the samples became much more rigid. The increase trends of tensile strength and modulus were given in Figure 8. In addition of these positive results, izod impact resistance of the reinforced sample showed considerable increases as shown in Figure 9. The impact resistance values of mGO-TDI and mGO-IPDI samples increased up to 39% and 35%, respectively. The impact resistance values showed continuous increase with the increase of reinforcing ratios. This situation could be derived from covalent bonding of mGO particulates between the epoxy acrylate chains and dispersed homogeneously in the matrix. The acrylated chains on the mGO particulates were covalently bonded by UV. Therefore hard nano particulates were bonded strongly like HDDA in the matrix. Shore D hardness values confirmed this situation. The hardness values also showed continuous increase with the increase of reinforcing ratios. The hardness values of mGO-TDI and mGO-IPDI samples increased up to 3.9% and 3.6%, respectively. Shore D hardness values are also given in Figure 9.

Table 1. The properties of TDI-mGO modified samples and pure sample

TDI-mGO	Tensile strength (MPa)	Tensile modulus (MPa)	Izod impact resistance (kj/m^2)	Shore D hardness	Taber abrasive resistance (weight loss, gr)	Density (gr/cm^3)
0%	12.7	293	8.5	63.6	0.0011	1.19
0.25%	13.4	894	9.9	64.3	0.0011	1.20
0.50%	15.3	1345	10.5	64.6	0.00095	1.21
0.75%	16.5	1555	11.5	65.2	0.0009	1.23
1%	17.9	1866	12.4	65.7	0.0008	1.24
1.25%	19.6	1987	13.6	66	0.0007	1.25
1.50%	20.1	2015	14	66.1	0.0006	1.26

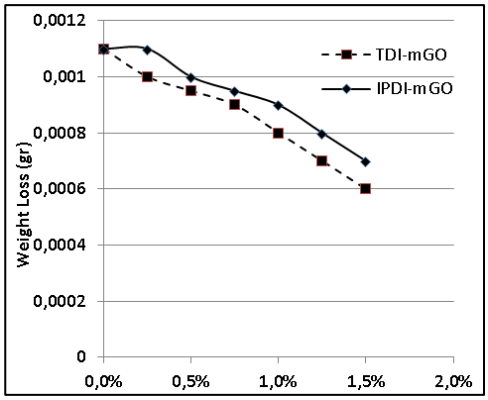

Figure 10. Taber abrasive resistance values of the produced samples

Table 2. The properties of IPDI-mGO modified samples and pure sample

IPDI-mGO	Tensile strength (MPa)	Tensile modulus (MPa)	Izod impact resistance (kj/m^2)	Shore D hardness	Taber abrasive resistance (weight loss, gr)	Density (gr/cm^3)
0%	12.7	293	8.5	63.6	0.0011	1.19
0.25%	13.2	815	9.1	64.1	0.0011	1.20
0.50%	14.8	1284	10.2	64.4	0.0010	1.21
0.75%	16	1510	10.8	65	0.00095	1.23
1%	17.4	1788	11.6	65.5	0.0009	1.24
1.25%	18.7	1885	12.5	65.8	0.0008	1.25
1.50%	19.3	1953	13.4	65.9	0.0007	1.26

Taber abrasive resistance of mGO reinforced samples increased substantially. After 1000 cycles, the difference of weight loss decreased significantly as the reinforcing ratio increased. The samples of 1.5% showed the most improved values. It was thought that it could be derived from the hard structure of GO particulates. Taber abrasive resistance increasing trend of all samples was given in Figure 10. In addition to these results, densities of the samples were measured by Archimed principle. The all reinforcing samples showed a little continuous increase. All results were given in Table 1 and Table 2.

4. CONCLUSION

In this study, novel mGO reinforced epoxy acrylate systems were developed by synthesizing modified GO particulates. IPDI or TDI and HEMA monomers were used to synthesize a novel NCO containing urethane acrylate functional monomer. This functional monomer was chemically bonded on GO particulates by means of the functional groups on GO such as COOH or OH. Therefore acrylated modified GO particulates were obtained and these particulates were incorporated into conventional epoxy acrylated system in the range between 0%-1.5% by weight. Tensile, izod impact, shore-D hardness, taber abrasive and density tests were applied to these produced samples. Considering of the results, mGO reinforced epoxy acrylate systems exhibited much more improved results compared to conventional epoxy acrylate system. It exhibited substantial increases in terms of tensile strength, modulus, izod impact resistance, hardness and taber abrasive resistance. This mGO reinforced epoxy acrylate systems can be used in applications that required higher mechanical and abrasive properties for epoxy acrylate systems of SLA type 3D printers.

REFERENCES

[1] Aerykssen, J.H., Khudyakov, I.V., New acrylated oligomers with a sulfide group for radiation-curable coatings. Industrial Engineering Chemistry Research, 9, 50:1523, 2011.

[2] Chemtob, A., Versace, D.L., Belon, C., Céline, C.B., Rigolet, S. Concomitant organic-inorganic UV-curing catalyzed by photoacids. Macromolecules, 41:7390, 8, 2008.

[3] Çakir, M., Akin, E., Ulak, P. Properties of UV-Curable bisphenol-A glycerolate diacrylate coatings containing 1H,1H,2H,2H-perfluorodecyl acrylate monomer. El-Cezerî Journal of Science and Engineering, 5, 3, 836-844, 2018.

[4] Yıldiz, Z., Usta, İ., Synthesis and characterization of dual-curable epoxyacrylates for polyester cord/rubber applications. Journal of Industrial Textiles, 46(2), 2018.

[5] Pan, H., Song, L., Ma, L., Hu, Y., Transparent Epoxy Acrylate Resin Nanocomposites Reinforced with Cellulose Nanocrystals Industrial and Engineering Chemistry Research, 51 (50), 16326-16332, **2012**.

[6] Wang, Y., Qu, R., Pan, Y., Luo, Y., Zhang, Y., Sun, C., Ji, C., High-performance UV-curable epoxy acrylate nanocomposite coatings reinforced with aramid nanofibers, Progress in Organic Coatings, Volume 163, 106631, 2022.

[7] Desai, P.D., Jagtap, R.N., Synthesis and characterization of fiber-reinforced resorcinol epoxy acrylate applied to stereolithography 3D printing., ACS Omega, 11;6(46), 31122-31131,2021.

[8] Sreenivasulua, B., Ramji, B.R., Nagaral, M., A review on graphene reinforced polymer matrix composites, Materials Today: Proceedings, 5, 2419–2428, 2022.

[9] Uysal, E., Çakir, M., Ekici, B., Graphene oxide/epoxy acrylate nanocomposite production via SLA and importance of graphene oxide surface modification for mechanical properties, Rapid Prototyping Journal, 27(4),682-691, 2021.

[10] Çakir, M., Kılıç, V., Boztoprak, Y., Karaer Özmen, F., Graphene oxide-containing isocyanate-based polyimidefoams: Enhanced thermal stability and flame retardance, Journal of Applied Polymer Science, 138, e51012, 2021.

2nd International Natural Science, Engineering and Material Technologies Conference
Sep 15-17, 2022, İğneada-Kırklareli / TÜRKİYE

CHEMICAL, MORPHOLOGICAL, AND STRUCTURAL CHARACTERISTICS OF PEGylated MAT-CuO NANOPARTICLES

G. Karabulut[1], N. Beköz Üllen[1], S. Karakuş[2]

[1]*Department of Metallurgy and Materials Engineering, Faculty of Engineering, İstanbul University-Cerrahpasa, İstanbul, TÜRKİYE*
[2]*Department of Chemistry, Faculty of Engineering, İstanbul University-Cerrahpasa, İstanbul, TÜRKİYE*

E-mail: gizem.karabulut@iuc.edu.tr

Abstract

In recent years, green copper oxide nanoparticles (CuO NPs) have been widely used in various applications such as pharmaceuticals, electronics, environmental applications, catalysts, gas sensors, superconductors, solar cells, and biomedical applications. The green synthesis of the metal-based nanoparticles, which are desired to be used in biomedical applications, from bio-based sources is more advantageous. In this study, PEGylated matcha extract-copper oxide nanoparticles (PEGylated Mat-CuO NPs) were synthesized using a sonochemical technique via a green chemistry approach. The green PEGylated Mat-CuO NPs were characterized by scanning electron microscopy, transmission electron microscopy, ultraviolet visible spectroscopy, X-ray diffraction, X-ray photospectrometry, and Fourier transmission infrared spectroscopy. According to the experimental results, *PEGylated* Mat-CuO NPs were successfully synthesized, and they had a spherical shape with a particle size ranging from 20 to 40 nm. Consequently, the prepared *PEGylated* Mat-CuO NPs are a promising nanocomposite using a low-cost and green way to obtain advanced nanomaterials as nanocarriers, nanoagents, and nanocoating materials in biomedical applications.

Keywords: Copper oxide nanoparticles, green chemistry, sonochemical synthesis, nanobiocomposite

1. INTRODUCTION

Metal-based nanoengineered materials attract attention because they cover a wide range of areas of advanced research. Metal and metal oxide nanoparticles (NPs) have been used in many applications such as agricultural, medical, electrical, optical, etc. Metal oxide NPs are becoming increasingly popular in nanotechnology applications due to their many properties, such as high surface-area-to-volume ratio, good catalytic, high stability, surface functionalizability, compatibility, and tunability [1,2]. Among the metal oxide NPs, copper oxide NPs (CuO NPs) are a p-type semiconductor material with a monoclinic structure and a band gap of between 1.2 eV and 3.57 eV, exhibiting magnetic, optical, and electrical properties [3]. It has a wide range of usage, such as pharmaceutical, electronic, environmental applications, catalysts, gas sensors, superconductors, solar cells, and biomedical applications (antimicrobial, anti-pollution, drug delivery, etc.) [3–6]. From the past to the present, many physical, chemical, and biological methods have been used for the synthesis of CuO NPs [7]. Today, green processes come to the fore in many areas due to the occurrence of many problems related to climate change, water pollution, limited natural resources, human health, and other global problems. Nowadays, green synthesis has a tremendous impact on the production of biocompatible CuO NPs [8].

In this study, based on the objectives of green production processes, CuO NPs were synthesized by the sonochemical method in a biopolymer matrix with a green chemistry approach. Plant extract-based synthesis for CuO NPs provides many advantages such as cost-effectiveness, biocompatibility, no harmful substances, environmental friendliness, simplicity, and reliability [7]. For this purpose, green synthesis of CuO has been carried out successfully with matcha powder extract. In addition to the matcha extract, polyethylene glycol was used for the matrix. Matcha is a green tea in powdered form. The high levels of phenolic compounds in its content cause it to show antioxidant properties [9,10]. Polyethylene glycol (PEG) is a non-toxic, non-volatile, and naturally degradable green solvent [11]. A sonochemical method was used for the synthesis of the PEGylated Mat-CuO NPs. This method enables the synthesis of NPs at high pressures and high temperatures through acoustic cavitation by making use of ultrasonic sound waves [12]. The synthesized PEGylated Mat-CuO NPs were characterized by several techniques such as scanning electron microscopy (SEM), transmission electron microscopy (TEM), ultraviolet visible spectroscopy (UV-Vis), X-ray diffraction (XRD), X-ray photospectrometry (XPS), and Fourier transmission infrared spectroscopy (FT-IR).

2. MATERIAL AND METHODS

2.1. Materials

Copper (II) sulfate pentahydrate ($CuSO_4.5H_2O$) and sodium hydroxide (NaOH, 40.00 g/mol) were purchased from Merck Company (Germany). Matcha tea powder was obtained from Arifoğlu Company (Turkey). The filter paper (Whatman® qualitative paper, diameter: 25 mm) was purchased from Sigma Aldrich Company (Germany). All chemicals and reagents were used without further purification.

2.2. Synthesis of *PEGylated* Mat-CuO NPs

Firstly, the preparation of plant extract was carried out to be used in nanoparticle synthesis. Matcha tea powders were washed several times with distilled water and then dried in an oven at 50 °C for 2 hours. Prepared matcha powder was taken to weigh 5 g and added to 100 mL of distilled water. Then, it was kept in a closed sterile container in a dark environment at 27 °C in a fixed position for 3 days. Finally, the sample was decanted and filtered with coarse filter paper so that matcha extract (Mat) was obtained.

For the synthesis of PEGylated Mat-CuO NPs, 0.1 g of PEG was added to 20 mL of prepared matcha extract and mixed at 500 rpm for 10 minutes. 0.0424 g of $CuSO_4.5H_2O$ was dissolved in 50 mL of distilled water and stirred for 10 minutes at 27 °C. 0.2 g of NaOH was dissolved in 50 mL of distilled water and stirred for 10 minutes at 27 °C. Then, 3 mL of NaOH solution and 50 mL of $CuSO_4.5H_2O$ solution were added dropwise into the Mat/PEG solution with the help of a Pasteur pipette and mixed at 27 °C for 10 minutes at 500 rpm. Finally, sonication was applied for 30 minutes at 50% amplitude, and the solution was filtered with a 0.22 µm sterile filter at the end of the process. It was stored in a sterile container at room temperature (27 °C) in a dark medium.

2.3. Characterization of *PEGylated* Mat-CuO NPs

The prepared PEGylated Mat-CuO NPs were characterized to obtain morphological, chemical, and topological properties of the nanostructure. The Zeiss-Sigma 300 SEM device was used to investigate the surface morphology and topography of synthesized PEGylated Mat-CuO NPs. The Hitachi High Tech HT7700-TEM device in a high vacuum mode at 100 kV was used to investigate the particle size and morphology of the synthesized PEGylated Mat-CuO NPs. The PG Instrument a double-beam UV–Vis

spectrophotometer device (T + 80 model) was used to perform absorbance measurements of the PEGylated Mat-CuO NPs. The Perkin Elmer FT-IR device (Spectrum Two model) was used to perform functional groups of the PEGylated Mat-CuO NPs in the frequency range of 4000–400 cm^{-1} with a resolution of 4 cm^{-1} and 8 scans. The Rigaku D/Max2200/PC XRD device was performed to determine the crystalline structure of the PEGylated Mat-CuO NPs with Cu-Kα radiation from 20° to 80 at 40 kV and 15 mA. Specs-Flex XPS device analysis was used to determine the elemental composition and chemical properties of the PEGylated Mat-CuO NPs with Al-Kα radiation.

3. RESULTS AND DISCUSSION

The surface morphology and topography of synthesized PEGylated Mat-CuO NPs were characterized by SEM and TEM techniques. SEM (a), TEM (b) images of the PEGylated Mat-CuO NPs, and histogram of the particle size distribution TEM image of the PEGylated Mat-CuO NPs were given in Figure 1. In the SEM results, the structure of the PEGylated Mat-CuO NPs is agglomerated and the particles are at the nanoscale (less than 100 nm). In the TEM results, it was observed that the PEGylated Mat-CuO NPs are homogeneously dispersed and spherical in shape. The size of nanoparticles ranges from 10 to 50 nm, and the average particles size is 21.82 nm. The morphological and topographic properties of PEGylated Mat-CuO NPs are compatible with plant-based synthesized CuO NPs in the literature [13].

The PEGylated Mat-CuO NPs were then subjected to UV-Vis analysis to obtain the absorbance measurement. The spectrum of the synthesized PEGylated Mat-CuO NPs was given in Figure 2. The color change from green to brown indicates the formation of the CuO NPs [14]. The peak was formed at 321 nm in the spectra, which is consistent with the literature [15].

FTIR spectrum of the PEGylated Mat-CuO NPs is given in Figure 3. The characteristics peaks of the NPs were formed at 3329.50 cm^{-1} (-OH), 2980.45 cm^{-1} (asymmetric -CH_2 vibration), 1617.12 cm^{-1} (C=O), 1385.61 cm^{-1} (C-N stretching), 1093,44 cm^{-1}(C-O stretching). In addition to the these peaks, Cu-O stretching vibration peaks formed at 943.02 cm^{-1}, 834.06 cm^{-1}, 763.67 cm^{-1}, 659.54 cm^{-1}, and 592.04 cm^{-1} [13].

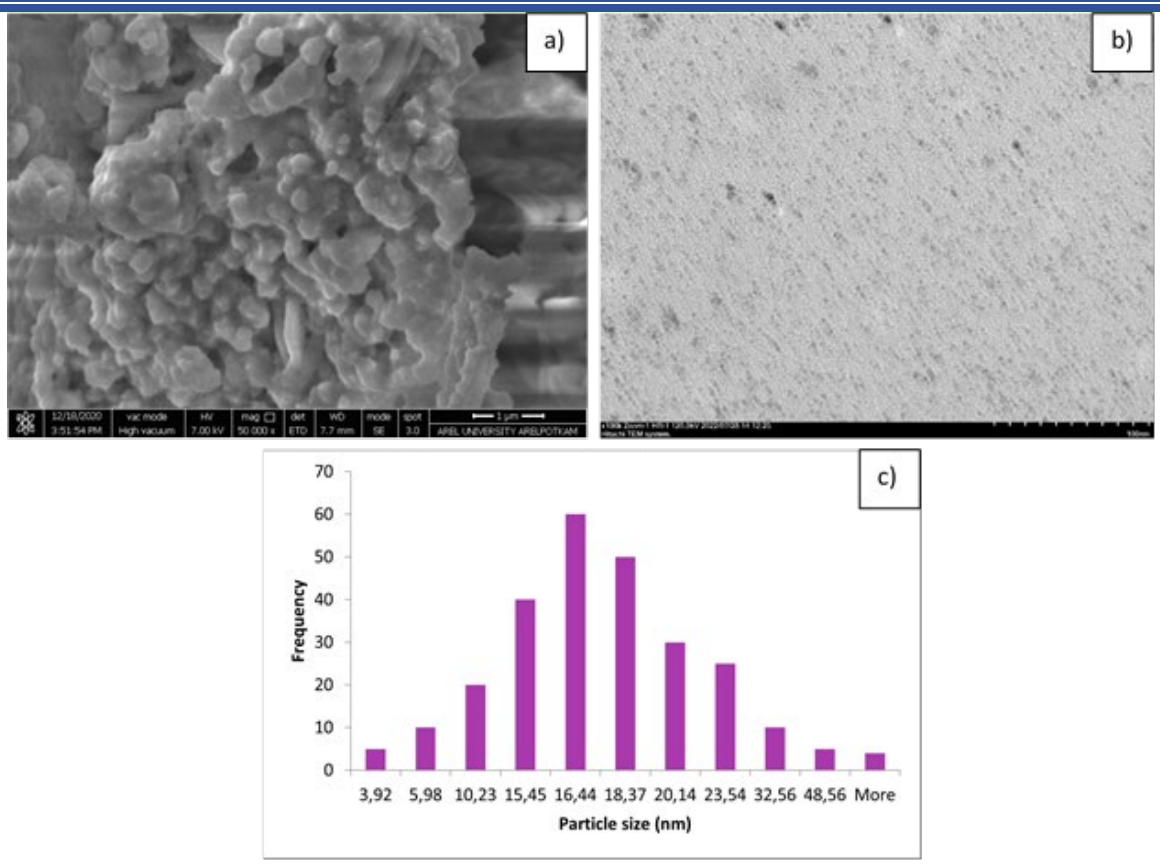

Figure 1. (a) SEM, (b) TEM images of the PEGylated Mat-CuO NPs, and (c) histogram of the particle size distribution.

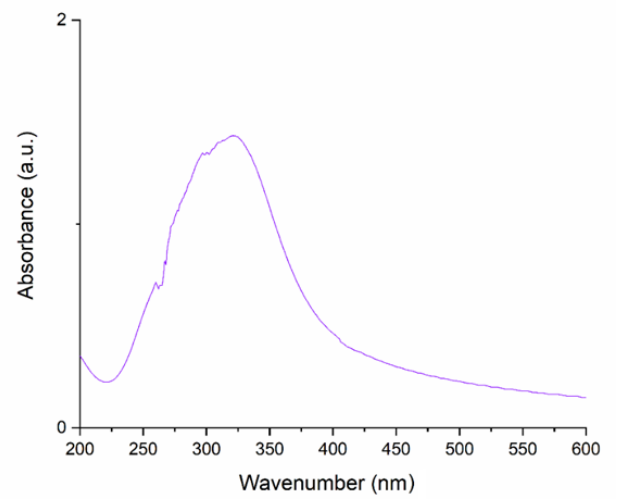

Figure 2. UV-Vis graph of the PEGylated Mat-CuO NPs

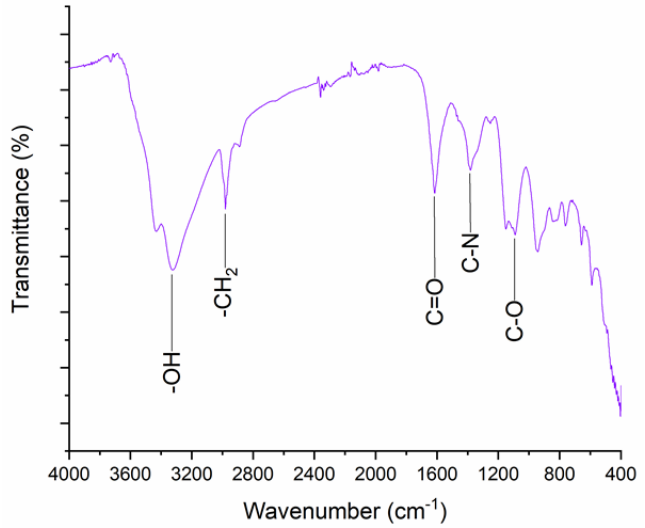

Figure 3. FT-IR spectra images of the PEGylated Mat-CuO NPs

The XRD pattern graph the prepared PEGylated Mat-CuO NPs solution is given in Figure 4. The characteristic peaks of the CuO NPs are formed at 2θ = 31.5°, 39.5°, 45.4°, 47.3°, 56.3°, and 75.1°. These peaks correspond to the reflections of the planes as (110), (111), (-112), (-202), (021), and (222), respectively. These planes were identified that the monoclinic structure of the CuO NPs. The other undefined peaks (2θ = 28.3° and 29.4°) are due to the phenolic structures of the plant structures in the nanostructure. The patterns of the PEGylated Mat-CuO NPs corresponded to the JCPDS Card No. 04-015-5865.

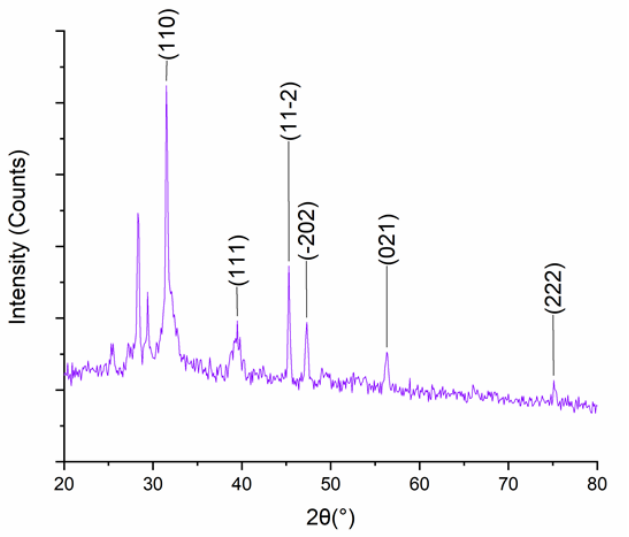

Figure 4. XRD pattern of the PEGylated Mat-CuO NPs

The prepared PEGylated Mat-CuO NPs' surface compounds, state of valance electrons, and binding energies were obtained with XPS. Figure 5 shows the spectra of PEGylated Mat-CuO NPs (a) survey spectrum, (b) Cu_{2p}, (c) O_{1s}, and (d) C_{1s}. The Cu_{2p} spectrum of the prepared PEGylated Mat-CuO NPs was determined with two peaks at about 934 eV and 953.7 eV. These peaks correspond to the 2p3/2 and 2p1/2 orbits of copper metal, respectively. The peaks are formed at 943.2 eV and 962.9 eV corresponding to the satellite peaks [16]. The O_{1s} peaks were formed at 530.2 eV, these peaks indicate the oxygen attached to the copper and the formation of CuO. The C_{1s} peaks were formed at 283.6 eV, these peaks derived from the Matcha extract of phytochemicals. The XPS results confirmed the PEGylated Mat-CuO NPs form a successful bond between Cu and O [17]. The results are consistent with previous studies [16–19].

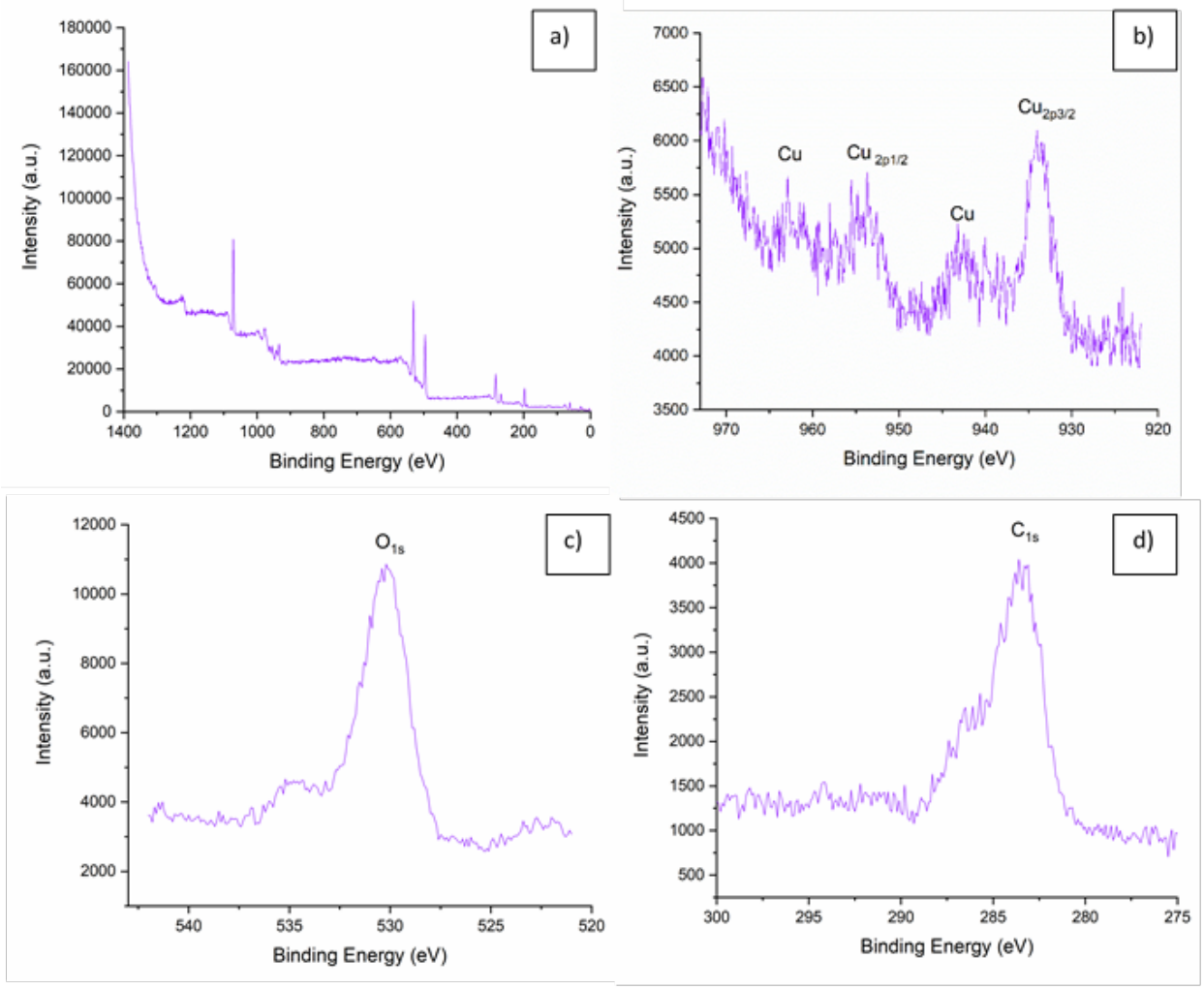

Figure 5. XPS graphs of the PEGylated Mat-CuO NPs a) survey spectrum, b) Cu2p, c) O1s, and d) C1s

4. CONCLUSION

In this study, PEGylated Mat-CuO NPs were prepared a sonochemical approach, which is a green, facile, and cost-effective synthesis technique. The synthesized NPs were characterized to obtain morphological, topographical, and physicochemical properties. The PEGylated Mat-CuO NPs had a spherical shape with uniform dispersion in the size range of 20 to 40 nm. Average particle size of the PEGylated Mat-CuO NPs is 21.82 nm. The structure of PEGylated Mat-CuO NPs had a monoclinic crystalline structure. As a result, the synthesized *PEGylated* Mat-CuO NPs may be used for various biological applications such as nanocarriers, nanoagents, and nanocoating materials.

ACKNOWLEDGMENTS

This study was funded by Scientific Research Projects Coordination Unit of Istanbul University-Cerrahpasa. Project number: FYL-2021-36085.

REFERENCES

[1] Mohammed Ali, M. J.M, Radhy, M.M. Mashkoor, S.J., Ali, E.M., Synthesis and characterization of copper oxide nanoparticles and their application for solar cell, Materials Today Proceedings, 60, 917- 921, 2022.

[2] Yadav, N., Bhagat, S., Singh, S. Surface modification of metal oxide nanoparticles to realize biological applications, Reference Module in Materials Science and Materials Engineeringi 2021.

[3] Waris, A., Din, M., Ali, A., Ali, M., Afridi, S., Baset, A., Ullah Khan, A., A comprehensive review of green synthesis of copper oxide nanoparticles and their diverse biomedical applications, Inorganic Chemistry Communications, 123,108369, 2021.

[4] Alhalili, Z., Green synthesis of copper oxide nanoparticles CuO NPs from Eucalyptus Globoulus leaf extract: Adsorption and design of experiments, Arabian Journal of Chemistry, 15, 103739, 2022.

[5] Badri, A., Slimi, S., Guergueb, M., Kahri, H., Mateos, X., Green synthesis of copper oxide nanoparticles using Prickly Pear peel fruit extract: Characterization and catalytic activity, Inorganic Chemistry Communications, 134, 109027, 2021.

[6] Pillai, R.R., Sreeşekshmi, P.B., Meera, A.P., Enhanced biological performance of green sythesized copper oxide nanoparticles using Pimenta dioica leaf extract, Materials Today Proceedings, 50, 163-172, 2022.

[7] Jamkhande, P. G., Ghule, N.W., Bamer, A.H., Kalaskar, M.G., Metal nanoparticles synthesis: An overview on methods of preparation, advantages and disadvantages, and applications, Journal of Drug Delivery Science and Technology, 53, 101174, 2019.

[8] Saravanan, A., Kumar, P.S., Karishma, S., Vo, D.V.N., Jeevanantham, S., Yaashikaa, P.R., George, C.S., A review on biosynthesis of metal nanoparticles and its environmental applications, Chemosphere, 264, 128580, 2021.

[9] Rezaeian, F.M., Zimmermann, B.F., Simplified analysis of flavanols in matcha tea, Food Chemistry, 373, 131628, 2022.

[10] Silva, T.M., Fracasso, D.S., Vargas Visentin, A.P., Cassini, C., Scariot, F.J., Danetti, S., Echeverrigaray, S., Moura, S., Touguinha, L.B., Branco, C.S., Salvador, M., Dual effect of the herbal matcha green tea (Camellia sinensis L. kuntze) supplement in EA.hy926 endothelial cells and Artemia salina, Journal of Ethnopharmacology, 298, 115564, 2022.

[11] Sequeira, M.C.M., Pereira, M.F.V., Aveliona, H.M.N.T., Caetano, F.J.P., Fareleira, J.M.N.A., Viscosity measurements of poly(ethyleneglycol) 400 [PEG 400] at temperatures from 293 K to 348 K and at pressures up to 50 MPa using the vibrating wire technique, Fluid Phase Equilibria, 496, 7-16, 2019.

[12] Hiremath, L., Nipun, S., Sruti, O., Kala, N.G., Aishwarya, B.M., Sonochemistry: Applications in Biotechnology, Sonochemical Reactions, 2020.

[13] Karakuş, S., Baytemir, G., Özeroğlu, C., Taşaltın, N., An ultra-sensitive smartphone-integrated digital colorimetric and electrochemical Camellia sinensis polyphenols encapsulated CuO nanoparticles-based ammonia biosensor, Inorganic Chemistry Communications, 143, 109733, 2022.

[14] Velsankar, K., Suganya, S., Muthumari, P., Mohandoss, S., Sudhahar, S., Ecofriendly green synthesis, characterization and biomedical applications of CuO nanoparticles synthesized using leaf extract of Capsicum frutescens, Journal of Environmental Chemical Engineering, 9, 106299, 2021.

[15] Rupashree, M.P., Soppin, K., Pratibha, S., Chethan, B., Cost effective photocatalytic and humidity sensing performance of green tea mediated copper oxide nanoparticles, Inorganic Chemistry Communications, 134, 108974, 2021.

[16] Sukumar, S., Rudrasenan, A., Nambiar, D. P., Green-Synthesized Rice-Shaped Copper Oxide Nanoparticles Using Caesalpinia bonducella Seed Extract and Their Applications, 5, 1040-1051, 2020.

[17] Ahmad, A., Khan, M., Khan, S., Luque, R., Abualnaja, K.M., Alduaij, O.K., Yousef, T.A., Bio-Construction of CuO Nanoparticles Using Texas Sage Plant Extract for catalytical degradation of Methylene blue Via Photocatalysis, Journal of Molecular Structure, 1256, 132522,2022.

[18] Saravanakumar, K., Shanmugam, S., Varukattu, N.B., MubarakAli, D., Kathiresan, K., Wang, M.H., Biosynthesis and characterization of copper oxide nanoparticles from indigenous fungi and its effect of photothermolysis on human lung carcinoma, Journal of Photochemistry and Photobiology B: Biology, 190, 103-109, 2019.

[19] Manoj, D., Saravanan, R., Santhanalakshmi, J., Agarwal, S., Gupta, V.K., Boukherroub, R., Towards green synthesis of monodisperse Cu nanoparticles: An efficient and high sensitive electrochemical nitrite sensor, Sensors and Actuators B. Chemical, 266, 873-882, 2018.

2nd International Natural Science, Engineering and Material Technologies Conference
Sep 15-17, 2022, İğneada-Kırklareli / TÜRKİYE

SYNTHESIS OF ULTRASOUND ASSISTED GREEN SILVER NANOPARTICLES AND COATING ON 316L STAINLESS STEEL WITH AIRBRUSH SPRAY TECHNIQUE

G. Karabulut[1], N. Beköz Üllen[1]

[1]*Department of Metallurgical and Materials Engineering, Faculty of Engineering, Istanbul University-Cerrahpasa, İstanbul, TÜRKİYE*

E-mail: gizem.karabulut@iuc.edu.tr

Abstract

In this study, novel PEGylated maca root extract-silver nanoparticles (PEGylated Mac-Ag NPs) were prepared using a green sonochemical method. The 316L stainless steel (SS316L) was coated with the prepared PEGylated Mac-Ag NPs using a low-cost and easy-to-use airbrush spray technique. The prepared PEGylated Mac-Ag NPs and coated SS316L with PEGylated Mac-Ag NPs were characterized to determine the surface morphology, crystal structure, and chemical functional groups using different methods such as scanning electron microscopy, transmission electron microscopy, ultraviolet-visible spectrophotometry, X-ray diffraction, Fourier transform infrared spectroscopy, X-ray photospectrometry, surface roughness, and profilometry. According to the surface characterization results, it was clear that the sono-synthesized PEGylated Mac-Ag NPs had a spherical-agglomerated aggregate structure in the particle range of 30 to 50 nm. Furthermore, the surface of the coated 316L stainless steel had a uniform particle distribution with spherical and particle diameters of less than 50 nm. Consequently, it was observed that surface of the SS316L was covered with nano-sized PEGylated Mac-Ag NPs using a green chemistry approach. The proposed synthesis and coating process were promise to use a simple and green process to fabricate advanced nanomaterials in biomedical applications.

Keywords: Silver nanoparticle, green chemistry, airbrush spray coating, sonochemical synthesis

1. INTRODUCTION

In recent years, M/MO nanoparticles have been widely used in coating applications of metallic surfaces in order to improve the surface properties and provide various functional properties such as mechanical, corrosion resistance[1], and antipathogenic properties [1]. Silver nanoparticles (Ag NPs) based coatings have been widely used in recent years due to the antipathogenic properties of silver [2,3], as well as its superior physicochemical and biological properties such as conductivity and catalytic properties [4]. There are many studies in the literature where Ag NPs-based coatings are coated on the metal surface [5,6] and other substrates such as glass [7], polymer [8], etc. In these studies, coating methods such as dip [5,6], sol-gel [9], atomic layer deposition [10], physical vapor deposition [11], and electro-deposition [12] were used. The methods used in these studies in the literature are difficult, expensive, and long-term processes. In this study, the goal is to ensure that biocompatible and synthesized with green chemistry Ag NPs were coated homogeneously to the metallic surface in a cheap, fast, and greener way. For this purpose, Ag NPs were synthesized using the green sonochemical method in this study. In this method, nanoparticle formation is carried out by acoustic cavitation using ultrasonic sound waves [13]. It is a green synthesis method to reduce Ag ions to form Ag NPs without the use of chemical reducing or hazardous stabilizing agents [14]. However, Ag NPs tend to agglomerate in the aqueous solutions. This causes them to be growing over time, reduce their surface area, and thus reduce their effectiveness. In order to prevent this, stabilizer agents should be used and nanoparticles should be control the size range [15]. In the literature, various natural polymers such as chitosan, pectin, starch, and alginate and various polymers such as poly (methyl methacrylate) (PMMA), polyvinyl alcohol (PVA), and PEG (Polyethylene Glycol) are used in the synthesis of Ag NPs. In recent years, the use of plant extracts as stabilizing and reducing agents has become a widespread trend due to their being natural and biocompatible [16]. In this study, fully biocompatible green maca root (*Lepidium Meyenii*) and Polyethylene Glycol (PEG) were used as stabilizers. Maca is a type of plant that has been used by people for about 2000 years and is called a medicinal plant [17]. PEG is a highly water-soluble, non-toxic, biochemically stable, low-cost, and biocompatible polymeric material [18]. For the first time in the literature, this study deals with the coating of a plant extract-based nanobiocomposite on SS316L surface by airbrush spray technique. The surface characterization and functional groups of PEGylated Mac-Ag NPs and coated surface were determined by various techniques Scanning electron microscopy (SEM), transmission electron microscopy (TEM), Fourier

transform infrared spectrophotometry (FT-IR), UV-Visible spectrophotometry (UV-Vis), X-ray photoelectron spectrophotometry (XPS), X-Ray diffraction (XRD), and profilometer.

2. MATERIAL AND METHODS

2.1. Materials

Maca root powder (*Lepidium meyenii*) was purchased from Arifoğlu Company (Turkey). Sodium hydroxide (NaOH) was purchased from Merck Company (Germany). The filter paper (Whatman® qualitative paper, diameter: 25 mm) and silver nitrate ($AgNO_3$, purity: ≥99.0%) were purchased from Sigma Aldrich Company (Germany). All chemicals and reagents were used without further purification. SS316L disks were obtained from a bar with a length of 1 m in 27 mm diameter (Birçelik Company, Istanbul, Turkey). The chemical composition of the SS316L was 0.014 w. %C, 0.437 w. %Si, %, 10.091 w.% Ni, 16.581 w.% Cr, 2.048 w.% Mo, 0.326 2.% Cu, 1.317 w.% Mn, 0.024 w.% S, 0.025 w.% P, 0.041 w.% N, and balance-Fe.

2.2. Preparation of PEGylated Mac-Ag NPs and PEGylated Mac-Ag NPs coated SS316L

Maca root powders were washed by several times to remove dust and impurities, and then dried in a vacuum oven at 70 °C for 5 h. 5 g of the maca root powder was added to 100 mL of distilled water and mixed at 500 rpm for 10 min. Then, it was kept in a closed sterile container in a dark environment at 27 °C for 3 days. Finally, the sample was decanted and filtered with 0.45-µm retention of sterile syringe filter, so that maca extract was obtained. 0.1 g of PEG was added to 20 mL of prepared maca root extract and mixed at 500 rpm for 10 minutes. 0.1 g of $AgNO_3$ was dissolved in 50 mL of distilled water and stirred for 10 minutes at 27 °C. 0.2 g of NaOH was dissolved in 50 mL of distilled water and stirred for 10 minutes at 27 °C. $AgNO_3$ and NaOH solutions were added drop by drop into the PEGylated maca solution and sonicated at %50 amplitude for 30 min at 27 °C. Finally, the prepared PEGylated Mac-Ag NPs was filtered using a 0.22- µm retention of sterile syringe filter.

The stainless steel bar was sliced with a computer numerical control (CNC) machine to obtain 2 mm in thickness discs. The cutting was performed using DNMG 150608 PM 1525 insert while a cutting speed 10 m/min, a feed rate of 0.25 mm/rev and a cutting depth of 1 mm. After the cutting process, all samples were ultrasonicated for 10 min in ethanol-acetone solution, and dried for 10 min at 60 °C in the vacuum oven. Then, an airbrush compressor kit (piston type/ Model Number: AS186) was used for the coating process. The

schematic view of the coating process is given in Figure 1. During spraying, a plastic pipe of 100 mm long and 25 diameter was used in order to spray from an equal distance and to prevent it from spreading around. After the spray gun was placed with the plastic pipe, the distance of the nozzle to the surface was measured as 75 mm. The spraying was carried out at 3 bar pressure for 4 seconds. The process was carried out only once and the surfaces were completely coated.

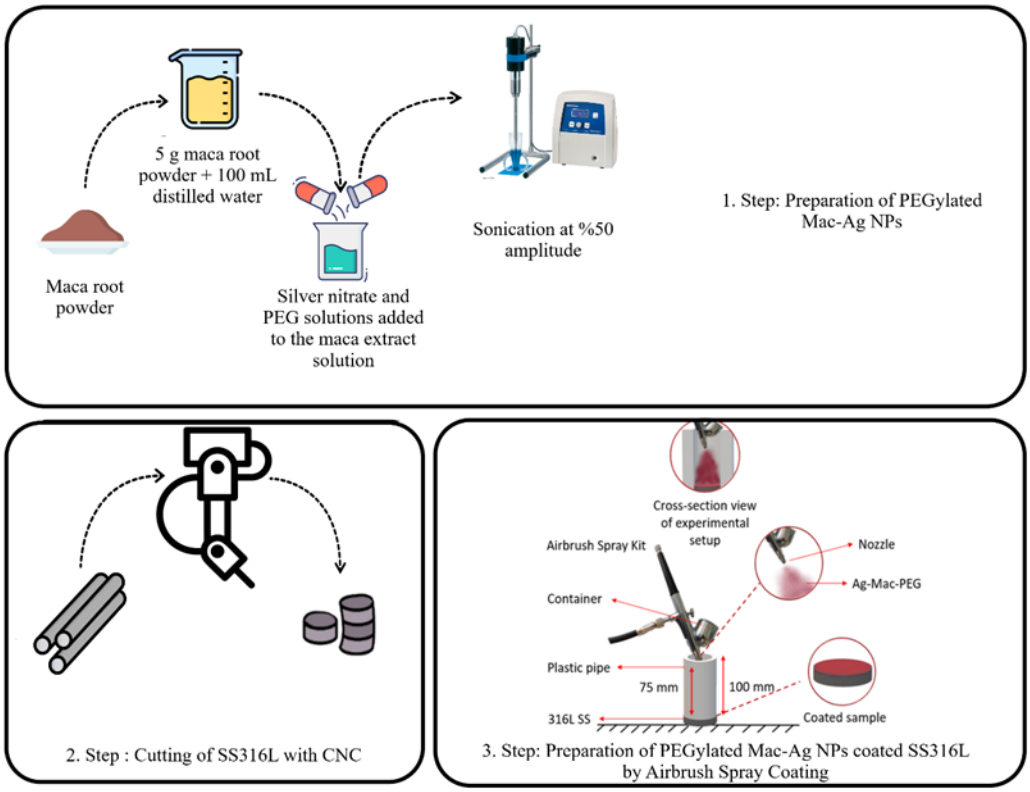

Figure 1. Schematic diagram of the process stages of the preparation of PEGylated Mac-Ag NPs coated SS316L

2.4. Characterization of PEGylated Mac-Ag NPs and PEGylated Mac-Ag NPs coated SS316L

The surface morphology and topography of synthesized PEGylated Mac-Ag NPs and coated samples were characterized by SEM (Zeiss-Sigma 300 device). Particle size and morphology of the PEGylated Mac-Ag NPs were characterized by TEM in a high vacuum mode at 100 kV (Hitachi High Tech HT7700). The absorbances measurement of the PEGylated Mac-Ag NPs was made by a double-beam UV–Vis spectrophotometer with a UVWin 5 Software (T + 80 model, PG Instrument). Functional groups of the PEGylated Mac-Ag NPs were obtained with FT-IR analysis (Perkin Elmer, Spectrum Two model) in the region

of 4000–400 cm^{-1} frequency range with a resolution of 4 cm^{-1} and 8 scans. XRD analysis was performed to determine crystalline structure of the PEGylated Mac-Ag NPs by Rigaku D/Max2200/PC device with Cu-Kα radiation from 10° to 80 at 40 kV and 15 mA. XPS analysis was performed to determine the elemental composition and chemical properties of the PEGylated Mac-Ag NPs as a coating solution by Specs-Flex device with Al-Kα radiation. The surface roughness, distribution, and thickness of the PEGylated Mac-Ag NPs coating on the surface were examined by Kla Tencor Stylus Profiler P7 profilometer device.

3. RESULTS AND DISCUSSION

3.1. Characterization of PEGylated Mac-Ag NPs

The surface morphology of the synthesized PEGylated Mac-Ag NPs was characterized by SEM and TEM techniques. In Figure 2, SEM (a) and TEM (b) images of the PEGylated Mac-Ag NPs were presented. According to the SEM image, PEGylated Mac-Ag NPs have homogeneous distribution with a spherical shape and in the particle size range of 10-40 nm. As a result of TEM, it was observed that the Mac-PEG structure, which is the matrix phase, showed a heterogeneous distribution, and the Ag NPs were dispersed in small sized and acceptable forms on the Mac-PEG matrix. The results show that the nanobiocomposite structure of PEGylated Mac-Ag NPs has been successfully formed. The results are consistent with previous studies on the sonochemical synthesis of the plant-derived Ag NPs [19].

UV-Vis analysis was performed to obtain surface plasmon resonance behavior of the PEGylated Mac-Ag NPs. UV-Vis spectra of the synthesized PEGylated Mac-Ag NPs were given in Figure 3(a). According to the literature, the formation of Ag NPs with surface plasmon resonance behavior forms a peak region of 400-460 nm [20]. As seen in Figure 3(a), Ag^0 in the nanobiocomposite were formed a peak at 422 nm. This proves the presence of Ag NPs in the structure. The FTIR analysis of PEGylated Mac-Ag NPs was performed determine the functional groups of nanobiocomposite. FTIR spectra of the PEGylated Mac-Ag NPs was given in Figure 3 (b). The characteristics peaks were found at 3303,46 cm^{-1} (O-H stretching), 2971,77 cm^{-1} (C-H stretching), 1557,24 cm^{-1} (C=O), 1396,21 cm^{-1} (O-H bending), and 1054,87 cm^{-1} (C-O stretching), respectively. The functional groups of nanobiocomposite containing polyphenol compounds are compatible with the literature [21]. XRD analysis was performed to examine the crystalline structure of the nanobiocomposite. XRD pattern graph of the PEGylated Mac-Ag NPs was given in Figure 3(c). As shown in the graph, the peaks were formed 2θ= 38°, 44.1°, 64.5°, and 77.4°. These peaks are corresponding to the plane of (1 1 1), (2 0 0),

(2 2 0), and (3 1 1), respectively. According to this result, the silver crystal has a face-centered cubic (FCC) structure. The peaks were formed at 2θ=27.7°, 29.2°, and 32.2° originate from the organic phases in the nanobiocomposite structure [19].

To obtain elemental composition and oxidation states of the synthesized PEGylated Mac-Ag NPs XPS analysis was performed. The binding energies of the PEGylated Mac-Ag NPs at 283.50 eV for C_{1s}, 531.10 eV for O_{1s}, and 399.00 eV for $Ag_{3d/2}$ are corresponded to in Figure 4(a-d). In Figure 4(b) the O_{1s} spectra observed at 531.10 eV was corresponded to carboxylate group. In C_{1s} spectrum (Figure 5(c)) was observed a single peak at 283.50 eV, this peak indicates the nonoxygenated ring carbon (C-C) and arises from compounds of phytochemical of maca root extract [19].

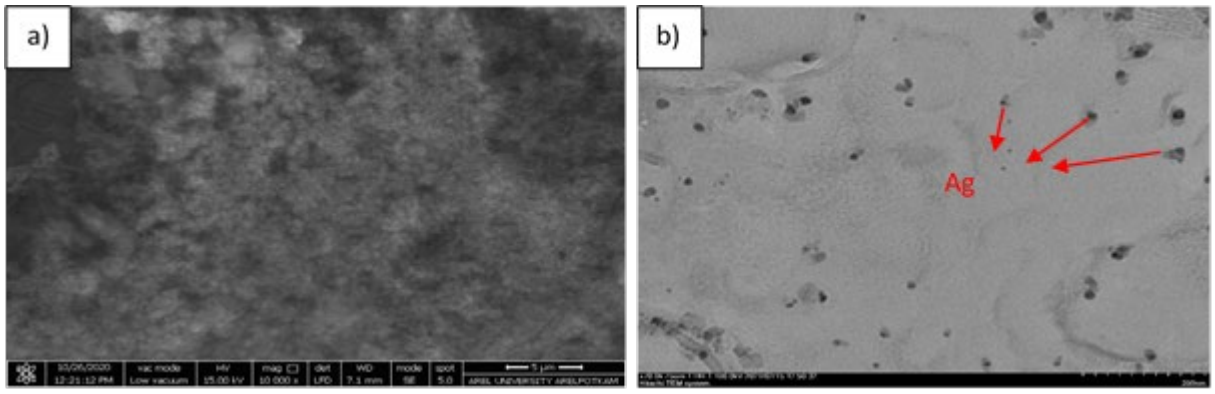

Figure 2. (a) SEM and (b) TEM images of the PEGylated Mac-Ag NPs

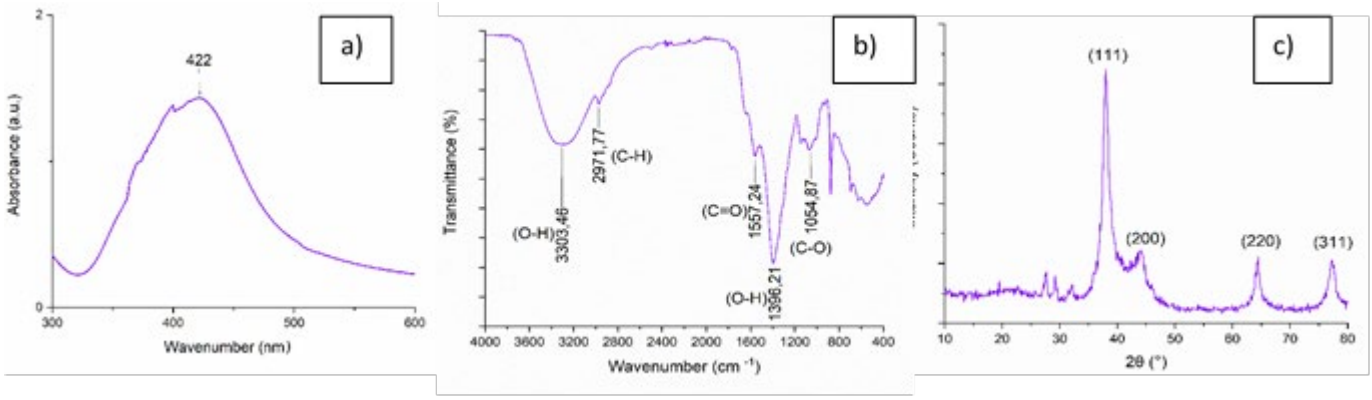

Figure 3. (a) UV-Vis, (b) FT-IR, and (c) XRD spectrum of the PEGylated Mac-Ag NPs

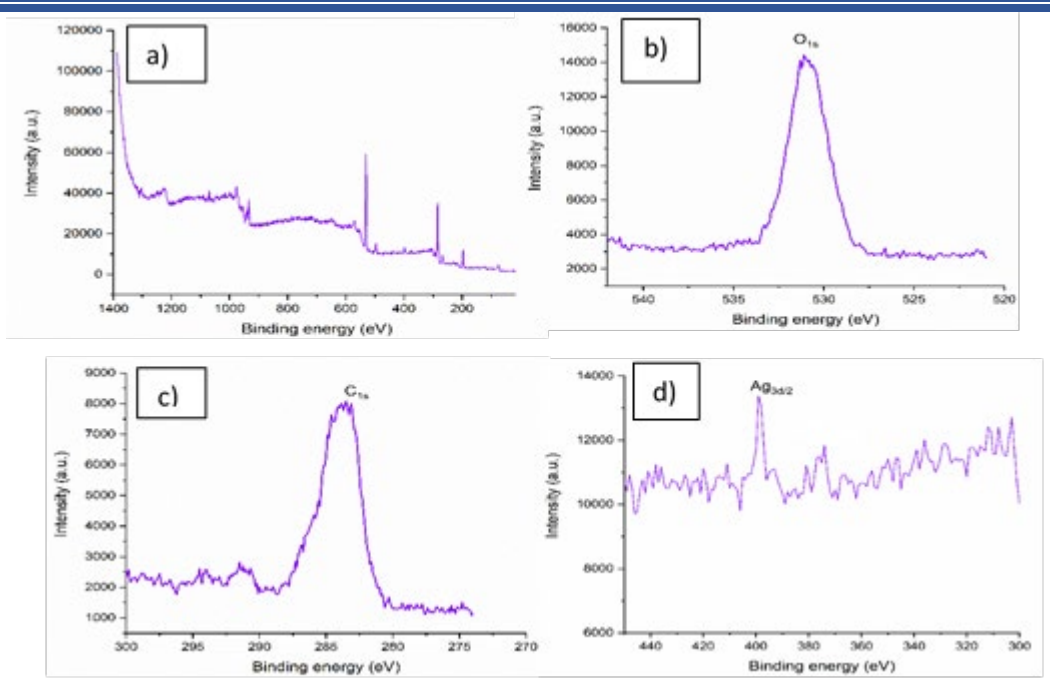

Figure 4. XPS spectrum of PEGylated Mac-Ag NPs (a) XPS survey spectrum, (b) binding energy spectrum for O_{1s}, (c) binding energy spectrum for C_{1s}, and (d) binding energy spectrum for Ag_{3d}

3.2. Characterization of PEGylated Mac-Ag NPs coated 316L stainless steel

SEM images of the coated samples with Airbrush spray coating technique are given in Figure 5(a-d) at different magnifications. According to the SEM results, PEGylated Mac-Ag NPs coating was done successfully. In Figure 5(a), the layers seen on the coating surface are the cutting lines formed during the cutting process on the steel surface. At lower magnifications (Figure 5(a-b)), the PEGylated Mac-Ag NPs coating has a branched structure. At larger magnifications (Figure 5(c-d)), the structural form of the coating material is fully visible. It is also seen that the PEGylated Mac-Ag NPs are homogeneously dispersed on the substrate surface, and Ag NPs sizes are in the range of 30-40 nm. The distribution and near-spherical shape of the Ag NPs on the SS316L substrate are consistent with the works on metallic surfaces coated with Ag NPs [23,25]. In terms of improving the resistance properties of the coating, the homogeneous distribution of Ag NPs on the SS316L substrate is important. Jothi et al. reported that the homogeneous distribution of nanoparticles on the stainless steel surface coated with Ag NPs increases the resistivity properties of the substrate [9].

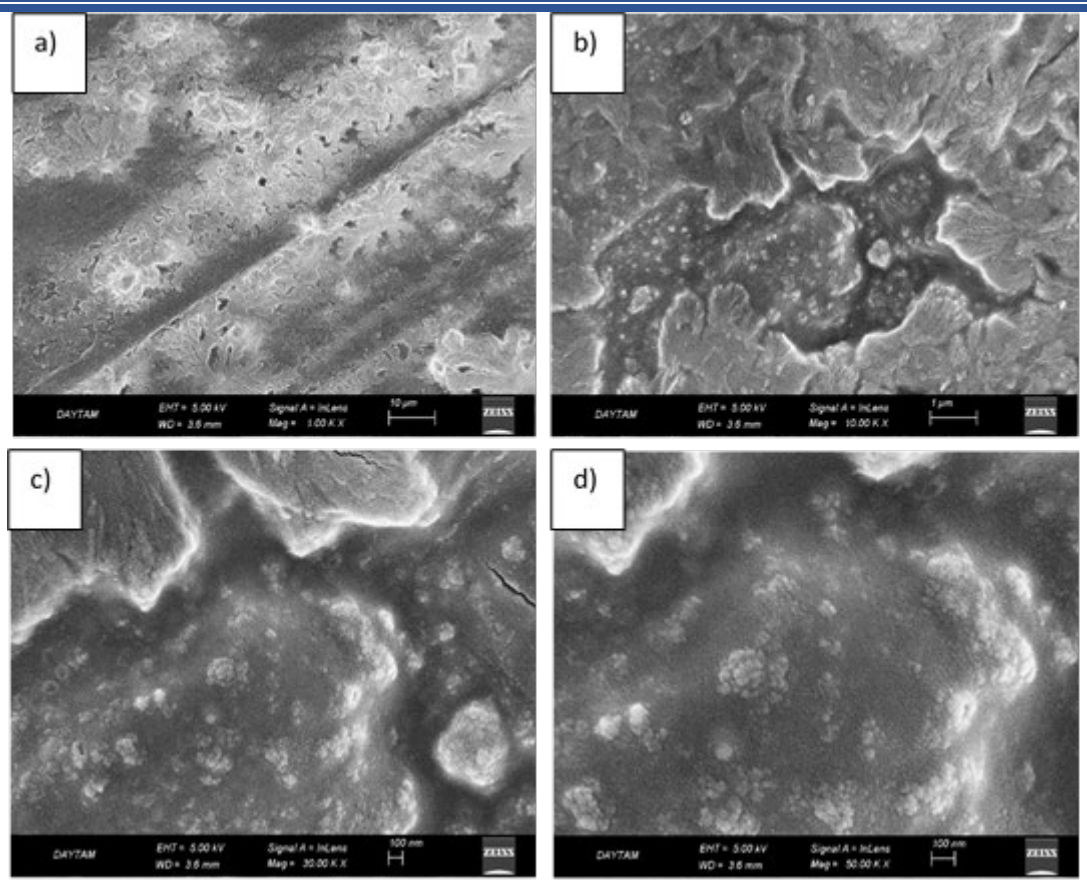

Figure 5. SEM images of the PEGylated Mac-Ag NPs coated 316L stainless steel at different magnifications (a) x100, (b) x10.000, (c) x30.000, and (d) x50.000

The surface roughness, distribution, and thickness of the PEGylated Mac-Ag NPs coating on the steel surface were examined by a profilometer. The 3D view of the coating morphology was given in Figure 6. As can be seen, the PEGylated Mac-Ag NPs coating is homogeneously distributed on the surface of SS316L. Similar to the SEM image (Figure 5 (a)), the cutting lines are also seen in the 3D images as a black region. The coating thickness was determined approximately 7.7 µm. Average surface roughness value of the coating was obtained approximately 9.021 nm. It can be seen from the figure that Ag NPs are coated on the SS316L surface as a single-layer and homogeneous structure. In the literature, this coating structure is defined as a "single-layer structure" [11]. Since the coating is carried out with nanoparticles, it is usual for the surface roughness to be at nanoscales.

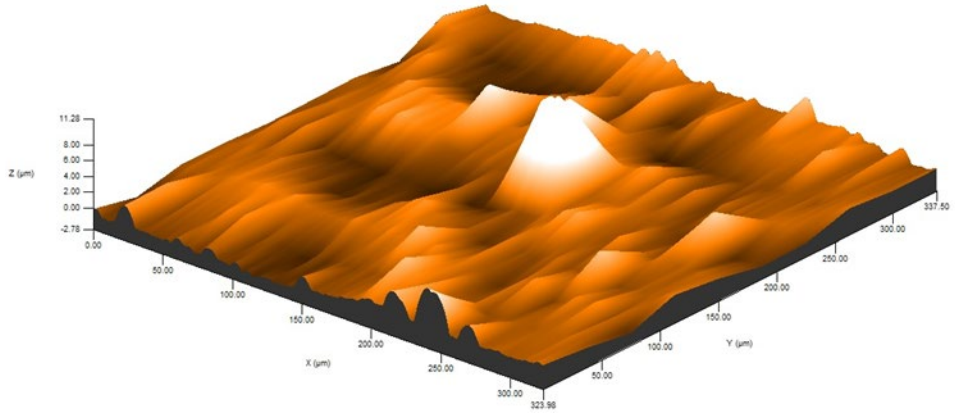

Figure 6. 3D view of the PEGylated Mac-Ag NPs coated 316L stainless steel

4. CONCLUSION

In this study, a novel green PEGylated Mac-Ag NPs coating was performed on the SS316L. The synthesized PEGylated Mac-Ag NPs are in FCC structure, covered by the organic phase, and have a size range of 10-40 nm. The coated PEGylated Mac-Ag NPs on the steel by airbrush spray method are homogeneously dispersed on the surface and their sizes are in the range of 30-40 nm. After coating, the roughness of the steel surface decreased. All of the manufacturing processes consist of green processes and products, so the synthesized nanostructure is suitable for biomedical applications. The coating technique used in the study is a preferable method to improve surface properties with nanoparticles. The surface modification of the SS316L was positively affected.

ACKNOWLEDGMENTS

This study was funded by Scientific Research Projects Coordination Unit of Istanbul University-Cerrahpasa. Project number: FYL-2021-36085.

REFERENCES

[1] Khan, M. A., Hussain, W., Hassan, N., Ilyas, M., Zill-e-huma, Abbas, S.Z., Hui, L., Fabrication of Ag nanoparticles on a Cu-substrate with excellent superhydrophobicity, anti-corrosion, and photocatalytic activity, 61, 6507-6521, 2022.

[2] Cai, Y., Luo, X., Maclean, M., Qin, Y., Duxbury, M., Ding, F., A single-step fabrication approach for development of antimicrobial surfaces, Journal of Materials Processing Technology, 271, 249-260, 2019.

[3] De Giglio, E., Cafagna, D., Cometa, S., Allegretta, A., Pedico, A., Giannossa, L.C., Sabbatini, L., Mattioli-Belmonte, M., Iatta, R., An innovative, easily fabricated, silver nanoparticle-based titanium implant coating: Development and analytical characterization, Analytical and Bioanalytical Chemistry, 405,805-816, 2013.

[4] Chen, D., Qiao, X., Qiu, X., Chen, J., Synthesis and electrical properties of uniform silver nanoparticles for electronic applications, Journal of Materials Science, 44, 1076-1081, 2009.

[5] Zhang, S., Liang, X., Gadd, G.M. Zhao, Q., A sol–gel based silver nanoparticle/polytetrafluorethylene (AgNP/PTFE) coating with enhanced antibacterial and anti-corrosive properties, Applied Surface Science, 535, 147675, 2021.

[6] Wang, B. B., Quan, Y. H., Xu, Z.M., Zhao, Q., Preparation of highly effective antibacterial coating with polydopamine/chitosan/silver nanoparticles via simple immersion, Progress in Organic Coatings, 149, 105967, 2020.

[7] Rajanandkumar, R., Synthesis and characterization of polymer encapsulated silver nanoparticle coatings for antibacterial effect, Materials Today Proceedings, 47, 1782-1786, 2021.

[8] Ohara, Y., Akazawa, K., Shibata, K., Hirota, T., Kodama, Y., Amemiya, T., Wang, J., Yamaguchi, T, Seed-mediated gold nanoparticle synthesis via photochemical reaction of benzoquinone, Colloids Surfaces A: Physicochemical and Engineering Aspects, 586, 124209, 2020.

[9] Jeeva Jothi, K., Balachandran, S., Palanivelu, K., Synergistic combination of Phyllanthus niruri / silver nanoparticles for anticorrosive application, Materials Chemistry and Physics, 279, 125794, 2022.

[10] Devlin-Mullin, A., Todd, N. M., Golrokhi, Z., Geng, H., Konerding, M. A., Ternan, N. G., Hunt, J. A., Potter, R. J., Sutcliffe, C., Jones, E., Lee, P.D., Mitchell, C.A., Atomic Layer Deposition of a Silver Nanolayer on Advanced Titanium Orthopedic Implants Inhibits Bacterial Colonization and Supports Vascularized de Novo Bone Ingrowth, Advanced Healthcare Materials, 6, 1700033, 2017.

[11] Alias, R., Mahmoodian, R., Abd Shukor, M. H., Development and characterization of a multilayer silver/silver-tantalum oxide thin film coating on stainless steel for biomedical applications, International Journal of Adhesion and Adhesives, 92, 89-98, 2019.

[12] Abdulsada, F.W., Hammood, A.S., Characterization of corrosion and antibacterial resistance of hydroxyapatite/silver nano particles powder on 2507 duplex stainless steel, Materials Today, Proceedings, 42, 2301-2307, 2021.

[13] Hiremath, L., Nipun, S., Sturi, O., Kala, N. G., Aishwarya, Sonochemistry: Applications in

Biotechnology, Sonochemical Reactions, 2020.

[14] Karakuş, S., Tan, E., Ilgar, M., Kahyaoglu, I.M., Şahin, Y.M., Mansuroglu, D.S., Ismik, D., Taslatin, N., Kilislioğlu, A., Preparation, Characterization, and Swelling Behavior of PEGylated Guar Gum @ Ag Nanoparticles, Sonochemical Reactions, 2019.

[15] Das, S., Bandyopadhyay, K., Ghosh, M. M., Effect of stabilizer concentration on the size of silver nanoparticles synthesized through chemical route, Inorganic Chemistry Communications, 123, 108319, 2021.

[16] Akalin, G.O., Oztuna Taner, O., Taner, T., The preparation, characterization and antibacterial properties of chitosan/pectin silver nanoparticle films, Polymer Bulletin, 79, 3495-3512, 2022.

[17] Chen, H., Han, Y., Jahan, I., Wu, S., Clark, B.C., Wiseman, J.S., Extracts of maca (Lepidium meyenii) root induce increased glucose uptake by inhibiting mitochondrial function in an adipocyte cell line, Journal of Herbal Medicine, 17-18, 100282, 2019.

[18] Hoffman, M.M., Polyethylene glycol as a green chemical solvent, Current Opinion in Colloid & Interface Science, 57, 101537, 2022.

[19] Manjamadha, V. P., Muthukumar, K., Ultrasound assisted green synthesis of silver nanoparticles using weed plant, Bioprocess and Biosystems Engineering, 39, 401-411, 2016.

[20] Aygün, A., Özdemir, S., Gülcan, M., Cellat, K., Şen, F., Synthesis and characterization of Reishi mushroom-mediated green synthesis of silver nanoparticles for the biochemical applications, Journal of Pharmaceutical and Biomedical Analysis, 178, 112970, 2020.

[21] Das, S.K. Behera, S., Patra, J.K., Thatoi, H., Green Synthesis of Sliver Nanoparticles Using Avicennia officinalis and Xylocarpus granatum Extracts and In vitro Evaluation of Antioxidant, Antidiabetic and Anti-inflammatory Activities, Journal of Cluster Science, 30, 1103-1113, 2019.

2nd International Natural Science, Engineering and Material Technologies Conference
Sep 15-17, 2022, İğneada-Kırklareli / TÜRKİYE

FOOD SECURITY AND DIGITALIZATION IN TURKEY AND IN THE WORLD

H. G. Ağca Küçükaydın[1], B. Çetin[1]

[1]*Department of Food Engineering, Faculty of Engineering, Kırklareli University, Kırklareli, TÜRKIYE*

E-mail: goknuragca@klu.edu.tr

Abstract

The increasing population and drought in the world, the pandemic and the subsequent war between Russia and Ukraine reveal the importance of the concept of food security. Despite the food crises and increasing global food demand, new technologies have been focused on in order to increase productivity in order to maintain quality and meet food needs in a sustainable manner. After the pandemic, the digitalization process, which will contribute to the sustainability, traceability of food supply, food safety and supply chain, has also accelerated. Starting from animal and agricultural production, studies should be carried out to increase the efficiency of food supply at all stages. Food security is the existence of the physical and economic conditions necessary for people to have access to safe and nutritious food to lead an active and healthy life. According to FAO, the four pillars of food security are availability, access, use and stability. On the other hand, the desire to produce safe food has led to the formation of the HACCP food safety system and the concept of traceability.

Today, people's orientation to quality and healthy foods while meeting their food needs creates new preferences. The consumer's search for maximum information about the product creates a different basis for digitalization. Digitalization, which is a "mega trend" with the demand of conscious consumers in today's marketing conditions, is changing the food industry as well as changing all sectors these days. This study reviews research and developments on food security and digitalization in Turkey and around the world.

Keywords: Food security, Food supply, Traceability, Digitalization

1. INTRODUCTION

Food production, food supply logistics and consumption based on plant and animal production have a high inclusiveness, especially human health, environmental health and economy. Today, the problems that arise in food supply have led researchers to conduct studies in this field and to make plans according to the population and changing world conditions. Food security is a measure of each individual's access to food, as well as the continuity of food production. Today, the integration of newly developing technologies into our lives makes our lives easier in many areas, as well as benefiting from the problem-solving effect.

1.1. Food Safety: In Turkey and In the World

Since the beginning of human history, food security has been one of the greatest concerns of society. Food security is directly related to the survival of society. The globalization of the world has led to an increase in food trade, that is, the way food follows in the world. Crises experienced as a result of globalization also affect the whole world. One of the 8 main headings, as the goal of the millennium, which the United Nations has set forth to increase the welfare of humanity, is to eliminate hunger and ensure food security [1, 2].

Agricultural production in Turkey has always been one of the priority issues. Although a policy of self-sufficiency was followed until recently, it has recently started to import basic agricultural products. Following the free market economy and increasing input costs are the main reasons. Turkey also takes its share from the global crises. As a result, the increase in food costs in recent years and the accompanying stocking constitute the biggest obstacle in ensuring food security [3]. TUIK data show that the rate of uncultivated agricultural land has been increasing from year to year. In fact, it is necessary to produce more in agriculture and livestock sectors today than yesterday. Due to the increase in inputs such as feed, fertilizer and diesel, not cultivating the lands and cessation of animal breeding will cause problems in the food supply for our country.

Although the percentage of hunger in the world remained constant for almost 5 years before the Covid-19 epidemic, it increased from 8.4% to 10.4% of the global population in 2020. In 2020, human life has been challenged in terms of food insecurity. The economic crises that have emerged in recent years directly and indirectly lead to food insecurity. Population growth, drought, cost increase in food production inputs (energy, etc.) as well as global political crises cause food insecurity. The estimated world population of 10 billion in 2050 shows how important it is to work on food security from now on, before it's too late [4-6].

1.2. Traceability in a Food Supply Chain

Traceability is at all stages from the production of the food to the consumption; It is the ability to trace the animal or vegetable source from which the food is obtained or a substance contained in it. It is a system that allows the product to be followed from production to the end consumer, including the production, distribution and import stages. Traceability consists of three basic elements. These are: identification of all products, components and stages; providing information about location movements and time and providing a system that can be associated with each other [7].

With the recent global crises that have led to food insecurity, the need for effective use of food resources and the potential risks that may arise in ensuring food safety should be followed. On the other hand, with the increasing awareness of the consumer, environmentalist, sensitive to animal welfare, sustainable agriculture and production and providing the information flow that the consumer needs have led to the development of the concept of traceability based on information technologies.

The application of food traceability depends on the multidimensional analysis of the product and which problems it will solve [8].

1.3. Digitalization in Food Industry

Advances in technology make food traceability possible with advanced data processing systems based on Radio Frequency Identification (RFID) and Wireless Sensor Network (WSN), a location tracking system such as the Global Positioning System (GPS), and smart software agents. The most common ones are barcode system and RFID technologies. Barcode technology can carry a number of data that may be important in retail and supply chain logistics. The transferred data file may not meet different purposes and requirements. RFID, on the other hand, provides the data flow with radio frequency, and provides traceability with a microprocessor carrying the data of the object and a tag equipped with an antenna integrated into the microprocessor. It contributes to food safety and security by providing the necessary real-time information flow throughout the food production and distribution chain [8-10].

2. CONCLUSION

Recently, food security is among the prominent problems all over the world. Global political crises, increasing demand with population, climate change and decreasing water resources have effects on agriculture. On the other hand, income level ranks first among the causes of food insecurity in developing and developed countries. When all these problems are considered, it becomes a necessity to produce a realistic and progressive solution. It is foreseen that digitalization will contribute to supply-demand management and the problem can be solved without growth and supported by legislation. Digitalization has the potential to be a strategic solution for overcoming problems such as income differences, stocking problems, disruption of supply-demand balance, malfunction in production plans that cause food insecurity in Turkey.

Primary processors are required to work under contract with farmers while ensuring that the digitization steps for food security are completed. They need to digitize labeling and recording, starting at the farm level. It is essential to invest in digitalization by private institutions or organizations with government support and to organize trainings. Digitization of each stage and process in food production is important [11].

Achieving the aim in food safety can be achieved with results-oriented solutions that are compatible with social and economic policies at the macro level [12]. In addition, the average age of those working in the agriculture and livestock sectors in our country should be lowered, and plans, projects and policies should be produced that will willingly direct young people to these areas.

REFERENCES

[1] N. Demirbaş, "Dünyada ve Türkiye'de Gıda Israfını Önleme Çalışmalarının Değerlendirilmesi Evaluation of Food Waste-Prevention Actions in the World and in Turkey," 2018. [Online]. Available: https://www.researchgate.net/publication/326989181

[2] Y. Ataseven, H. Arısoy, and Ö. Köksal, "Türkiye'de Tarım Politikalarının Gıda Güvencesi ve Güvenliği Açısından Değerlendirilmesi." [Online]. Available: http://www.dunyagida.com.tr;

[3] E. Kızıl, "Türkiye'de Tarımsal Teşvik Sisteminin Yapısı, Sorunları ve Çözüm Önerileri: Konya İli Örneği," Necmettin Erbakan Üniversitesi, Konya, 2021.

[4] "How to Sustainably Feed 10 Billion People by 2050, in 21 Charts," https://www.wri.org/insights/how-sustainably-feed-10-billion-people-2050-21-charts, (accessed Sep. 23, 2022).

[5] Pietro Gennari, "Tracking progress on food and agriculture-related SDG indicators 2021," www.fao.org/sdg-progress-report/2021/en/, 2021. www.fao.org/sdg-progress-report/2021/en/ (accessed Sep. 23, 2022).

[6] Ö. C. Niyaz and İ. H. İnan, "Türkiye'de Gıda Güvencesinin Mevcut Durumunun Değerlendirilmesi," Adnan Menderes Üniversitesi Ziraat Fakültesi Dergisi , vol. 13, no. 2, pp. 1–7, 2016.

[7] E. Yaralı, "Gıda zincirinde izlenebilirlik," Harran Tarım ve Gıda Bilimleri Dergisi, pp. 108–119, Mar. 2019, doi: 10.29050/harranziraat.394856.

[8] M. M. Aung and Y. S. Chang, "Traceability in a food supply chain: Safety and quality perspectives," Food Control, vol. 39, no. 1. Elsevier BV, pp. 172–184, 2014. doi: 10.1016/j.foodcont.2013.11.007.

[9] B. Keleş and G. Ova, "Gıda Tedarik Zinciri Yönetiminde Bilgi Teknolojileri Kullanımı," Adnan Menderes Üniversitesi Ziraat Fakültesi Dergisi, Jul. 2020, doi: 10.25308/aduziraat.658756.

[10] A. Yalçın Melikoğlu and Ö. Kızılırmak Esmer, "Gıda Güvenliğinin Sağlanmasında Radyo Frekanslı Tanımlama Teknolojisinin Rolü," Akademik Gıda, vol. 13, no. 1, pp. 72–80, 2015, [Online]. Available: http://www.academicfoodjournal.com

[11] Z. Cebeci, "Gıda İzlenebilirliğinde Bilgi Teknolojileri," Nov. 2006, pp. 189–195.

[12] G. Koç and A. Uzmay, "Gıda Güvencesi ve Gıda Güvenliği: Kavramsal Çerçeve, Gelişmeler ve Türkiye," 2015.

USABILITY OF MEDICAL TEXTILES WITH PREPREG COMPOSITE TEXTILES

H. Şen

Edirne Vocational School of Technical Sciences / Department of Textile, Clothing, Shoes and Leather, Trakya University, Edirne, TÜRKİYE

E-mail: hayrisen@trakya.edu.tr

Abstract

Medical textiles covers an area of technical textiles in 12 different areas. Technical textiles provide a very simple product with the addition of specific, useful, ergonomic and desired different features, thus providing a product with high added value. Technical textiles are also widely used in the use of medicine and hygiene products. With the development of synthetic fibers, the need for raw materials in the field of technical textiles can be met very quickly, so the production of disposable products in this field has been given importance. This is due to the increase in fiber diversity. The use of non-woven surfaces with woven and knitted surfaces has increased the ergonomic properties of the products. However, more specific medical textiles; For example, it is important to process medical textiles with prepreg composite materials in order to develop protective lead aprons for x-rays and to expand their usage areas. In this study; The usability of medical textiles with prepreg composite materials in specific productions is emphasized.

Keywords: Technical textiles, Medical textiles, Prepreg composites, Nano fibers.

1. INTRODUCTION

Medical textiles covers an area of technical textiles in 12 different areas. Technical textiles provide a very simple product with the addition of specific, useful, ergonomic and desired different features, thus providing a product with high added value. Technical textiles are also widely used in the use of medicine and hygiene products. For this reason, technical textiles have a wide usage area.

With the development of synthetic fibers, the need for raw materials in the field of technical textiles can be met very quickly, so the production of disposable products in this field has been given importance. This is due to the increase in fiber diversity. Especially; The importance of recyclable textile fibers is also emerging. Additionally; The use of non-woven surfaces with woven and knitted surfaces has increased the ergonomic properties of the products.

It can be produced from a very simple and inexpensive product such as bandage from technical textiles. Moreover; very specific, complex and expensive products such as artificial tendons and vessels can be produced. The group produced to meet specific needs is high performance technical textiles [1].

Technical textiles are characterised as semi-finished or finished materials and textile products, manufactured for their performance and added value functions rather than for their appearance and feel [2].

In the present study, the usability of medical textiles with prepreg composite materials in specific productions is emphasized.

2. TECHNICAL TEXTILES & MEDICAL TEXTILES

In general, brief explanations of these classifications can be made as follows:

1) Medtech: Medical and hygienic textiles

2) Mobiltech: Textiles used in all kinds of land, sea, air vehicles and space industry

3) Protech: Textiles used for individual and collective protection

4) Buildtech: Construction and building textiles

5) Indutech: Textiles for filtration, transport and other industrial purposes

6) Geotech: Textiles used in underground civil engineering and landscape architecture

7) Agrotech: Textiles used in agriculture, aquaculture, horticulture and forestry

8) Sportech: Sports and leisure textiles

9) Hometech: Furniture, home textiles and technical components of flooring

10) Clothtech: Technical components of shoes and clothing

11) Packtech: Packaging textiles

12) Oekotech: Textiles for ecological and environmental purposes [3].

Worldwide; The largest export market for technical textile products, which has a total export value of $1.5 billion, is the European Union countries with a 50.8% share and an export value of $786.8 million. According to the records of exporters' associations (2018); when the exchange rates of exports of textile ındustry products on the basis of product groups are examined, the highest export increase rate was recorded in technical textile products with 9.2%, and the highest export decrease rate was recorded in fiber products with 6.2% [6].

Prepreg; Pre-impregnated carbon, glass or aramid fibres and etc. Prepreg composite and technical textiles can be prepared using the hand lay-up method. In particular, it is tried to produce products with high ergonomic features, which are produced within the scope of medical textiles and are inexpensive.

Some technological features have made glass fibers extremely important in our time. In particular, the fact that it does not pass heat, is very resistant to heat, and prevents x-rays and radiation rays is one of them. For example, awning, curtain, apron, tablecloth, furniture face, helmet, dress, etc. against rays and fires. The production of protective articles and fabrics such as These articles and fabrics do not ignite with lit cigarette butts and matches. Likewise, they are used in the manufacture of life-saving boats and fire-protective items in oil tanker ships [4].

All the textile materials used in health and hygiene applications, in both consumer and medical markets. These are a well defined band of products with considerable variation in performance and unit value [5].

The glass prepreg material can be produced in certain layers and with a lead layer on the front and back surfaces. It can be produced with radiation-proof plates, with the help of glass prepreg material in a certain layer and with a lead layer on the front and back surfaces. In this way, much more ergonomic products that can be used in operating rooms may emerge.

If we examine the Production Flow Chart of Technical Textiles according to the table,

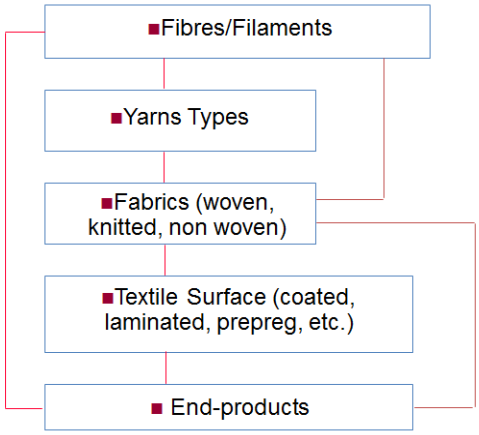

Figure 1. Production Flow Chart of Technical Textiles

Few examples of medical textiles;

Figure 2. X-Ray radiation protective front protection; apron, bonnet, mobile curtain [8]

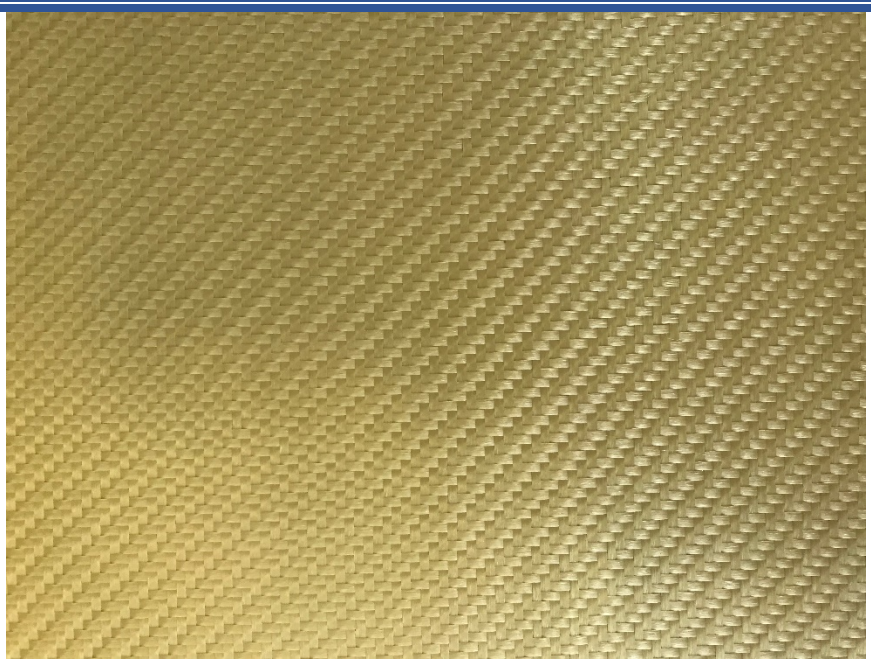

Figure 3. Prepreg plate

3. CONCLUSION

However, more specific medical textiles; For example, it is important to process medical textiles with prepreg composite materials in order to develop protective lead aprons for x-rays and to expand their usage areas.

According to this method, with the help of prepreg materials that can be used in medical textiles, more ergonomic manufacturability and more effective use of X-Ray radiation shields will be ensured. As a result of the studies, lighter preservatives can be obtained in these products.

As a result of this study; It has been tried to focus on the use of medical textiles in technical textiles and their usability with prepreg materials.

REFERENCES

[1] Mecit, D., Ilgaz, S., Duran, D., Başal, G., Gülümser, T., Tabakçıoğlu, I., Teknik Tekstiller ve Kullanım Alanları 1-2, Tekstil ve Konfeksiyon, 2/2007.

[2] Shishoo, R., Technical Textiles, An overview of the State of the Art, 2019.

[3] Horrocks, A. R., Anands, C., Teknik Tekstiller El Kitabı (Technical Textiles Handbook), The Textile Institute, Türk Tekstil Vakfı, 2003.

[4] Özdemir, D., diren Mecit, H., Seventekin, N., Öktem, T., Cam Lifleri, Tekstil ve Konfeksiyon, 1/2006.

[5] National Composites Network, Technical Textiles and Composite Manufacturing.

[6] T. C. KALKINMA BAKANLIĞI KALKINMA PLANI ON BİRİNCİ (2019-2023), Tekstil-Deri-Hazır Giyim Çalışma Grubu Raporu, Ankara,2018.

[7] http://www.technica.net/tessilitecnici/rel20011107/Nemoz.pdf.

[8] https://olgunmedikal.com/urun/om-x-ray-radyasyondan-koruyucu-on-koruma-onluk/

2nd International Natural Science, Engineering and Material Technologies Conference
Sep 15-17, 2022, İğneada-Kırklareli / TÜRKİYE

USABILITY OF SPORTS AND LEISURE TIME (RECREATION) TECHNICAL TEXTILES WITH PREPREG COMPOSITE TEXTILES

H. Şen

Edirne Vocational School of Technical Sciences / Department of Textile, Clothing, Shoes and Leather, Trakya University, Edirne, TÜRKİYE

E-mail: hayrisen@trakya.edu.tr

Abstract

Prepreg materials are composite fabrics that are pre-impregnated with resin. Technical textiles are located in 12 different fields. Sports and leisure time (recreation) technical textiles reveal an ergonomic and high added value product with the desired features of a very simple product [2]. Especially thanks to the very high strength aramid based kevlar fabrics, carbon prepreg fabrics, glass fiber and other synthetic fiber added prereg composites, great progress has been made both for the production of sports equipment and for clothing and equipment used in the realization of sports and recreational activities. We can attribute this to the development of synthetic fibers. Examples of the development of helmets, racing cars, racing bikes, canoe hulls, sports shoes, walking shoes, swimming fins, tennis rackets, hockey sticks, grass pitches, sleeping bags, camping equipment and other sports and leisure (recreation) technical textiles used in speed sports constitutes. In this study; The usability of sports and leisure time (recreation) technical textiles with prepreg composite materials was emphasized.

Key Words: Technical textiles, Sports and leisure time (recreation) technical textiles, Prepreg composites.

1. INTRODUCTION

Sports and leisure time (recreation) technical textiles reveal an ergonomic and high added value product with the desired features of a very simple product. Sports and recreation textiles are high value-added products with specific and targeted customers. Especially in countries with high purchasing power and producing these products, customer potential is high.

Especially thanks to the very high strength aramid based kevlar fabrics, carbon prepreg fabrics, glass fiber and other synthetic fiber added prereg composites, great progress has been made both for the production of sports equipment and for clothing and equipment used in the realization of sports and recreational activities. We can attribute this to the development of synthetic fibers. Examples of the development of helmets, racing cars, racing bikes, canoe hulls, sports shoes, walking shoes, swimming fins, tennis rackets, hockey sticks, grass pitches, sleeping bags, camping equipment and other sports and leisure (recreation) technical textiles used in speed sports constitutes.

In this study; The usability of sports and leisure time (recreation) technical textiles with prepreg composite materials was emphasized.

2. TECHNICAL TEXTILES & SPORTS AND LEISURE TIME (RECREATION)

Technical textiles are located in 12 different fields. Prepreg materials are composite fabrics that are pre-impregnated with resin.

In general, brief explanations of these classifications can be made as follows:

1) Medtech: Medical and hygienic textiles
2) Mobiltech: Textiles used in all kinds of land, sea, air vehicles and space industry
3) Protech: Textiles used for individual and collective protection
4) Buildtech: Construction and building textiles
5) Indutech: Textiles for filtration, transport and other industrial purposes
6) Geotech: Textiles used in underground civil engineering and landscape architecture
7) Agrotech: Textiles used in agriculture, aquaculture, horticulture and forestry

8) Sportech: Sports and leisure textiles

9) Hometech: Furniture, home textiles and technical components of flooring

10) Clothtech: Technical components of shoes and clothing

11) Packtech: Packaging textiles

12) Oekotech: Textiles for ecological and environmental purposes [3].

Sports textiles; It is an application area that includes sports and leisure clothes, sports equipment and tools [3].

These technical textiles are produced especially in order to meet the needs of sports branches. Because; Textiles used in every sport branch require different ergonomic features. Thanks to their superior performance, sports and recreation textiles contribute to both the athlete and the equipment used by the athlete. Moreover; If it is necessary to define the concept of recreation, it is the activities performed voluntarily, resting and renewing the person after compulsory work and activities.

When we look at sports and recreational activities according to the figure 1;

Figure 1. Sports and recreational activities

Prepregs are; Pre-impregnated carbon, glass or aramid fibers etc. Prepreg composite and technical textiles can be prepared using the hand lay-up method.

Few examples of sport and leisure time (recreation) technical textiles;

Figure 2. Carbon fiber swimming pallet and ice hockey stick [1]

Figure 3. Carbon prepreg

When we examine the reasons for preference of sports products, the most effective factor is the choice of brand that affects consumer behavior. For this reason, each brand enters the competition of innovative production in its own lane. It currently provides this with prepreg materials. In this way, more useful and high performance sports and recreation technical textiles can be produced. The use of specialty fibers together with prepreg materials also provides a wider use of these materials.

For example, CoolMax; It is a special fiber type that is durable, has a low pilling level and keeps the wearer dry and comfortable. It has the ability to easily remove moisture from the body. Thanks to this feature, the performance of the athlete increases by getting rid of factors such as sweat and jersey weight, thanks to the fabrics in which the fiber is used [5].

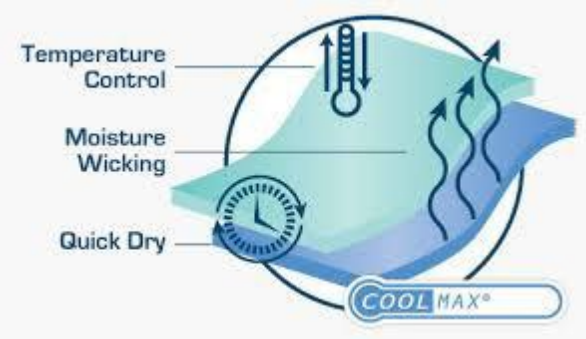

Figure 4. Coolmax Fiber Structure [4]

Sports and leisure (recreation) technical textiles are designed and developed separately for each of the sports fields. This is also tried to be shown in figure 5.

Figure 5. Sports and leisure time (recreation) technical textiles

3. CONCLUSION

During active sports activities, a durable structure is required from the clothes with mechanical stress. However, thermophysiological, functionality and sensory clothing comfort come to the fore. During recreational activities, more clothing comfort and ergonomics are seen.

Glass, carbon, aramid and other prepreg materials are used to improve the performance of equipment, especially in racing sports, where fencing, shovels, sticks and other similar materials are used. In order to increase the performance in sportswear and equipment, it is necessary to use prepreg composite materials together with textile products.

It is aimed that this study, which is carried out to increase the performance of sports and leisure time (recreation) technical textiles, will set an example for the studies to be done and pave the way for experimental studies. As a result of this study; It has been tried to focus on the use of sports and leisure time (recreation) technical textiles in technical textiles and their usability with prepreg materials.

REFERENCES

[1] https://www.kompozitsan.com/tr/karbonfiber-spor-aletleri/593-karbon-palet.html

[2] Akalın, M., Mıstık, S. İ., Teknik Tekstiller, Birsen Yayınevi, İstaanbul, 2010.

[3] Gupta, D., Functional clothing – Definition and classification. Indian Journal of Fibre & Textile Research, 36: 321-326, 2011.

[4] (www.dupont.com)

[5] Akçalı, K., Spor Tekstilleri Üretiminde Kullanılan Farklı Kumaş Yapılarının İncelenmesi, International Journal of Science Culture and Sport December 2016: 4 (Special Issue 3) ISSN: 2148-1148 Doi: 10.14486/IntJSCS632.

2nd International Natural Science, Engineering and Material Technologies Conference
Sep 15-17, 2022, İğneada-Kırklareli / TÜRKİYE

SYNTHESIS OF PINCER-TYPE CARBENES AND THEIR SILVER(I) COMPLEXES WITH CYCLOPHANE STRUCTURE, ELUCIDATION OF THEIR STRUCTURES, AND ANTIMICROBIAL AGENT PROPERTIES

M. Dönmez[1], M. Türkyılmaz[2]

[1] *Department of Chemistry, Faculty of Sciences, Trakya University, Edirne, TÜRKİYE*

E-mail: muratdonmezx@gmail.com

Abstract

This study, it is aimed to synthesize new types of smart drugs with anticancer and antimicrobial properties. For this purpose, a four-stage reaction system was applied. In the first stage; Starting with 2,6-bis(chloromethyl)pyridine (**a**) and 5,6-dimethyl-1H-benzo[*d*]imidazole (**b**), 2,6-bis((5,6-dimethyl-1H-benzo[*d*]imidazol-1-yl)methyl)pyridine (**c**) cyclophane compound forming the main framework was synthesized. In the second stage; a 2-bromoacetonitrile compound was added to the cyclophane compound and a symmetrical N-Heterocyclic compound was synthesized. In the third stage; As a result of the interaction of the carbene compound synthesized in the second step with the silver oxide compound, the silver(I) complex was synthesized. Chemical structures of all synthesized products; are identified by different spectroscopic methods. In the fourth stage; The synthesized compounds were tested against bacterial strains such as gram-positive and gram-negative as well as fungal strains. After examining the antimicrobial activations of carbene and silver complexes, it was determined that the activity of the silver(I)-NHC complex was higher than carbenes.

Keywords: Carbene, silver, cyclophane, antimicrobial agent.

1. INTRODUCTION

N-heterocyclic carbenes (NHC), which are used in modern medicine and material sciences, were proved to have a wide range of use, especially in catalytic practices thanks to their strong σ-donor and weak π-acceptor features [1]. In this area used, cylcophanes, which are strong σ-donor named are new compounds in recent years. Cyclophanes are organic molecules consisting of aromatic compounds besides aliphatic compounds [2]. The aromatic structure rings assist the hardness of their construction, while the aliphatic units compose bridges between the aromatic structures and reason for the elasticity of the whole structure [3]. The synthesis of cyclophane compounds has been on the rise of interest recently (Figure 1) [4].

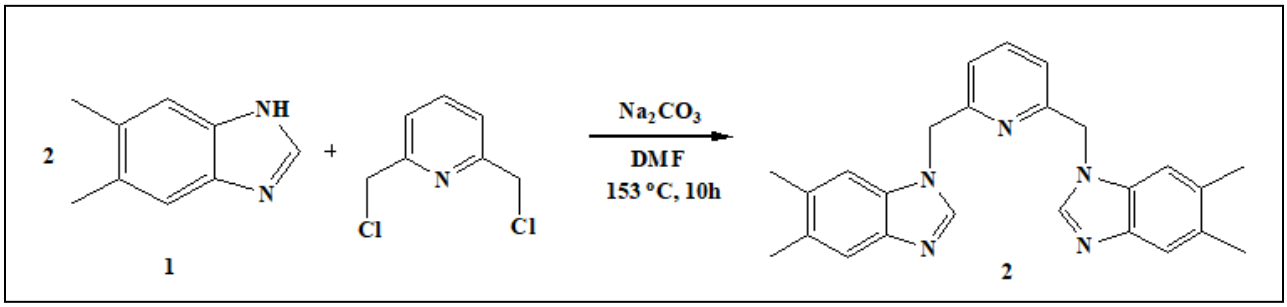

Figure 1. Synthesis methods of carbene compounds.

This interest is supported by the utility of cyclophanes to action as molecular identification reagents in householder-guest chemical systems [5]. The clear construction and high strain of cyclophanes are contributed to a great of practices such as the pharmaceuticals sector [6], asymmetric catalysis [7], insulating plastics [8], organic electronics, metal seize, and supramolecular chemistry [9]. Until now, several methods be indicated for the synthesis of cyclophanes [10]. In some procedures are wanted several steps or hard reaction cases such as high-press, and hard division methods. Recently, silver (Ag(I)) complexes have been used as carbene transfer tasks [11]. Some of the Ag(I)-NHC complexes indicated include monodentate carbenes as ligands, but lots of donor multidentate carbene ligands were interested more attention. Here, it was presented the silver complexes $Ag[PF_6]_2$ reproduced from the 5,6-dimethyl-1H-benzo[*d*]imidazole-linked cyclophanes [12]. In the rigid status, $[NHC][PF_6]_2$ has a dimeric construction with the formula $[Ag_2(NHC)_2][PF_6]_2$, where NHCs show deprotonated compounds. The complexes, which have catalytic activity in water has an important field of research, and thus they are used in a different field. Ag(I)-NHC complexes that include Ag^+ ion have the potential for use in chemotherapy supplied they have enough stability in vivo. In the cyclophane compound

attached to 5,6-dimethylbenzimidazole, it has been reported that silver clusters can remain stable. Antimicrobial efficacies of these complexes were measurements opposite different types of bacteria, and fungi. It was indicated that these novel carbenes and their NHC complexes are efficient antimicrobial agents opposite dissimilar microorganisms. Double cationic cyclophane compound of 5,6-dimethyl-1H-benzo[*d*]imidazolium-linked; such as 3-bromopropanenitrile obtained as a result of reaction with substituents. cyclophane derivatives with properties varied in terms of yield, solubility, and antimicrobial activation [13].

2. MATERIAL AND METHODS

Names of chemicals used in reactions carried out under argon gas; 2,6-bis(chloromethyl) pyridine; ($C_7H_7Cl_2N \geq 99.00$ %), 5,6-dimethyl-1H-benzo[*d*]imidazole ($C_9H_{10}N_2 \geq 99.00$ %), 2-bromoacetonitrile; ($C_2H_2BrN, \geq 97.00$ %), diethyl ether; ($C_4H_{10}O \geq 99.9$ %), deuterated chloroform; ($CDCl_3 \geq 99.80$ %), deuterium oxide; ($D_2O \geq 99.95$ %), ethanol; ($C_2H_5OH \geq 99.90$ %), sodium carbonate; ($Na_2CO_3 \geq 99.50$ %), silver(I) oxide; ($Ag_2O \geq 99.0$ %), ethyl acetate; ($C_4H_8O_2 \geq 99.50$ %), hexane; ($C_6H_{14} \geq 99.00$ %), potassium hexafluorophosphate; ($KPF_6 \geq 99.50$ %). Used in chemical reactions names of devices; Thermo Scientific Nicolet İN10 brand Pye Unicam, Shimadzu UV 1600 spectrophotometer, Thermogravimetric analysis TGA 400, A vacuum oven, X-Ray diffraction (XRD) analysis Elemental analysis a Sundy SDCHN636 Carbon Hydrogen & Nitrogen Analyzer, Melting points an Electrothermal-9200 melting point apparatus FT-IR spectrum an ATI Unicam 1000 spectrometer, Multi-Analyzer-MRC Lab: pH, Conductivity, Do, Temp & More,

3. RESULTS AND DISCUSSION

3.1. Synthesis Methods of NHC Carbenes

In this article, 5,6-dimethyl-1H-benzo[*d*]imidazole (**1**) and 2,6-bis(chloromethyl)pyridine (**2**) were interacted to obtain the main skeleton 2,6-bis((5,6-dimethyl-1H-benzo[*d*]imidazol-1-yl)methyl)pyridine (**3**). After the structure of this obtained compound was elucidated, it was interacted with the 2-bromoacetonitrile compound to obtain the carbene compound 1,1'-(pyridine-2,6-diyl bis(methylene))bis(3-(cyanomethyl)-5,6-dimethyl-1*H*-3λ^4-benzo[*d*]imidazol-1-ium)bromide (**4**) carbene derived. The conductivity value of the carbene compound was characterized by spectroscopic methods such as ^{1}H-NMR, ^{13}C-NMR, FT-IR, TGA analysis, melting point, and XRD spectroscopy (Figure 2).

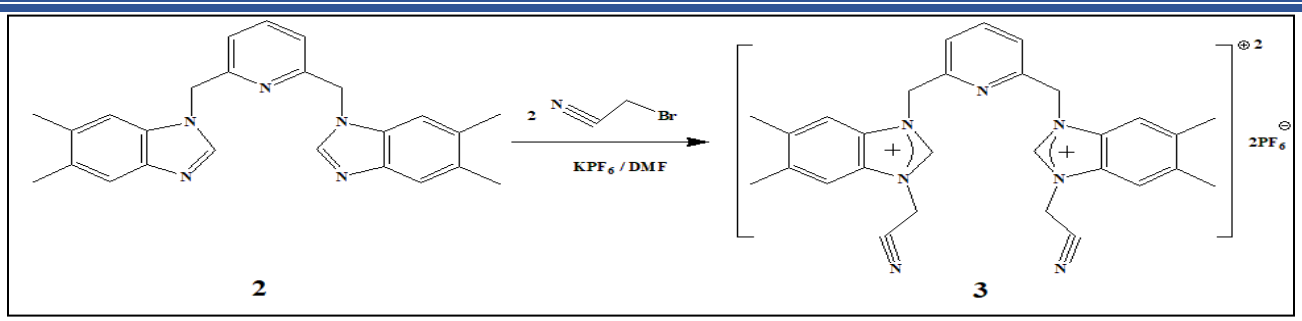

Figure 2. Synthesis methods of carbenes.

5,6-dimethyl-1H-benzo[*d*]imidazole (0.321 g, 2.2 mmol), 2,6-bis(chloromethyl)pyridine (0.176 g, 1 mmol), Na_2CO_3 (0.11 g, 1 mmol) and DMF (20 ml) are added at room temperature under nitrogen gas. Product **3b** was obtained by a method similar to product **3a.** Conductivity value (µS / cm, 10^{-3} M, in water): 10.80. Yield: %32 (0.178 g). Melting point: 322-324 ºC. Brown solid. UV-vis (CH_3CN) 292 (4.65), 297 (4.68), 345 (4.89) and 368 (4.90) nm'de $\pi \rightarrow \pi^*$ transition. Molecular formula: $C_{29}H_{29}F_{12}N_7P_2$, LC-Mass Spectrum: 477.2280 $[M]^+$.

3.1.1. FT-IR Analysis of Carbene

When the FT-IR spectrum of the synthesized compounds is examined; -C-H stress peaks in CH_3 and CH_2 groups are also observed, the sharp peaks of the stress, and the -C-H stretch of the aromatic compound ring in the structure as a flat peak (Figure 3).

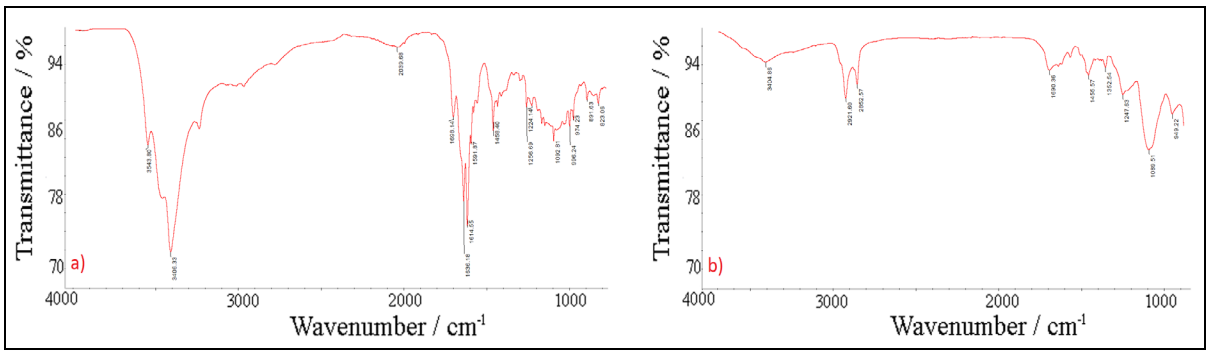

Figure 3. FTIR spectrums compounds of **a)** 3 and **b)** 4.

3.1.2. NMR Analysis of Carbene

NMR analysis of the starting material showed that the carbon peak in ^{1}H-NMR was in the range of 8-9 ppm, and the carbon peak in ^{13}C-NMR was in around of 130-140 ppm. It gives sharp methyl (CH3) peaks at

3-4 ppm depending on the vibration of the methyl bond in the 5,6-dimethylbenzimidazolium in the structure of cyclophanes. NMR analysis of carbenes gives sharp peaks in the range of 8-9 ppm depending on the acidic proton in the NMR of hydrogen, in and the range of 140-150 ppm in the NMR of carbon (Figure 4,5,6).

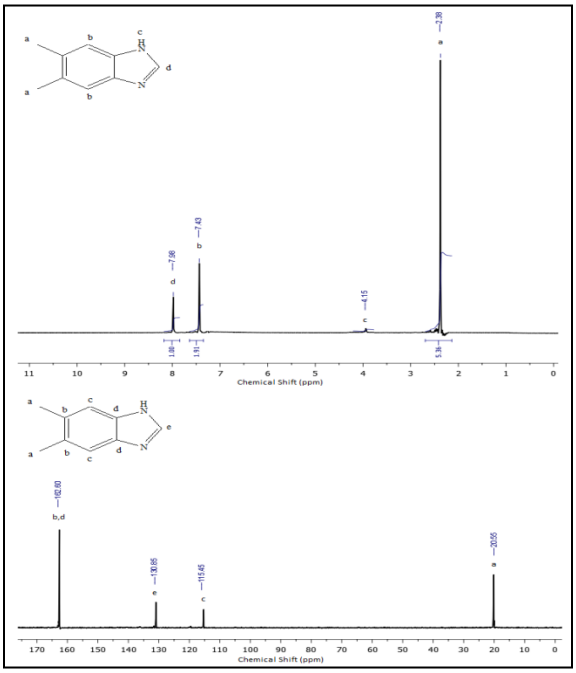

Figure 4. ^{1}H and ^{13}C-NMR spectrums compounds of **1** and **2.**

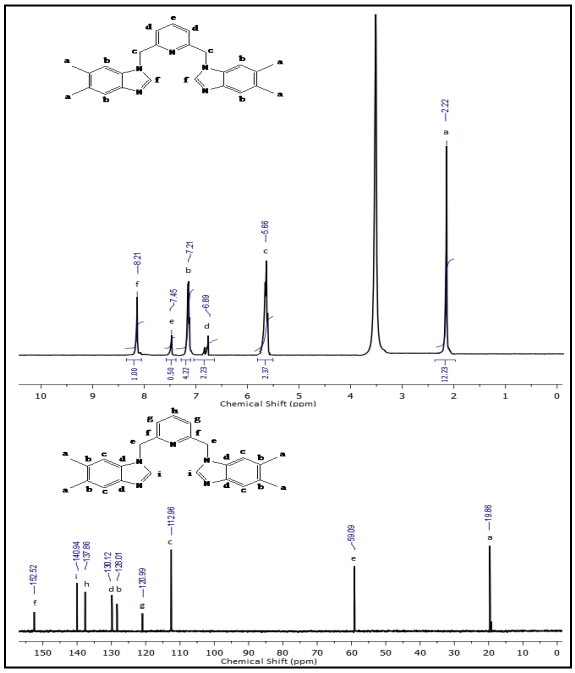

Figure 5. ^{1}H and ^{13}C-NMR spectrums compounds of **2.**

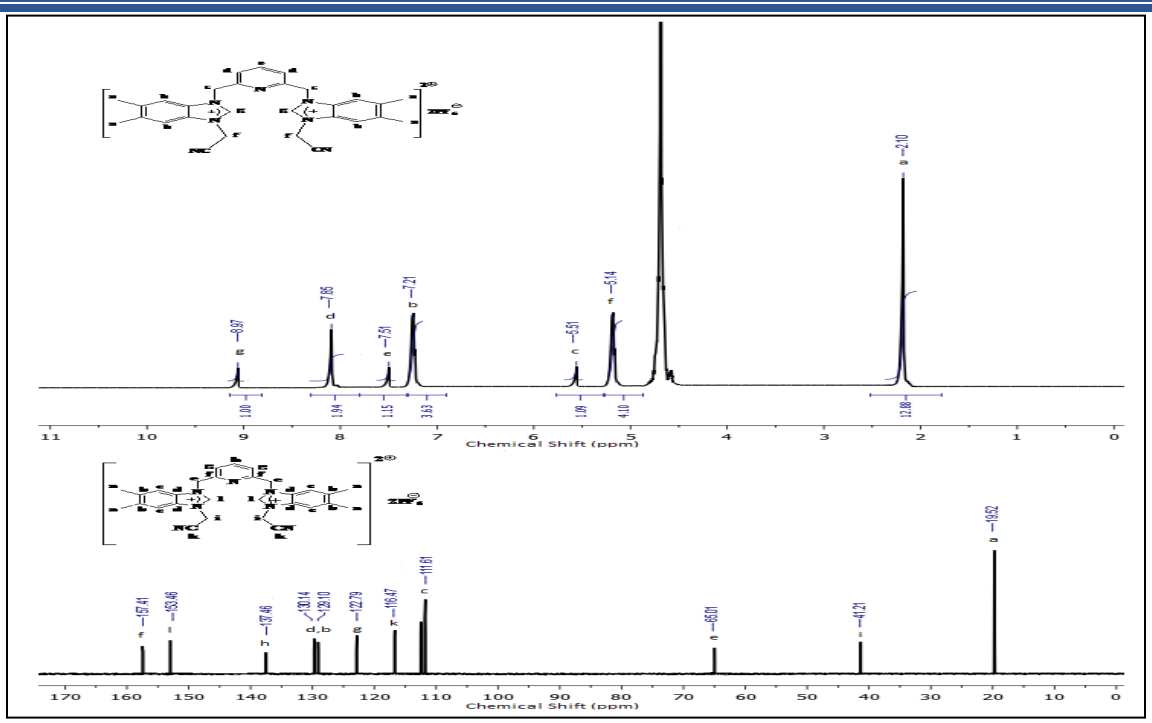

Figure 6. ^{1}H and ^{13}C-NMR spectrums compounds of **3.**

3.1.2. XRD Analysis of Carbene

The chemical structure of the catalyst has supported by the XRD method. The powder XRD pattern of the of NHCs looked gives data involved with organic structure. In this designed organic structure, it has been the nitrogen, hydrogen, and carbon in the centric component and hexafluorophosphate ion for the stable compound. The XRD peaks at 10.47, 25.17, and 50.87 are due to (180), (370), and (580) reflection planes of the PF_6^-. The large halo around 8-28º can be because of the form of NHC and organic ligands in the construction. To literature information, it could be because of the nano-construction creation of NHCs. The large halogen around 8-28° may be due to the NHC and organic parts in the structure. It may also be from the nanostructured part of NHCs as in the cited literature (Figure 7).

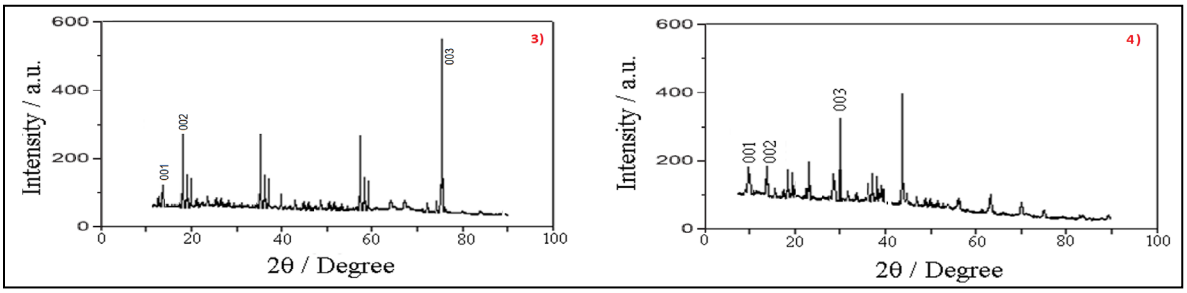

Figure 7. XRD measurements compounds of **a)** 3 and **b)** 4.

3.2. Synthesis Methods of Ag(I)-NHC Complexes

1,1'-(pyridine-2,6-diylbis(methylene))bis(3-(cyanomethyl)-5,6-dimethyl-1*H*-3λ^4-benzo[*d*]imidazol-1-ium)bromide **4** (0.555 g, 1 mmol), KPF_6 (0.367 g, 2 mmol), Ag_2O (0.14 g, 0.60 mmol) and DMF (20 mL) were backwashed at 78 °C for 10 h. After the solution was filtered over celite, the organic solvent was removed in a vacuum oven. The conductivity value of the carbene compound was characterized by spectroscopic methods such as ^{1}H-NMR, ^{13}C-NMR, FT-IR, TGA analysis, melting point, and XRD spectroscopy (Figure 8).

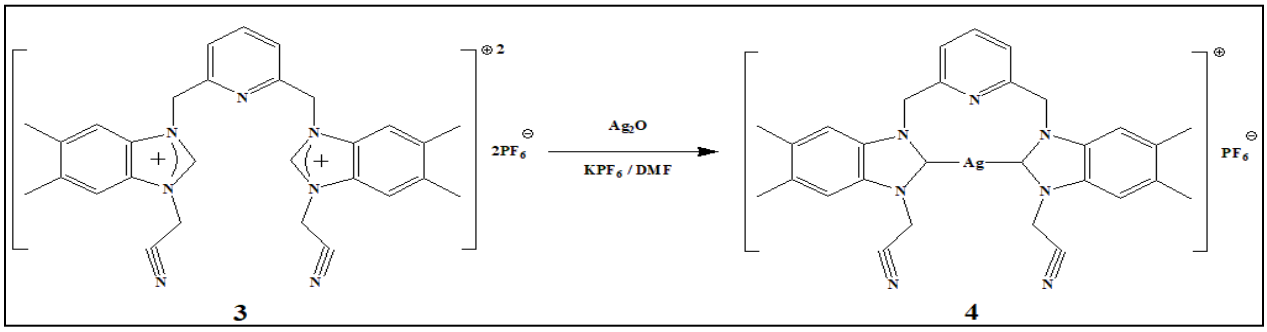

Figure 8. Synthesis methods of Ag(I)-NHC complexes.

Yellow solid. Yield: 0.218 g, 30 %. Melting point. 271-273 °C. Conductivity value (µS/cm, in water): 68.16. % Elemental analysis; calcd: C: 47.82, H: 4.01, N: 13.46, found: C: 47.85, H: 4.06, N: 13.41. IR (revel / abs, 4000-450 cm^{-1}), ν (OH) 3404 (s), 2921 (s), 2852 (s), 1690 (d), 1455 (d), 1352 (s), 1247 (s), 1089 (s), 834 (s). UV/VIS (CH_3CN); π → π * transition at 259 (4.46) nm, at 586 (4.99) and 642 (4.88) nm LCMT **n → π*** transition. Molecular formula: $C_{29}H_{29}AgF_6N_7P$, LC-Mass Spektrumu: 582.1129 $[M]^+$.

3.2.2. NMR Analysis of Metal Complexes

In the NMR analysis of metal complexes obtained from carbenes, it is observed that the carbene peak point in hydrogen NMR does not signal at ^{1}H-NMR, while in ^{13}C-NMR it signals at 160-180 ppm depending on the Ag-Carbene bond (Figure 9).

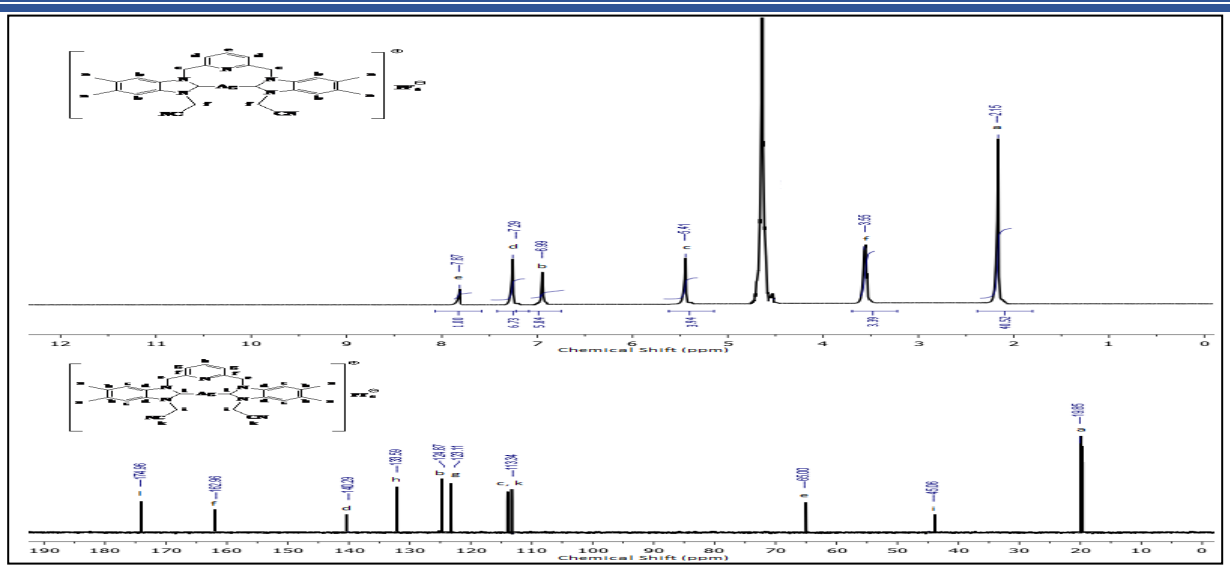

Figure 9. ^{1}H and ^{13}C NMR spectrums of Ag(I)-NHC Complexes

3.2.1. TGA-DTA Analysis of Metal Complexes

Thermal gravimetric analysis measurements of metal complexes and weight loss of compounds have been curred in four steps. In the first step, the temperature was between 101 and 399 °C. The weight loss came from dehydration of components. In this step for water molecule lost is generwholey between 1-2 moles. In the second step, the temperature was between 400 and 799 °C, which is due to primary carbonization. In the third step, the temperature was between 510 and 795 °C and the compound was nearly completely carbonized. There was higher weight loss at 800 °C due to major volatiles and tar elimination (Figure 10).

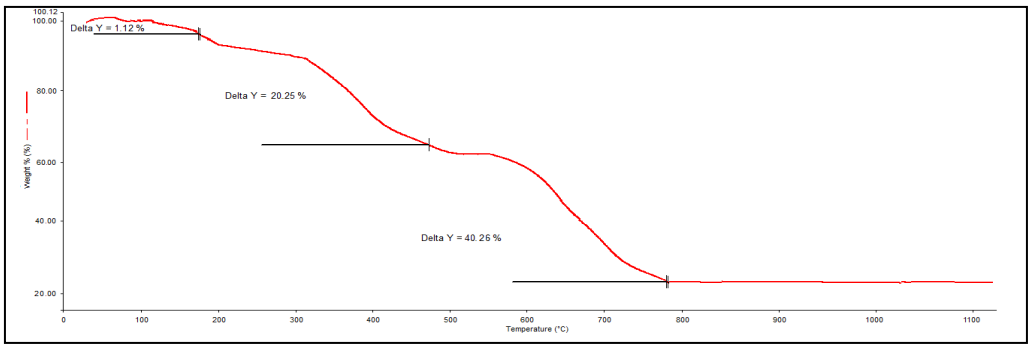

Figure 10. TGA analysis of compound **4.**

3.3. Antimicrobial Activities Synthesized Compounds

After a series of novel pincer-type structures the cyclophane cation had synthesized, and their Ag(I)-NHC complexes were synthesized. Antimicrobial efficiencies of such new complexes were reported. In

carbene compound **3**, in Ag(I)-NHC complex **4**, showed better antimicrobial efficiency against bacteria and fungi compared to other complex concentrations. Results study are beneficial for the synthesis of NHC derivative compounds with high antimicrobial efficiency (Figure 11) [14].

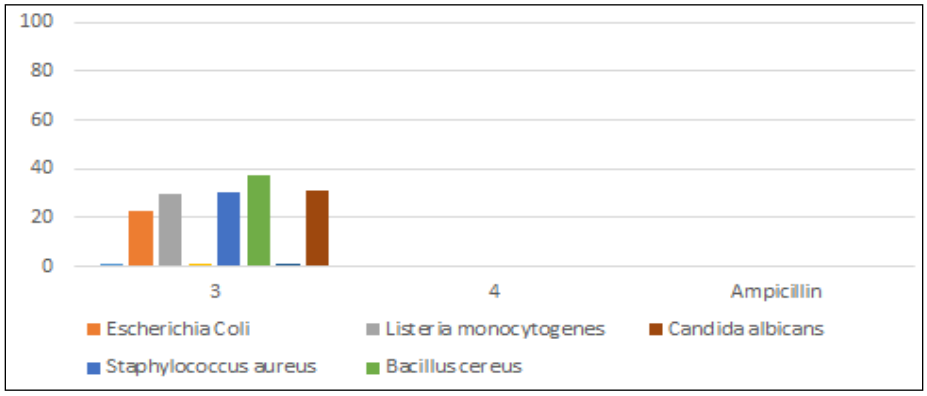

Figure 11. Graphical representation of the MIC values of Compounds **3** and **4**.

4. CONCLUSION

After a series of novel pincer-type symmetrical structures the cyclophane cation had synthesized, and their Ag(I)-NHC complexes were synthesized. These compounds were identified by using spectroscopic and analytical methods. Antimicrobial efficiencies of such new complexes were reported. In carbenes **4a**, Ag(I)-NHC complexes **5d**, showed better antimicrobial efficiency against bacteria and fungi compared to other complexes' lower concentrations. The results of the study are beneficial for the synthesis of NHC derivative compounds with high antimicrobial efficiency. In FT-IR spectra analysis, the hydroxyl in the alcohol group bond at 3404 cm1, the nitrile (-C=N:) bond at 1600-1650 cm^{-1}, the carbonyl bond (-C=O) in the acetate group at 1626 cm^{-1}, and the amine group ($-NH_2$) at 3393 cm^{-1} of the functional groups. In NMR analysis, peaks of cyclophanes carbenes, which 5,6-dimethylbenzimidazolium compound attached give a peak of 8-10 ppm at the ^{1}H NMR and over 140-160 ppm at the ^{13}C-NMR. In metal complexes obtained from carbenes, it is observed that the carbene peaks do not signal at ^{1}H-NMR, the Ag-Carbene bond is formed signaling at 190 ppm at ^{13}C-NMR. However, the metal ion effect in the mass spectrum both confirms the 1:1 or 2:1 coordination ratio of the ligand and Ag^{+} ion and shows the isotopic patterns reflecting the silver atom. In TGA analysis, in the first step; moisture or water loss in the environment, in the second and third steps; In the fourth step where the organic part of the main skeleton burned away; it was observed that silver metal remained in the environment.

In the data analysis based on the total % mass loss, it was determined that the calculated values of silver metal differ from the theoretical values.

ACKNOWLEDGMENTS

This study was supported by the Scientific Project Unit of Trakya University under project number: TUBAP-2014-106.

REFERENCES

[1] Bellotti, P., Koy, M., Hopkinson, M.N., Glorius, F., Recent advances in the chemistry and applications of N-heterocyclic carbenes, Nat Rev Chem., 5, 711–725, 2021.https://doi.org/10.1038/s41570-021-00321-1.

[2] Gong, W., Zhang, G., Liu, T., Giri, R. Yu, J.-Q., Site-Selective C(sp3) −H Functionalization of Di-, Tri-, and Tetrapeptides at the N-Terminus, J. Am. Chem. Soc., 136, 16940–16946, 2014. https://doi.org/10.1021/ja510233h.

[3] Li, C. Pillararene-based supramolecular polymers: from molecular recognition to polymeric aggregates, Chem. Commun., 50, 12420, 2014. https://doi.org/10.1039/c4cc03170a.

[4] Gulder, T., Baran, P.S., Strained cyclophane natural products: Macrocyclization at its limits, Nat. Prod Rep., 29, 899–934, 2012. https://doi.org/10.1039/C2NP20034A.

[5] Velle, A., Rodriguez-Santiago, L., Sodupe, M., Sanz Miguel, P. J., Enhanced Metallophilicity in Metal–Carbene Systems: Stronger Character of Aurophilic Interactions in Solution, Chemistry–A European Journal. 2019. https://doi.org/10.1002/chem.201904507.

[6] Yamaguchi, J., Yamaguchi, A. D., Itami, K. CH Bond Functionalization: Emerging Synthetic Tools for Natural Products and Pharmaceuticals, Angew. Chem. Int. Ed., 51, 8960–9009, 2012. https://doi.org/10.1002/anie.201201666.

[7] Peng, B., Ma, J., Guo, J., Gong, Y., Zhang, R.W.Y., Zeng, J., Chen, W.-W., Ding, K., Zhao, B., J. Am. Chem. Soc., A Powerful Chiral Super Brønsted C–H Acid for Asymmetric Catalysis, 144, 2853–2860, 2022. https://doi.org/10.1021/jacs.1c12723.

[8] Read, D., Assaad, Structural properties of fiber-reinforced concrete containing thermosetting polymer plastic wastes J.J, 11, 137-147, 2022, https://doi.org/10.1080/21650373.2021.1899998.

[9] Chu, D., Gong, W., Jiang, H., Tang, X., Cui, Y., Liu, Y., Boosting Enantioselectivity of Chiral Molecular Catalysts with Supramolecular Metal–Organic Cages, Chinese Chemical Society Publishing, 4, 1180-1189, 2022. https://doi.org/10.31635/ccschem.021.202100847.

[10] Vida, Y., Perez-Inestrosa, Cyclophane size drives the photochemical behaviour of benzophenone, E. Photochem Photobiol Sci., 11, 1645-1651, 2012,. https://doi.org/10.1039/c2pp25025j.

[11] Chen, Z.-L., Empel, C., Wang, K., Wu, P.-P., Cai, B.-G., Li, L., Koenigs, R.M. Xuan, Enabling Cyclopropanation Reactions of Imidazole Heterocycles via Chemoselective Photochemical Carbene Transfer Reactions of NHC-Boranes, J., J. Org Lett., 24, 2232–2237, 2022. https://doi.org/10.1021/acs.orglett.2c00609.

[12] Hamdi, N., Mnasri, A., Nasr, I.S.A.; Koko, W.S., Khan, T. A., Biersack, B., Özdemir, I., Gürbüz, N., *Polycyclic Aromatic Compounds* Highly Efficient Single A3-Coupling (Aldehyde-Amine-Alkyne) Reaction Catalyzed by Air Stable Silver-(N-Heterocyclic Carbene) Complexes: Synthesis and Characterization, 2022. https://doi.org/10.1080/10406638.2021.2019064.

[13] Turkyilmaz, M., Uluçam, G., Aktaş, Ş., Okan, S. E., Synthesis and characterization of new N-heterocyclic carbene ligands: 1,3-Bis(acetamide)imidazol-3-ium bromide and 3-(acetamide)-1-(3-aminopropyl)-1H-imidazol-3-ium bromide, Journal of Molecular Structure 1136, 263-270, 2017. https://doi.org/10.1016/j.molstruc.2017.02.022.

[14] Tran, T.N.T., Nguyen, T.D.P., Dinh, H.T., Bui, T.T., Ho, L.H., Nguyen-Phan, T.X., Khoo, K.S., Chew, K.W., Show, P.L., Characterization of bacteria type strain *Bacillus*. spp isolated from extracellular polymeric substance harvested in seafood wastewater Journal of Chemical Technology & Biotecnology, 97, 501-508, 2021. https://doi.org/10.1002/jctb.6870.

2nd International Natural Science, Engineering and Material Technologies Conference
Sep 15-17, 2022, İğneada-Kırklareli / TÜRKİYE

THE EFFECT OF USING VARIOUS CONSTRUCTION MATERIALS ON VIBRATION ISOLATION FREQUENCY BAND OF A PERIODIC STRUCTURE

E. Er[1], E. Türkeş[1], O. Yüksel[1]

[1]*Department of Mechanical Engineering, Faculty of Engineering, Kırklareli University, Kırklareli, TÜRKİYE*

E-mail: osmanyuksel@klu.edu.tr

Abstract

Traditionally, passive vibration isolation is achieved by using mass-spring type structures. However, as an innovative approach, periodic structures can also be utilized as vibration isolators, as well. This special kind of periodic structures are called phononic band gap structures or elastic metamaterials. These periodic structures can be designed via Bragg Scattering, Local Resonances or Inertial Amplification [1, 2] methods.
In this paper, inertial amplification induced vibration isolation frequency band properties of various periodic structures formed by using different construction materials, are studied. At first, a compliant inertial amplification mechanism is presented. Then, by incorporating three of these mechanisms in a linear sequence, a one-dimensional periodic structure is formed. Finally, by alternating the construction materials of flexure hinge connections and rigid body blocks of the periodic structure, vibration isolation frequency band properties (i.e., band width and band depth) are analyzed, compared with each other and discussed via displacement transmissibility (i.e., frequency response function) plots.

Keywords: periodic structure, vibration isolator, inertial amplification, compliant mechanism

1. INTRODUCTION

Vibration isolation is defined as reducing vibration transmission from the source to the target structure. Traditionally this goal is achieved via employing mass and spring type structures. On the other hand, as an innovative approach periodic structures can be utilized as passive vibration isolators, as well. Periodic vibration isolators can be designed with one of the three methods which are called inertial amplification [1, 2], Bragg scattering [3, 4] and local resonances [5, 6].

In Bragg scattering method, periodically varying mass and stiffness values are used throughout the structure. In local resonances method, periodic local resonators are added to the structure. In inertial amplification method, periodic inertial amplifier mechanisms provide vibration isolation. Inertial amplification has an advantage over local resonances and Bragg scattering methods, since by employing inertial amplification method, low frequency vibration isolation can be achieved without increasing total mass and sacrificing total stiffness of the structure. Periodic structures designed with embedded compliant inertial amplification mechanisms can be utilized as efficient vibration isolators operating in the low frequency region [2, 7].

In periodic vibration isolators, the smallest repeating mechanism is called as the unit cell. The unit cell determines the vibration isolation frequency band of the periodic structure [1, 2, 7, 8]. Moreover, as the number of unit cells used in the periodic structure increases then the achieved vibration isolation levels increase, as well [1, 2, 7, 8]. Therefore, design of unit cell mechanisms is crucial for the vibration isolation performance of periodic structures.

In this study, the effect of using various construction materials on vibration isolation frequency band of a periodic structure is discussed. The periodic structure considered is formed via incorporating compliant inertial amplification mechanisms in a linear sequence. Then by altering the flexure hinge connections and large building blocks of the periodic structure, changes in the vibration isolation frequency band width and band depth are analysed and discussed.

2. MATERIAL AND METHODS

The lumped parameter inertial amplification mechanism is provided in Figure 1. Here, y denotes the input displacement, x denotes the output displacement. The two m masses at the right and left end of the

mechanism are connected with a spring with stiffness k. Whereas, the amplifier mass m_a at the top of the mechanism is connected to the masses m with rigid rods. The acute angle between the rigid rods and the spring is θ. The equation of motion of this lumped parameter system is provided as:

$$(m_a(cot^2\theta + 1)/4 + m)\ddot{x} + kx = (m_a(cot^2\theta - 1)/4)\ddot{y} + ky \quad (1)$$

When Equation 1 is solved for the output, the first resonance frequency is obtained as:

$$\omega_1 = \sqrt{\frac{k}{m+m_a(cot^2\theta+1)/4}} \quad (2)$$

When Equation 1 is solved for the input, the first antiresonance frequency is obtained as:

$$\omega_{z1} = \sqrt{\frac{k}{m_a(cot^2\theta-1)/4}} \quad (3)$$

For small θ values, dynamic inertia of the lumped parameter mechanism is amplified. Thence, the vibration isolation frequency band starting frequency shifts to the low frequency region and can be defined as [2, 7, 8]:

$$\omega_s = \sqrt{\frac{2{\omega_1}^2{\omega_{z1}}^2}{{\omega_1}^2+{\omega_{z1}}^2}} \quad (4)$$

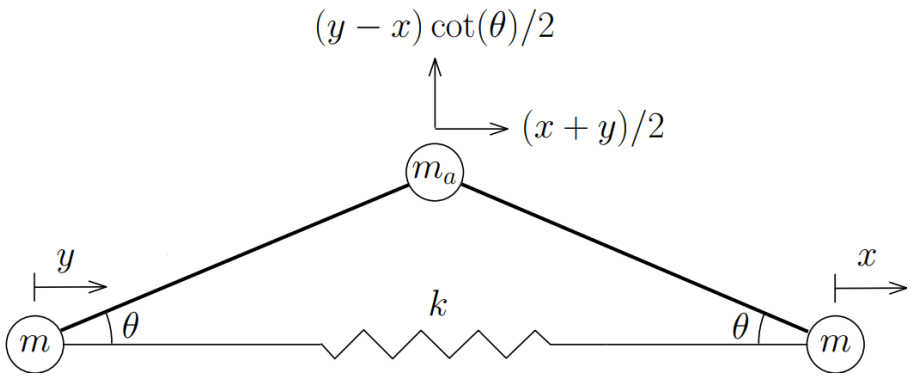

Figure 1. The lumped parameter inertial amplification mechanism model.

On the other, the compliant inertial amplification mechanism discussed in this study is provided in Figure 2. It is a two-dimensional mechanism that consists of three sections which are enumerated as 1, 2 and 3. Section 1 is the first large block which has 25 mm horizontal and 50 mm vertical dimensions. Section 2 is the flexure hinge connection which has a length of 100 mm and 5 mm vertical thickness. The acute angle between the flexure hinge and horizontal axis is selected as 15°. Section 3 is the other large block which has 50 mm horizontal and 50 mm vertical dimensions. The compliant inertial amplification mechanism is the unit cell of the periodic structure.

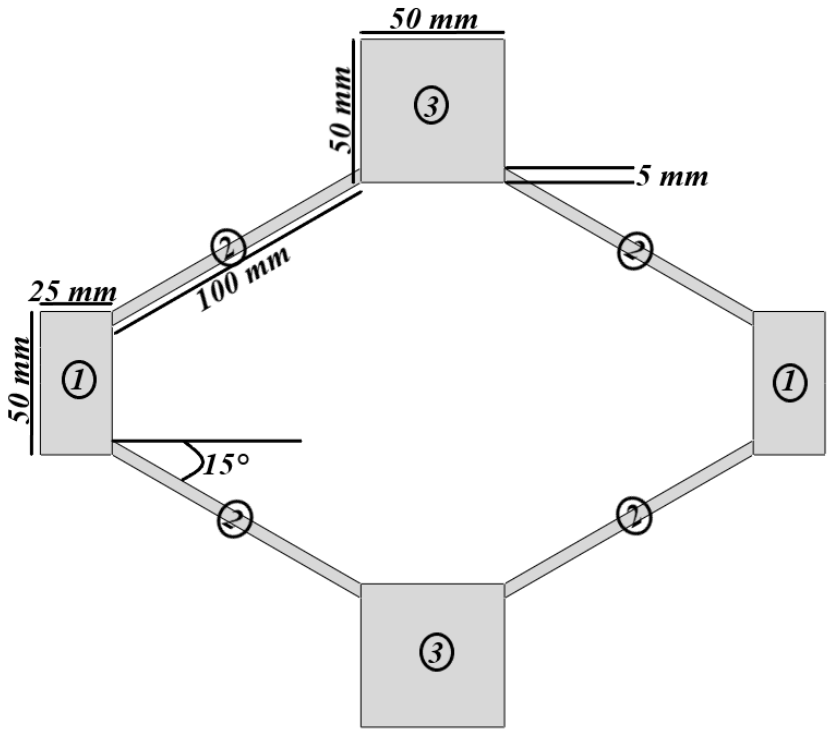

Figure 2. The dimensions and the configuration of the compliant inertial amplification mechanism, which is used as the unit cell (i.e., the repetitive building block) of the periodic structure.

The unit cell determines the starting and ending frequencies of the vibration isolation frequency band of the periodic structure. In this study, dimensions of the unit cell are fixed. Whereas, the construction materials of the large blocks and flexure hinges are altered. Since the dimensions of the unit cell do not change, hence the starting and ending mode shapes of the vibration isolation frequency band do not change, as well. In Figures 3 and 4, vibration isolation frequency band starting (Figure 3) and ending (Figure 4) mode shapes are provided,

respectively. As can be seen, in both modes, large blocks enumerated as 1 and 3 perform rigid body motion while, flexure hinge connections enumerated as 2 flex and bend. Therefore, it can be said that the construction material of the flexure hinges determines the vibration isolation frequency band width (i.e., the frequency band range).

The construction materials are selected as steel and copper. Steel material properties are given as: modulus of elasticity, $E = 210$ GPa; density, $\rho = 7800$ kg/m^3, Poisson's ratio, $v = 0.3$. On the other hand, copper material properties are provided as: modulus of elasticity, $E = 130$ GPa; density, $\rho = 8960$ kg/m^3, Poisson's ratio, $v = 0.34$.

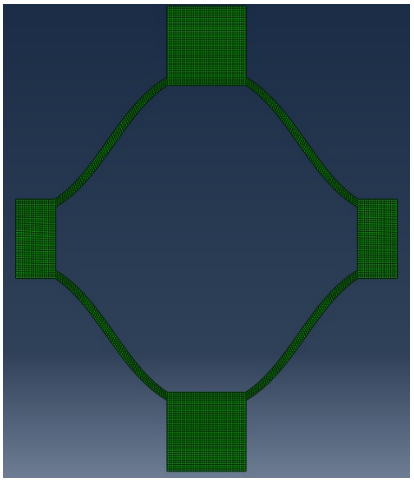

Figure 3. The opening mode of the compliant unit cell mechanism that determines the vibration isolation frequency band starting frequency.

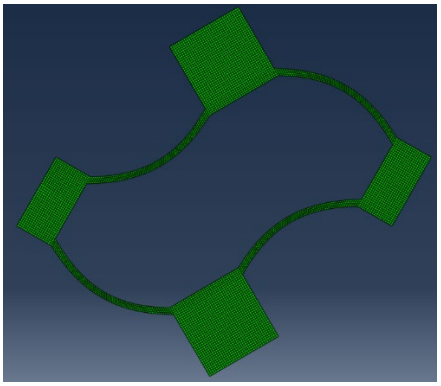

Figure 4. The bending mode of the compliant unit cell mechanism that determines the vibration isolation frequency band ending frequency.

By incorporating three of the unit cell mechanisms in a linear sequence, a one-dimensional periodic structure shown in Figure 5 is formed. Here, horizontal input displacement is provided at the left end and the output displacement is taken from the other end. Displacement transmissibilities (frequency response function) of the constructed periodic structures are calculated with the Equation 5:

$$TR(\omega) = \frac{|output|}{|input|} = \frac{|x|}{|y|} \tag{5}$$

In the study, four periodic structures are formed by altering the construction materials of the sections enumerated as 1, 2 and 3.

- Periodic Structure 1's construction material is steel
- Periodic Structure 2's construction material is copper
- Periodic Structure 3's 1st and 3rd blocks are steel whereas flexure hinges (i.e., 2nd beams) are copper
- Periodic Structure 4's 1st and 3rd blocks are copper whereas flexure hinges (i.e., 2nd beams) are steel

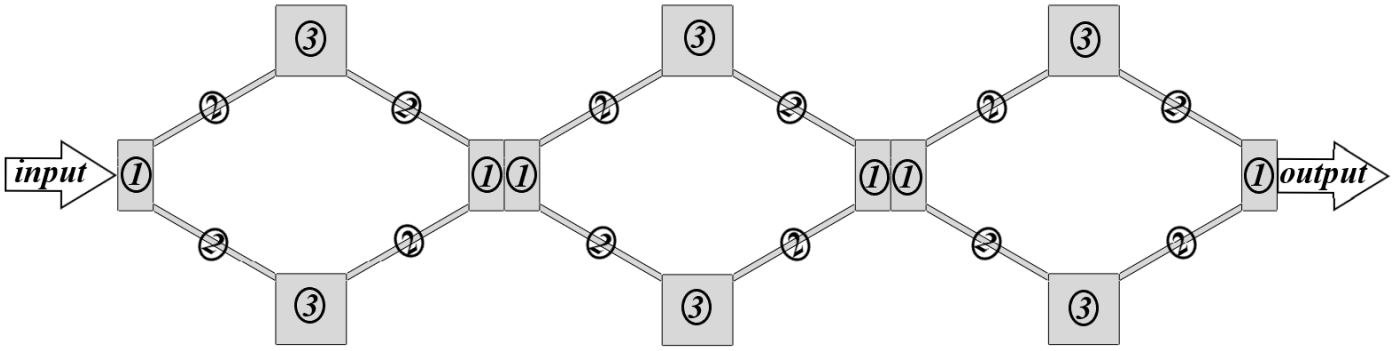

Figure 5. The one-dimensional periodic vibration isolator structure constructed via successive incorporation of three unit cell mechanisms. Here, displacement (i.e., vibration) input is provided from the left end and output displacement (i.e., vibration) is calculated from the other end for low frequency region.

3. RESULTS AND DISCUSSION

The displacement transmissibility values for the four different periodic structures are calculated using Equation 5 and the plots are provided in Figures 6-9. In Figure 6, the displacement transmissibility plot of the periodic structure 1 formed with steel blocks (enumerated as 1 and 3) and steel flexure hinges (enumerated as 2) is seen. The vibration isolation frequency band for this periodic structure is between 211 Hz – 352 Hz.

In Figure 7, the displacement transmissibility plot of the periodic structure 2 formed with copper blocks (enumerated as 1 and 3) and copper flexure hinges (enumerated as 2) is provided. The vibration isolation frequency band for this periodic structure occurs between 155 Hz – 259 Hz.

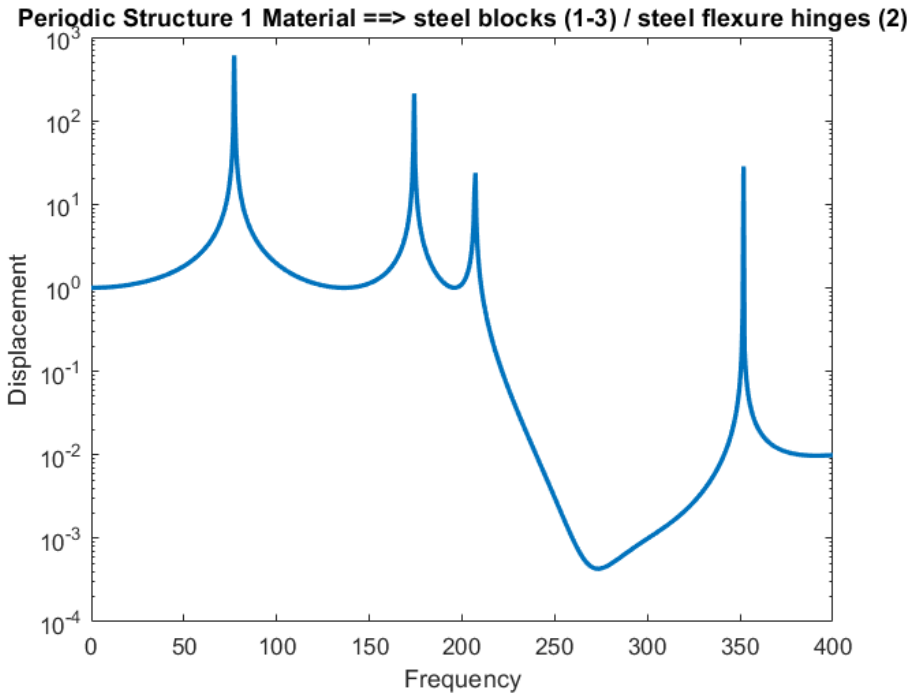

Figure 6. Displacement transmissibility plot of the periodic structure 1 formed with steel blocks (enumerated as 1 and 3) and steel flexure hinges (enumerated as 2). Vibration isolation frequency band is between 211 Hz – 352 Hz.

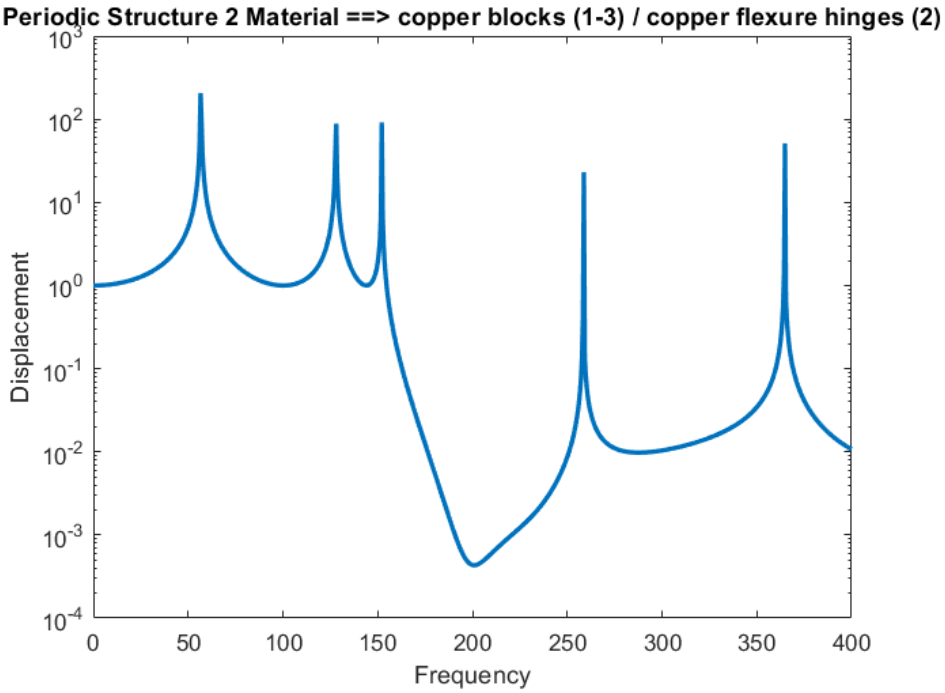

Figure 7. Displacement transmissibility plot of the periodic structure 2 formed with copper blocks (enumerated as 1 and 3) and copper flexure hinges (enumerated as 2). Vibration isolation frequency band is between 155 Hz – 259 Hz.

In Figure 8, the displacement transmissibility plot of the periodic structure 3 formed with steel blocks (enumerated as 1 and 3) and copper flexure hinges (enumerated as 2) is given. The vibration isolation frequency band is formed between 168 Hz – 268 Hz.

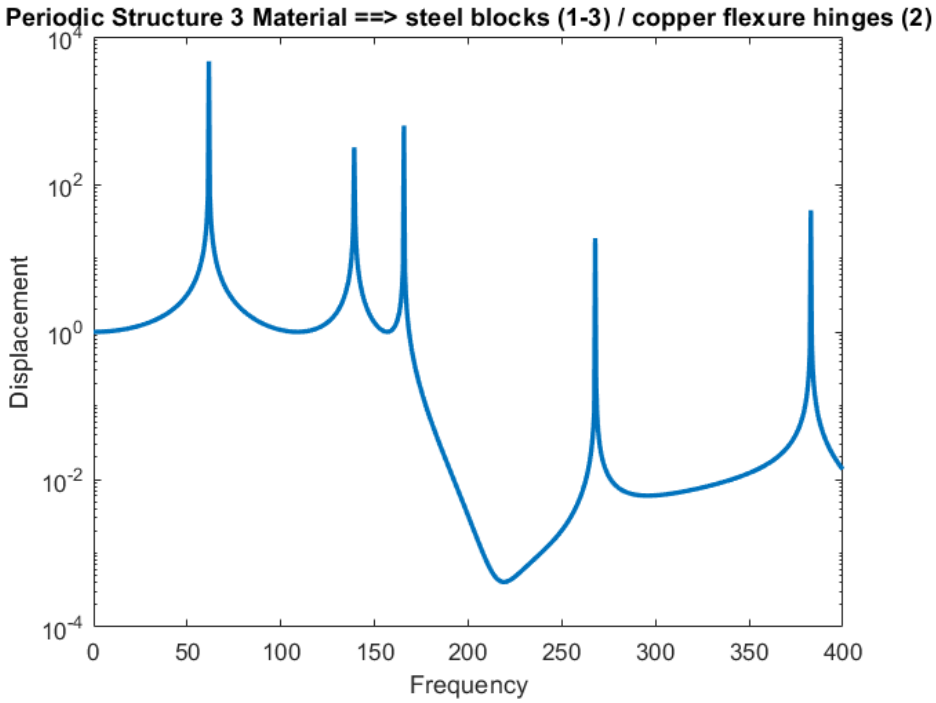

Figure 8. Displacement transmissibility plot of the periodic structure 3 formed with steel blocks (enumerated as 1 and 3) and copper flexure hinges (enumerated as 2). Vibration isolation frequency band is between 168 Hz – 268 Hz.

In Figure 9, the displacement transmissibility plot of the periodic structure 4 formed with copper blocks (enumerated as 1 and 3) and steel flexure hinges (enumerated as 2) is shown. The vibration isolation frequency band appears between 191 Hz – 337 Hz.

When results are analysed, it is seen that the construction material of flexure hinge connections determines the vibration isolation frequency band width. As the "Elastic Modulus / Density" ratio increases then the vibration isolation frequency band range increases, as well. This behaviour is observed since the isolation band starting and ending frequencies are function of bending mode of the flexure hinges as seen in Figures 3 and 4. In other words, structure's stiffness for the corresponding mode is determined by the flexure hinges. Hence, for the periodic structures with steel flexure hinges, widest possible vibration isolation frequency band is achieved.

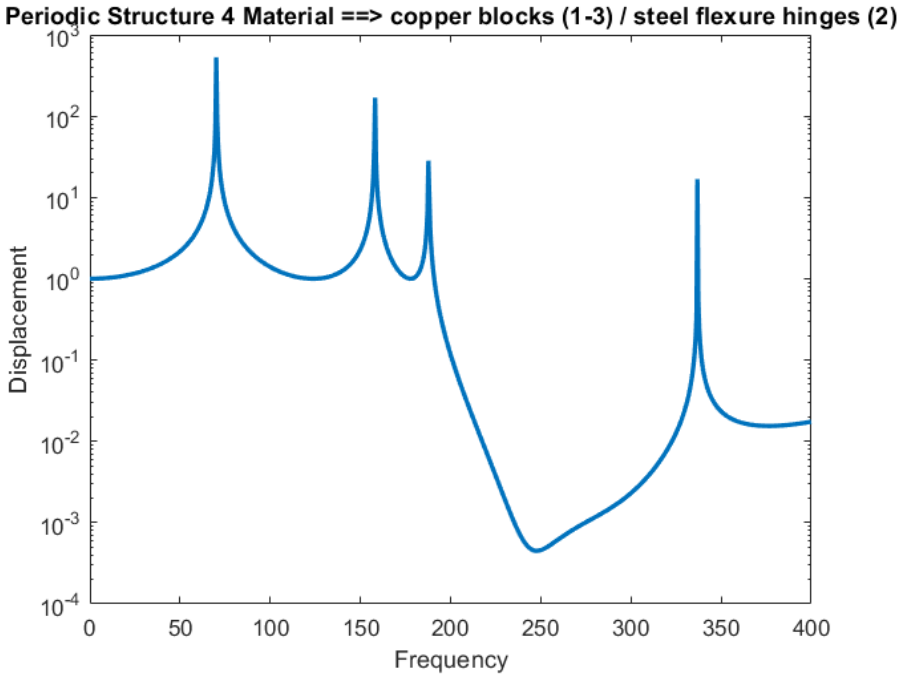

Figure 9. Displacement transmissibility plot of the periodic structure 4 formed with copper blocks (enumerated as 1 and 3) and steel flexure hinges (enumerated as 2). Vibration isolation frequency band is between 191 Hz – 337 Hz.

Besides, the material of construction of large blocks determines the vibration isolation band's starting frequency. As the density of the large blocks' material increases then vibration isolation starts at lower frequencies. It is observed since, periodic structure's total mass is mainly the function of large blocks' masses. As heavier blocks are utilized, total mass of the structure increases thus isolation band starting frequency decreases.

On the other hand, vibration isolation amounts (i.e., isolation band depth) achieved for all of the four periodic structures are quite similar to each other. For all of the structures, satisfactory vibration isolation levels are reached for almost the entire isolation frequency band width. At some frequencies, more than 99.9 % vibration isolation is achieved. In other words, at those frequency values, only 0.1 % of input vibration reaches to the output end.

4. CONCLUSION

All of the periodic structures proposed in this study can be utilized as high-performance vibration isolators operating at low frequency region, since the vibration isolation levels achieved are quite satisfactory

for all of them. However, in order to attain vibration isolation for wider frequency ranges, the construction materials of flexure hinge connections and large blocks should be determined properly. In order to obtain widest possible vibration isolation frequency band, the flexure hinge connections' material should have high "Elastic Modulus / Density" ratio. On the other hand, in order to obtain a vibration isolation band at lower frequency region, large blocks' material should have greater density value.

REFERENCES

[1] C. Yilmaz, G. M. Hulbert and N. Kikuchi, Phononic band gaps induced by inertial amplification in periodic media, Physical Review B, v. 76 (5), p. 054309, 2007.

[2] O. Yuksel and C. Yilmaz, Realization of an ultrawide stop band in a 2-d elastic metamaterial with topologically optimized inertial amplification mechanisms, International Journal of Solids and Structures, v. 203, pp. 138-150, 2020.

[3] M. Sigalas and E. N. Economou, Band structure of elastic waves in two dimensional systems, Solid State Communications, v. 86 (3), pp. 141-143, 1993.

[4] Y. Jin, X. Y. Jia, Q. Q. Wu, X. He, G. C. Yu, L. Z. Wu and B. Luo, Design of vibration isolators by using the Bragg scattering and local resonance band gaps in a layered honeycomb meta-sructure, Journal of Sound and Vibration, v. 512, p. 116721, 2022.

[5] Z. Liu, X. Zhang, Y. Mao, Y. Y. Zhu, Z. Yang, C. T. Chan, and P. Sheng, Locally resonant sonic materials, Science, v. 289 (5485), pp. 1734-1736, 2000.

[6] L. Lei, L. Miao, C. Li, X. Liang and J. Wang, Locally resonant periodic wave barriers for vibration isolation in subway engineering, KSCE Journal of Civil Engineering, v. 25, pp. 1239-1251, 2021.

[7] O. Yuksel and C. Yilmaz, Shape optimization of phononic band gap structures incorporating inertial amplification mechanisms, Journal of Sound and Vibration, v. 355, pp. 232-245, 2015.

[8] O. Yuksel and C. Yilmaz, Size and topology optimization of inertial amplification induced phononic band gap structures, Proceedings of the ASME 2017 International Mechanical Engineering Congress and Exposition, v. 13, p. V013T01A007, 2017.

2nd International Natural Science, Engineering and Material Technologies Conference
Sep 15-17, 2022, İğneada-Kırklareli / TÜRKİYE

USING MULTI-CRITERIA DECISION MAKING APPROACH IN INTERNET OF THINGS APPLICATIONS: A BIBLIOMETRIC ANALYSIS

S. Ö. Gönen

Department of Logistics Management, Faculty of Economics and Administrative Sciences, Yeditepe University, Istanbul, TÜRKİYE

E-mail: seza.gonen@yeditepe.edu.tr

Abstract

This study focused on the use of Multi-Criteria Decision Making (MCDM) approach in Internet of Things (IoT) applications. When 105 articles published between 2013 and 2021 were examined, it has been determined that the studies have increased especially in the last two years. Moreover, studies in the field were mostly conducted in subject areas of "Computer Science" and "Engineering". Furthermore, production volumes of journals, countries, organizations and authors were also examined in the study. In addition, analyses of co-authorship, co-occurence and bibliographic coupling were carried out using VOSviewer software. I believe that this study will guide future researchers to see trends, gaps and opportunities in the related field.

Keywords: Bibliometric Analysis, Internet of Things, Multi-Criteria Decision Making

1. INTRODUCTION

Decision making is choosing one of two or more alternatives. When one of these alternatives is better than the other(s), the decision is easy. However, in real life the situation is more complicated because alternatives have different strengths and weaknesses compared to each other. Multi-criteria decision-making techniques have been developed to assist decision makers in such situations.

In the literature, there are bibliometric analysis studies on the use of these techniques in corporate sustainability **[1]**, construction **[2]** and Covid-19 applications **[3]**. However, to the author's knowledge, there is no bibliometric analysis study on the use of MCDM techniques in IoT applications. In this context, a bibliometric analysis study on using MCDM approach in IoT applications was carried out in this study.

IoT is a worldwide network that connects people, things, data, and processes. It can collect information anytime and anywhere. Massive amounts of collected data can be analysed by combining IoT technology with blockchain, big data and artificial intelligence. There are IoT applications in agriculture **[4]**, medicine **[5]**, smart city **[6]**, supply chain management **[7]**, logistics **[8]**, etc.

2. METHOD

The scope of the bibliometric analysis study was limited to the articles indexed in Scopus. Therefore, Articles, Articles in Press and Reviews were included in the study, while other document types (i.e., book chapters, proceedings, etc.) were excluded. In addition, non-English articles were excluded, as well. Since 2022 has not been completed yet, articles published after 2021 were not included in the study.

The query string used in the study was as follows: "*(TITLE-ABS-KEY("multi criteria decision making" OR "multi-criteria decision making" OR "multicriteria decision making" OR MCDM) AND TITLE-ABS-KEY("Internet of Things" OR IoT)) AND (EXCLUDE (PUBYEAR,2023) OR EXCLUDE (PUBYEAR,2022)) AND (LIMIT-TO (DOCTYPE,"ar") OR LIMIT-TO (DOCTYPE,"re")) AND (EXCLUDE (LANGUAGE,"Chinese"))*".

The search resulted in 105 documents. The citation information, bibliographical information, abstract, keywords, and references of these 105 articles were downloaded in a comma-separated file (.csv) from Scopus. VOSviewer software was used for co-authorship analyses (by countries and by organizations), co-occurrence analysis (by keywords) and bibliographic coupling (by documents).

3. RESULTS AND DISCUSSION

3.1. Publications by Year

Fig. 1 depicts the articles over the years from the very first article known in the field to 2021. From the figure, it is obvious that only 4 articles were published in the first 5 years. However, the studies on IoT applications using MCDM approach has gained momentum after 2018. Especially in the last 2 years, more articles have been published (71% of all articles).

3.2. Publications by Subject Area

Table 1 shows the most prolific subject areas, based on the number of published articles. "Computer Science" was the most represented subject area with 60 articles (57% of total articles). It was followed by "Engineering" with 54 articles (51% of total articles). The third largest subject area was "Business, Management and Accounting" with 20 articles (19% of total articles).

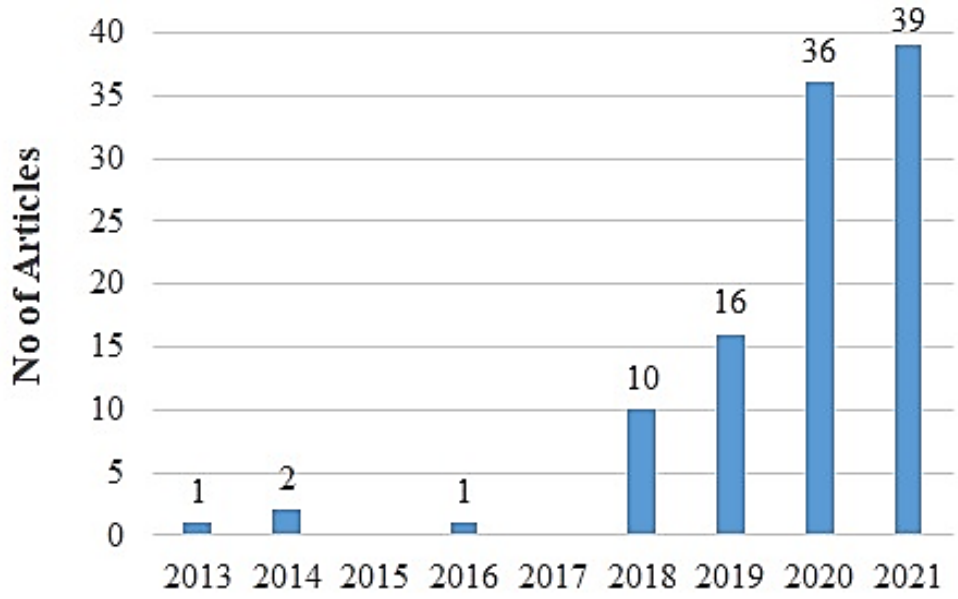

Figure 1: Publications by year.

Table 1: The most prolific subject areas, based on the number of published articles.

Subject Area	No of Articles*	% of 105 Articles
Computer Science	60	57
Engineering	54	51
Business, Management and Accounting	20	19
Environmental Science	14	13
Decision Sciences	12	11
Mathematics	12	11
Energy	11	11
Materials Science	11	11
Social Sciences	10	10

* Please note that the same article can be associated with one or more subject areas.

3.3. Publications by Journal

Articles in the field were published in 76 journals. However, 84% of these journals published only one article and the articles published in these journals corresponded to 61% of all articles. Meanwhile, only three journals published 5 or more articles. 18% of all articles were published by these three journals. The journal that published the most articles was "*IEEE Access*" (**Table 2**). It was followed by "*IEEE Internet of Things Journal*" and "*Sustainability (Switzerland)*", respectively.

Table 2: Top 5 journals, based on the number of published articles.

R	Journal	No of Articles	No of Citations*	% of 1640 Citations**	Impact Factor	Best Quartile
1	*IEEE Access*	8	200	12	3.476	Q1
2	*IEEE Internet of Things Journal*	6	175	11	10.238	Q1
3	*Sustainability (Switzerland)*	5	40	2	3.889	Q1
4	*IEEE Transactions on Industrial Informatics*	4	157	10	11.648	Q1
5	*Journal of Cleaner Production*	3	44	3	11.072	Q1
5	*Sensors (Switzerland)*	3	34	2	3.847	Q1

* No of citations does not include the citations after 2021.

** The number of citations received by 105 articles is 1640. It does not include the citations after 2021.

3.4. Publications by Countries

Articles in the field were published in 45 countries. However, 49% of these countries published only one article. Meanwhile, only five countries published 10 or more articles. 61% of all articles were published by these five countries. The country that published the most articles was India (**Table 3**). It was followed by China and Taiwan, respectively.

Table 3: Top 5 countries, based on the number of published articles.

R	Country	No of Articles	No of Citations*	% of 1640 Citations**	Collaborative Works***	
					No of Articles	No of Countries
1	India	24	208	13	7	9
2	China	19	423	26	14	11
3	Taiwan	12	82	5	8	7
4	Iran	10	9	0.5	5	7
4	United States	10	480	29	9	9
5	Egypt	8	476	29	5	4

* No of citations does not include the citations after 2021.

** The number of citations received by 105 articles is 1640. It does not include the citations after 2021.

*** "Collaborative works" represents studies published by authors affiliated with organizations in different countries. "No of articles" in this column refers to the number of articles published in collaboration with authors from other countries. "No of countries" in this column represents the number of countries with which authors from that country have collaborated.

On the other hand, co-authorship analysis by countries was also performed. The co-authorship network shown in **Fig. 2** was generated with 12 countries that published minimum 5 articles in the field. The node size of each country indicates its publication volume, while lines and distances between nodes represent co-authorship in the articles.

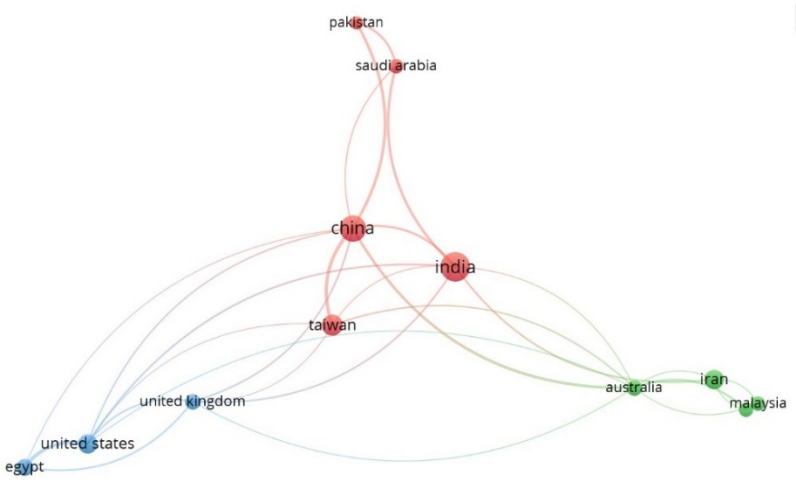

Figure 2: Co-authorship network between countries.

3.5. Publications by Organizations

Articles in the field were published in 160 organizations. However, 79% of these organizations published only one article. Meanwhile, only one organization (Zagazig University, Egypt) published 5 or more articles. Of the 8 articles published by Zagazig University, seven articles were published in collaboration with authors affiliated with different organizations (**Fig. 3**). These organizations are located in four different countries (i.e., United States, United Kingdom, Viet Nam, and China).

3.6. Publications by Authors

Articles in the field were published by 357 authors. However, 87% of these authors published only one article. Meanwhile, only one author (Abdel-Basset, M.) published 5 or more articles. Abdel-Basset is affiliated with Zagazig University, the organization that published the most articles, and was one of the authors of 7 of 8 articles of this university. Besides, 29% of all citations were received by articles published by him.

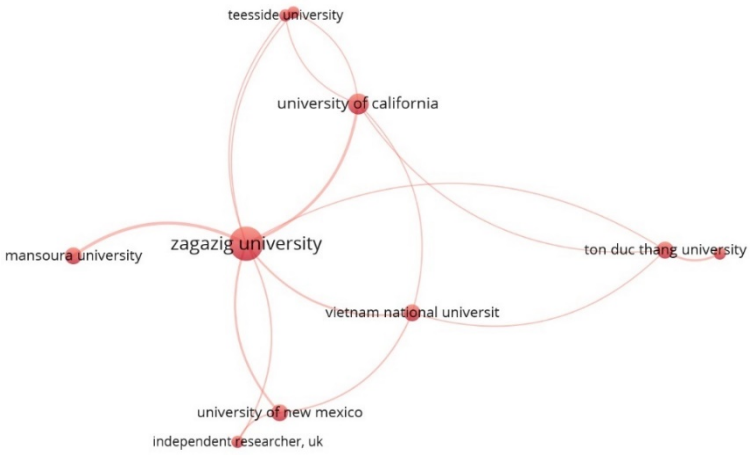

Figure 3: Co-authorship network of Zagazig University.

3.7. Keyword Analysis

From 105 articles, 983 keywords were identified. 98% of them appeared 5 times or less, while 1% of them appeared 10 times or more in the articles. The three most frequently repeated words were "Internet Of Things", "Decision Making", and "Multi-criteria Decision Making", respectively. However, various versions of these words have also been used as keywords. For instance, "Internet Of Thing", "Internet Of Thing (IOT)", "Internet Of Things (IOT)", "Internet Of Things (IoT)", "Internet-of-Things", and "IoT" were among different versions of "Internet Of Things". Similarly, "Decision-making", "Decision-making (DM)" and "Decisions Makings" were some of the versions of "Decision Making". Moreover, many versions of "Multi-criteria Decision Making" were also used as keywords. Some of them were as follows: "MCDM", "Multi Criteria Decision Making", "Multi Criteria Decision-making", "Multi- Criteria Decision- Making (MCDM)", "Multi-Criteria Decision Making (MCDM)", "Multi-Criteria Decision-Making", "Multi-criteria Decision Making (MCDM)", "Multi-criteria Decision-making", "Multi-criterion Decision-making", "Multicriteria Decision Making", "Multicriteria Decision Making (MCDM)", "Multicriteria Decision-making", "Multicriteria Decision-making (MCDM)", "Multicriterion Decision Makings", "Multiple Criteria Decision Making", "Multiple Criteria Decision Making (MCDM)", "Multiple Criteria Decision-making", and "Multiple-criteria Decision Making (MCDM)". Therefore, some keywords were different versions of each other. Thus, they were defined as synonyms while making co-occurence analysis. As a result, the co-occurence network given in **Fig. 4** was obtained with 17 keywords, selected from a minimum 5 occurences. The node size of each keyword

indicates its occurences, while lines and distances between nodes represent co-occurence of these keywords in the articles.

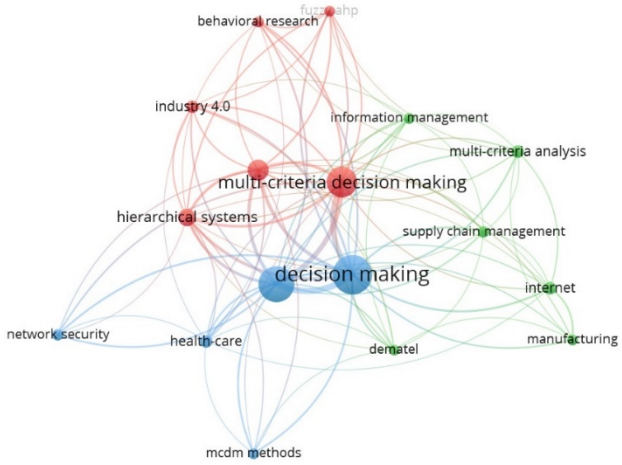

Figure 4: Co-occurence network between keywords.

3.8. Analysis of Citations

The most cited articles were identified and listed in **Table 4**. In addition, bibliographic coupling analysis was performed. All articles were clustered into five.

Table 4: The most cited 5 articles, based on the average citations by year.

R	Authors	Year	Article Title	No of Citations*	Average Citations by Year
1	Xu et al. **[9]**	2020	BeCome: blockchain-enabled computation offloading for IoT in mobile edge computing	128	64.0
2	Abdel-Basset et al. **[10]**	2018	Internet of things (IoT) and its impact on supply chain: a framework for building smart, secure and efficient systems	190	47.5
3	Abdel-Basset et al. **[11]**	2020	A bipolar neutrosophic multi criteria decision making framework for professional selection	77	38.5
4	Mourtzis & Vlachou **[12]**	2018	A cloud-based cyber-physical system for adaptive shop-floor scheduling and condition-based maintenance	139	34.8
5	Moktadir et al. **[13]**	2018	Assessing challenges for implementing Industry 4.0: Implications for process safety and environmental protection	128	32.0

* No of citations does not include the citations after 2021.

Cluster 1 contained 26 studies, including those focused on presenting a mobility aware container migration algorithm for cloudlet-enabled IoT systems **[14]**, selecting phantom node to preserve vehicle location privacy **[15]**, evaluating trustworthiness of neighbor node in wireless sensor networks **[16]**, proposing a service placement methodology for fog computing environment **[17]**, suggesting a trust-oriented IoT service placement method for smart cities in edge computing **[18]**, investigating the performance of MCDM-based load balancing scheme among gateways in fog-based IoT **[19]**, introducing a switch migration based load balancing framework that uses MCDM method for selecting a target controller **[20]**, proposing a blockchain-enabled computation offloading method that utilizes MCDM to optimize the offloading strategy **[9]**, suggesting a health security framework in IoT **[21]**, ranking challenging factors for security of IoT technology **[22]**, prioritizing critical success factors of cloud enterprise resource planning **[23]**, classifying IoT applications **[24]**, and assessing factors that hinder the adoption of internet of medical things **[25]**.

Cluster 2 consisted of 20 studies, such as those aimed at proposing a framework for returning the most pertinent IoT resource as user query response **[26]**, developing an IoT-based mhealth framework for chronic heart disease patients **[27]**, presenting a framework for evaluating the security features of internet of health things based device in the healthcare environment **[28]**, suggesting a framework for a real-time automated energy management system by IoT sensors **[29]**, making a context-aware selection of the best sensors in an IoT architecture **[30]**, presenting a framework for selecting among IoT-based service providers **[31]**, developing a decision making tool to select the best candidate for a job **[32]**, and evaluating a multi-agent learning neural network and Bayesian model for real-time IoT-based skin detectors **[33]**.

Cluster 3 included 20 studies, including those addressed the implementation of an IoT-based tool for assessing employee performance **[34]**, the selection of third party logistics service providers for IoT-based agriculture supply chain management **[35]**, the evaluation of the importance of security criteria for IoT-based supply chain system **[36]**, the assessment of IoT information security risks **[37]**, the prioritization of key digitization enablers and the comparison of the supply chain performance of organizations **[38]**, the ranking of smart manufacturing drivers **[39]**, the prioritization of factors that affect IoT adoption of manufacturing companies **[40]**, the assessment of IoT adoption barriers of waste management systems of smart cities **[41]**, the evaluation of IoT adoption barriers in food retail supply chains **[42]**, the establishment of a smart hospital

evaluation system **[43]**, the comparison of e-health IoT applications for individuals **[44]**, and the selection of IoT technologies for deployment in energy industry **[45]**.

Cluster 4 contained 17 studies, including those focused on choosing industrial IoT platform for digital servitization **[46]**, evaluating IoT platforms **[47]**, selecting IoT cloud platform **[48]**, building IoT smart sensor network **[49]**, evaluating trustworthiness of vehicular clouds **[50]**, proposing an edge based enterprise system for product design scheme evaluation **[51]**, assessing design alternatives of end-of-life products using IoT **[52]**, prioritizing areas of IoT application in agriculture sector **[53]**, selecting distributed stream processing frameworks for IoT applications **[54]**, and evaluating fog-based IoT security factors **[55]**.

Cluster 5 consisted of 12 studies, including those aimed at suggesting a framework based on computer propped diagnosis and IoT for type-2 diabetes patients **[56]** and heart failure infected patients **[57]**, prioritizing factors in consumer adoption of mobile health services and comparing mobile health care products **[58]**, and assessing the performance of the IoT-based supply chain of e-commerce companies **[59]**.

4. CONCLUSION

In this study, it was aimed to make a bibliometric analysis on using MCDM approach in IoT applications. For this purpose, 105 articles published between 2013 and 2021 were examined. 71% of these articles were published in the last two years and the subject area of 57% of the articles was “Computer Science”. Moreover, 61% of the articles were published in one of the journals that published only a single article. Although India was the country that published the most articles, the publications of USA, Egypt and China have received more citations. On the other hand, the organization that published the most articles was Zagazig University in Egypt. While the author that published the most articles was Abdel-Basset from Zagazig University. Meanwhile, the most repeated keywords were "Internet of Things", "Decision Making", and "Multi-Criteria Decision Making". These findings summarize the current state of the literature and have the potential to give inspiration for future researches.

REFERENCES

[1] Chowdhury, P., & Paul, S.K. (2020). Applications of MCDM methods in research on corporate sustainability: A systematic literature review. *Management of Environmental Quality: An International Journal*, 31 (2), 385-405.

[2] Zhu, X., Meng, X., & Zhang, M. (2021). Application of multiple criteria decision making methods in construction: A systematic literature review. *Journal of Civil Engineering and Management*, 27 (6), 372-403.

[3] Alsalem, M.A., Alamoodi, A.H., Albahri, O.S., Dawood, K.A., Mohammed, R.T., Alnoor, A., Zaidan, A.A., Albahri, A.S., Zaidan, B.B., Jumaah, F.M., & Al-Obaidi, J.R. (2022). Multi-criteria decision-making for coronavirus disease 2019 applications: a theoretical analysis review. *Artificial Intelligence Review*, 55 (6), 4979-5062.

[4] Rejeb, A., Rejeb, K., Abdollahi, A., Al-Turjman, F., & Treiblmaier, H. (2022). The interplay between the internet of things and agriculture: A bibliometric analysis and research agenda. *Internet of Things (Netherlands)*, 19, 100580.

[5] Sadoughi, F., Behmanesh, A., & Sayfouri, N. (2020). Internet of things in medicine: A systematic mapping study. *Journal of Biomedical Informatics*, 103, 103383.

[6] Rejeb, A., Rejeb, K., Simske, S., Treiblmaier, H., & Zailani, S. (2022). The big picture on the internet of things and the smart city: a review of what we know and what we need to know. *Internet of Things (Netherlands)*, 19, 100565.

[7] Rejeb, A., Simske, S., Rejeb, K., Treiblmaier, H., & Zailani, S. (2020). Internet of things research in supply chain management and logistics: A bibliometric analysis. *Internet of Things (Netherlands)*, 12, 100318.

[8] Ding, Y., Jin, M., Li, S., & Feng, D. (2021). Smart logistics based on the internet of things technology: an overview. *International Journal of Logistics Research and Applications*, 24 (4), 323-345.

[9] Xu, X., Zhang, X., Gao, H., Xue, Y., Qi, L., & Dou, W. (2020). BeCome: blockchain-enabled computation offloading for IoT in mobile edge computing. *IEEE Transactions on Industrial Informatics*, 16 (6), 4187-4195.

[10] Abdel-Basset, M., Manogaran, G., & Mohamed, M. (2018). Internet of things (IoT) and its impact on supply chain: A framework for building smart, secure and efficient systems. *Future Generation Computer Systems*, 86, 614-628.

[11] Abdel-Basset, M., Gamal, A., Son, L.H., & Smarandache, F. (2020). A bipolar neutrosophic multi criteria decision making framework for professional selection. *Applied Sciences (Switzerland)*, 10 (4), 1202.

[12] Mourtzis, D., & Vlachou, E. (2018). A cloud-based cyber-physical system for adaptive shop-floor scheduling and condition-based maintenance. *Journal of Manufacturing Systems*, 47, 179-198.

[13] Moktadir, M.A., Ali, S.M., Kusi-Sarpong, S., & Shaikh, M.A.A. (2018). Assessing challenges for implementing Industry 4.0: Implications for process safety and environmental protection. *Process Safety and Environmental Protection*, 117, 730-741.

[14] Al-Tarawneh, M.A.B. (2020). Mobility-aware container migration in cloudlet-enabled IoT systems using integrated muticriteria decision making. *International Journal of Advanced Computer Science and Applications*, 11 (9), 694-701.

[15] Farman, H., Khalil, A., Ahmad, N., Albattah, W., Khan, M.A., & Islam, M. (2021). A privacy preserved, trust relationship (Ptr) model for internet of vehicles. *Electronics (Switzerland)*, 10 (24), 3105.

[16] Gautam, A.K., & Kumar, R. (2021). A trust based neighbor identification using MCDM model in wireless sensor networks. *Recent Advances in Computer Science and Communications*, 14 (4), 1336-1351.

[17] Varshney, S., Sandhu, R., & Gupta, P.K. (2020). QoE-based multi-criteria decision making for resource provisioning in fog computing using AHP technique. *International Journal of Knowledge and Systems Science*, 11 (4), 17-30.

[18] Xu, X., Liu, X., Xu, Z., Dai, F., Zhang, X., & Qi, L. (2020). Trust-oriented IoT service placement for smart cities in edge computing. *IEEE Internet of Things Journal*, 7 (5), 4084-4091.

[19] Banaie, F., Yaghmaee, M.H., Hosseini, S.A., & Tashtarian, F. (2020). Load-balancing algorithm for multiple gateways in fog-based internet of things. *IEEE Internet of Things Journal*, 7 (8), 7043-7053.

[20] Sahoo, K.S., Puthal, D., Tiwary, M., Usman, M., Sahoo, B., Wen, Z., Sahoo, B.P.S., & Ranjan, R. (2020). ESMLB: efficient switch migration-based load balancing for multicontroller SDN in IoT. *IEEE Internet of Things Journal*, 7 (7), 5852-5860.

[21] Haghparast, M.B., Berehlia, S., Akbari, M., & Sayadi, A. (2021). Developing and evaluating a proposed health security framework in IoT using fuzzy analytic network process method. *Journal of Ambient Intelligence and Humanized Computing*, 12 (2), 3121-3138.

[22] Akbar, M.A., Alsanad, A., Mahmood, S., & Alothaim, A. (2021). A multicriteria decision making taxonomy of IoT security challenging factors. *IEEE Access*, 9, 128841-128861.

[23] Naveed, Q.N., Islam, S., Qureshi, M.R.N.M., Aseere, A.M., Rasheed, M.A.A., & Fatima, S. (2021). Evaluating and ranking of critical success factors of cloud enterprise resource planning adoption using MCDM approach. *IEEE Access*, 9, 156880-156893.

[24] Mashal, I., & Alsaryrah, O. (2020). Fuzzy analytic hierarchy process model for multi-criteria analysis of internet of things. *Kybernetes*, 49 (10), 2509-2520.

[25] Tariq, M.I., Mian, N.A., Sohail, A., Alyas, T., & Ahmad, R. (2020). Evaluation of the challenges in the internet of medical things with multicriteria decision making (AHP and TOPSIS) to overcome its obstruction under fuzzy environment. *Mobile Information Systems*, 2020, 8815651.

[26] Vandana, C.P., & Chikkamannur, A.A. (2021). Multi criteria decision based ranked discovery framework for IoT resources. *Indian Journal of Computer Science and Engineering*, 12 (5), 1425-1441.

[27] Albahri, A.S., Zaidan, A.A., Albahri, O.S., Zaidan, B.B., Alamoodi, A.H., Shareef, A.H., Alwan, J.K., Hamid, R.A., Aljbory, M.T., Jasim, A.N., Baqer, M.J., & Mohammed, K.I. (2021). Development of IoT-based mhealth framework for various cases of heart disease patients. Health and Technology, 11 (5), 1013-1033.

[28] Wang, L., Ali, Y., Nazir, S., & Niazi, M. (2020). ISA evaluation framework for security of internet of health things system using AHP-TOPSIS methods. *IEEE Access*, 8, 152316-152332.

[29] Bapat, H., Sarkar, D., & Gujar, R. (2021). Application of integrated fuzzy FCM-BIM-IoT for sustainable material selection and energy management of metro rail station box project in western India. *Innovative Infrastructure Solutions*, 6 (2), 73.

[30] Kertiou, I., Benharzallah, S., Kahloul, L., Beggas, M., Euler, R., Laouid, A., & Bounceur, A. (2018). A dynamic skyline technique for a context-aware selection of the best sensors in an IoT architecture. *Ad Hoc Networks*, 81, 183-196.

[31] Singh, M., Baranwal, G., & Tripathi, A.K. (2020). QoS-aware selection of IoT-based service. *Arabian Journal for Science and Engineering*, 45 (12), 10033-10050.

[32] Nallakaruppan, M.K., & Kumaran, U.S. (2018). Quick fix for obstacles emerging in management recruitment measure using IOT-based candidate selection. *Service Oriented Computing and Applications*, 12 (3-4), 275-284.

[33] Zaidan, A.A., Zaidan, B.B., Alsalem, M.A., Albahri, O.S., Albahri, A.S., & Qahtan, M.Y. (2020). Multi-agent learning neural network and Bayesian model for real-time IoT skin detectors: a new evaluation and benchmarking methodology. *Neural Computing and Applications*, 32 (12), 8315-8366.

[34] Alti, A., & Almuhirat, A. (2021). An advanced IoT-based tool for effective employee performance evaluation in the banking sector. *Ingenierie des Systemes d'Information*, 26 (1), 103-108.

[35] Yadav, S., Garg, D., & Luthra, S. (2020). Selection of third-party logistics services for internet of things-based agriculture supply chain management. *International Journal of Logistics Systems and Management*, 35 (2), 204-230.

[36] Nozari, H., Fallah, M., Szmelter-Jarosz, A., & Krzemiński, M. (2021). Analysis of security criteria for IoT-based supply chain: a case study of FMCG industries. *Central European Management Journal*, 29 (4), 149-171.

[37] Bharathi, S.V. (2019). Forewarned is forearmed: assessment of IoT information security risks using analytic hierarchy process. *Benchmarking*, 26 (8), 2443-2467.

[38] Gupta, H., Kumar, S., Kusi-Sarpong, S., Jabbour, C.J.C., & Agyemang, M. (2021). Enablers to supply chain performance on the basis of digitization technologies. *Industrial Management and Data Systems*, 121 (9), 1915-1938.

[39] Malaga, A., & Vinodh, S. (2021). Benchmarking smart manufacturing drivers using Grey TOPSIS and COPRAS-G approaches. *Benchmarking*, 28 (10), 2916-2951.

[40] Asadi, S., Nilashi, M., Iranmanesh, M., Hyun, S.S., & Rezvani, A. (2021). Effect of internet of things on manufacturing performance: A hybrid multi-criteria decision-making and neuro-fuzzy approach. *Technovation*, 102426.

[41] Sharma, M., Joshi, S., Kannan, D., Govindan, K., Singh, R., & Purohit, H.C. (2020). Internet of things (IoT) adoption barriers of smart cities' waste management: An Indian context. *Journal of Cleaner Production*, 270, 122047.

[42] Kamble, S.S., Gunasekaran, A., Parekh, H., & Joshi, S. (2019). Modeling the internet of things adoption barriers in food retail supply chains. *Journal of Retailing and Consumer Services*, 48, 154-168.

[43] Lin, C.L., Chen, J.K.C., & Ho, H.H. (2021). Bim for smart hospital management during covid-19 using MCDM. *Sustainability (Switzerland)*, 13 (11), 6181.

[44] Zadtootaghaj, P., Mohammadian, A., Mahbanooei, B., & Ghasemi, R. (2019). Internet of things: A survey for the individuals' e-health applications. *Journal of Information Technology Management*, 11 (1), 102-129.

[45] Maryska, M., Doucek, P., Sladek, P., & Nedomova, L. (2019). Economic efficiency of the internet of things solution in the energy industry: A very high voltage frosting case study. *Energies*, 12 (4), 585.

[46] Zhou, T., Ming, X., Chen, Z., & Miao, R. (2021). Selecting industrial IoT platform for digital servitisation: a framework integrating platform leverage practices and cloud HBWM-TOPSIS approach. *International Journal of Production Research*, 1-23.

[47] Lin, M., Huang, C., Xu, Z., & Chen, R. (2020). Evaluating IoT platforms using integrated probabilistic linguistic MCDM method. *IEEE Internet of Things Journal*, 7 (11), 11195-11208.

[48] Chakraborty, A., Jindal, M., Khosravi, M.R., Singh, P., Shankar, A., & Diwakar, M. (2021). A secure IoT-based cloud platform selection using entropy distance approach and fuzzy set theory. *Wireless Communications and Mobile Computing*, 2021, 6697467.

[49] Wang, J., Yeh, W.C., Xiong, N.N., Wang, J., He, X., & Huang, C.L. (2019). Building an improved internet of things smart sensor network based on a three-phase methodology. *IEEE Access*, 7, 141728-141737.

[50] Aladwan, M.N., Awaysheh, F.M., Alawadi, S., Alazab, M., Pena, T.F., & Cabaleiro, J.C. (2020). TrustE-VC: trustworthy evaluation framework for industrial connected vehicles in the cloud. *IEEE Transactions on Industrial Informatics*, 16 (9), 6203-6213.

[51] Lou, S., Feng, Y., Li, Z., Zheng, H., Gao, Y., & Tan, J. (2021). An edge-based distributed decision-making method for product design scheme evaluation. *IEEE Transactions on Industrial Informatics*, 17 (2), 1375-1385.

[52] Joshi, A.D., & Gupta, S.M. (2019). Evaluation of design alternatives of end-of-life products using internet of things. *International Journal of Production Economics*, 208, 281-293.

[53] Mohammadian, A., Heidary Dahooie, J., Qorbani, A.R., Zavadskas, E.K., & Turskis, Z. (2021). A new multi-attribute decision-making framework for policy-makers by using interval-valued triangular fuzzy numbers. *Informatica (Netherlands)*, 32 (3), 583-618.

[54] Lin, Z., Huang, C., & Lin, M. (2021). Probabilistic hesitant fuzzy methods for prioritizing distributed stream processing frameworks for IoT applications. *Mathematical Problems in Engineering*, 2021, 6655477.

[55] Verma, R., & Chandra, S. (2021). Interval-valued intuitionistic fuzzy-analytic hierarchy process for evaluating the impact of security attributes in fog based internet of things paradigm. *Computer Communications*, 175, 35-46.

[56] Abdel-Basset, M., Manogaran, G., Gamal, A., & Chang, V. A (2020). Novel intelligent medical decision support model based on soft computing and IoT. *IEEE Internet of Things Journa*l, 7 (5), 4160-4170.

[57] Abdel-Basset, M., Gamal, A., Manogaran, G., Son, L.H., & Long, H.V. (2020). A novel group decision making model based on neutrosophic sets for heart disease diagnosis. *Multimedia Tools and Applications*, 79 (15-16), 9977-10002.

[58] Liu, Y., Yang, Y., Liu, Y., & Tzeng, G.H. (2019). Improving sustainable mobile health care promotion: A novel hybrid MCDM method. *Sustainability (Switzerland)*, 11 (3), 752.

[59] Grida, M., Mohamed, R., & Zaied, A.N.H. (2020). A novel plithogenic MCDM framework for evaluating the performance of IoT based supply chain. *Neutrosophic Sets and Systems*, 33, 223-341.

2nd International Natural Science, Engineering and Material Technologies Conference
Sep 15-17, 2022, İğneada-Kırklareli / TÜRKİYE

MORPHOLOGICAL CHARACTERIZATION OF AL BASED HYBRID COMPOSITE POWDERS VIA MECHANICAL ALLOYING

E. Dağaşan Bulucu[1], M. E. Palaz[1]

[1]*Department of Materials Science and Engineering, Faculty of Engineering, Erciyes University, Kırklareli, TÜRKİYE*

E-mail: edagasan@erciyes.edu.tr

Abstract

This paper involves morphological studies conducted on Al based hybrid particulate composites reinforced via ball milling process. Al_2O_3, SiC, B_4C and ZrO_2 ceramic powders were introduced into the metal matrix at different weight ratios. Ball milling process was conducted by a planetary type ball mill with WC milling balls and vial. Parameters like rotating speed, time, Ball-to-Powder ratio and Process Control Agent were kept constant as 200 rpm, 100 hrs, 10:1 and % 1.5 wt. stearic acid, respectively. Powder samples that taken from the composite mixture by time intervals of 20 hours were analyzed by FESEM and XRD. Particle size measurements were also conducted on FESEM images by an image analyzing software.

Keywords: Mechanical Alloying, Ball Milling, Aluminium Matrix Composites, Hybrid Particulate Composites, Microstructural Characterization

1. INTRODUCTION

Due to ease of formability and lightweight, aluminum is finding many applications in industrial area [1]. But because of poor elevated temperature properties of aluminum and its alloys, much research work had been carried out to strengthen them by producing aluminum matrix composites [2]. Especially ceramic particulate reinforced Al matrix composites (AMC) are extremely studied due to advantageous mechanical properties like high specific strength and elastic modulus. Besides that, AMC provide additional properties like low thermal expansion coefficient and good wear resistance [3]. Common reinforcing elements for Al and its alloys are ceramic particles like SiC [4], Si_3N_4 [1], Al_2O_3 [5, 6], SiO_2 [7] and B_4C [3, 8] because of their low density and high hardness values.

On the other hand, mechanical alloying (MA) is a solid-state technique and allows production of homogeneous materials [9, 10]. The technique was invented as a result of research conducted on nickel-based superalloys by INCO [9, 10, 11]. The method can be used to synthesize various interesting solid-state materials, such as amorphous, quasicrystalline and nanocrystalline alloys or composites [9]. Ball milling can also be defined as a method for producing composite metal powders with a controlled fine microstructure [12]. It occurs by the repeated fracturing and rewelding of a mixture of powder particles in a high energy ball mill [11].

In mechanical alloying process powder particles are subjected to repeated cold welding, fracturing, and rewelding. The transfer of mechanical energy to the powder particles results in introduction of strain into the powder through generation of dislocations and other defects which act as fast diffusion paths [10].

Planetary Ball Mill is one of the most popular mills used in MA. In this type of mill, the milling media have considerably high energy, because starting materials and grinding media (balls) come off the inner wall of the vial and the effective centrifugal force reaches up to twenty times gravitational acceleration [11]. Since the supporting disc and the vial rotate opposite directions, the centrifugal forces alternately are synchronized and opposite. Therefore, the milling media and the charged powders alternatively roll on the inner wall of the vial, and are lifted and thrown off across the bowl at high speed (Figure 1) [11].

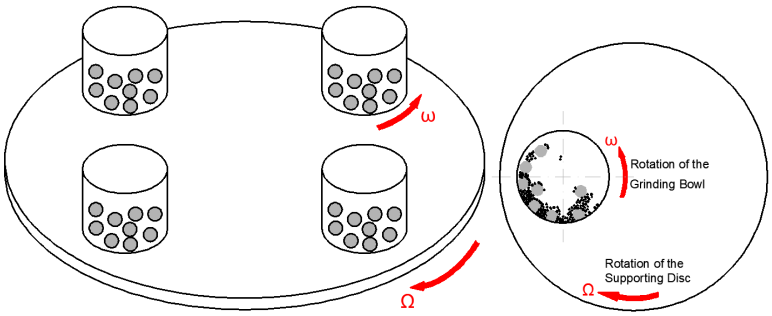

Figure 1. Schematical View of a Planetary Ball Mill.

2. EXPERIMENTAL DETAILS

2.1. Materials

In order to produce hybrid powder mixtures, Al matrix is supported by different ceramic powders such as Al_2O_3, B_4C, SiC (5 % wt.) and also ZrO_2 (at different % wt. ratios of 5 and 10). Properties of used matrix and reinforcing powders are given in Table 1 and also reinforcement type and ratio of each specimen can be seen in Table 2.

Table 1. Properties of the Materials.

Material	Particle Size (µm)	Purity (%)	Supplier/Product Code	Hardness (HV)	Density (g/cm^3)
Al	0-50	99,9	Aldrich/11010		2,70
SiC	37	99	Alfa Aesar 357391	2600	3,22
B_4C	22-59	99+	Alfa Aesar/10922	4000	2,52
Al_2O_3	44	99,8	AEE/Al-602	2100	3,98
ZrO_2	10-50	99,9	AEE/Zr-604	1200	4,25

Table 2. Type and % wt. of Reinforcements in Specimens.

Specimen Code	CONTENT				
	Al	**Al_2O_3**	**SiC**	**B_4C**	**ZrO_2**
A	90 %	5 %	-	-	5 %
B	85 %	5 %	-	-	10 %
C	90 %	-	5 %	-	5 %
D	85 %	-	5 %	-	10 %
E	90 %	-	-	5 %	5 %
F	85 %	-	-	5 %	10 %

2.2. Mechanical Alloying Process

Reinforcing powders were introduced into the Al matrix by mechanical alloying. A FRITSCH Pulverisette 6 classical line planetary ball with one station was utilized for this purpose. 250 ml WC vial and WC balls were used during ball mil. In order to take advantage from both weight and surface area of balls, both 10 mm and 20 mm diameter balls were used together by adjusting Ball to Powder ratio as constant as 10:1. % 1.5 wt. stearic acid was also added into each powder as lubricant.

To produce a homogeneous distribution milling speed and milling time were kept constant as 200 rpm and 100 hours, respectively due to previous studies conducted. Mechanical alloying atmosphere was chosen as high purity argon supplied by an MBRAUN-GB-2202-PVAC type glove box in order to prevent oxidation.

To determine morphological evolution of the powders, mechanical alloying process was interrupted by time intervals of 20 hours to take specimens from the powder mixture.

2.3. FESEM Analysis

Investigation of the micro structural evolution of composite powder mixtures and composites was conducted by ZEISS Gemini 500 type Field emission scanning electron microscope. FESEM images were taken at different magnitudes of 500 X, 1 KX, 5 KX, 10 KX and 20 KX.

2.4. Particle Size Analysis

While evaluating the particle size evolution of powder mixtures during ball milling operation, 12 images were taken from each specimen at six different magnitudes of 100X, 500X, 1 KX, 2 KX, 5 KX, 10 KX and 20 KX. Micrograms were then processed by Image ProPlus software for each specimen.

2.5. XRD Analysis

XRD analyzes were conducted to investigate morphological structure. XRD tests were performed by a BRUKER AXS D8 Advance type analyzer with Cu Kα radiation (λ=0,15406 nm) by using a voltage of 40 kV and a current of 40 mA. XRD patterns were recorded in the 2θ range 10-90° with step of 0.02 °.

3. RESULTS AND DISCUSSION

3.1. FESEM Results

In order to observe micro structural evolution of powders, FESEM images of both as-received and mechanical alloyed powders were taken. Figure 2 gives FESEM micrograms of as received Al, SiC, B_4C, Al_2O_3 and ZrO_2 powders.

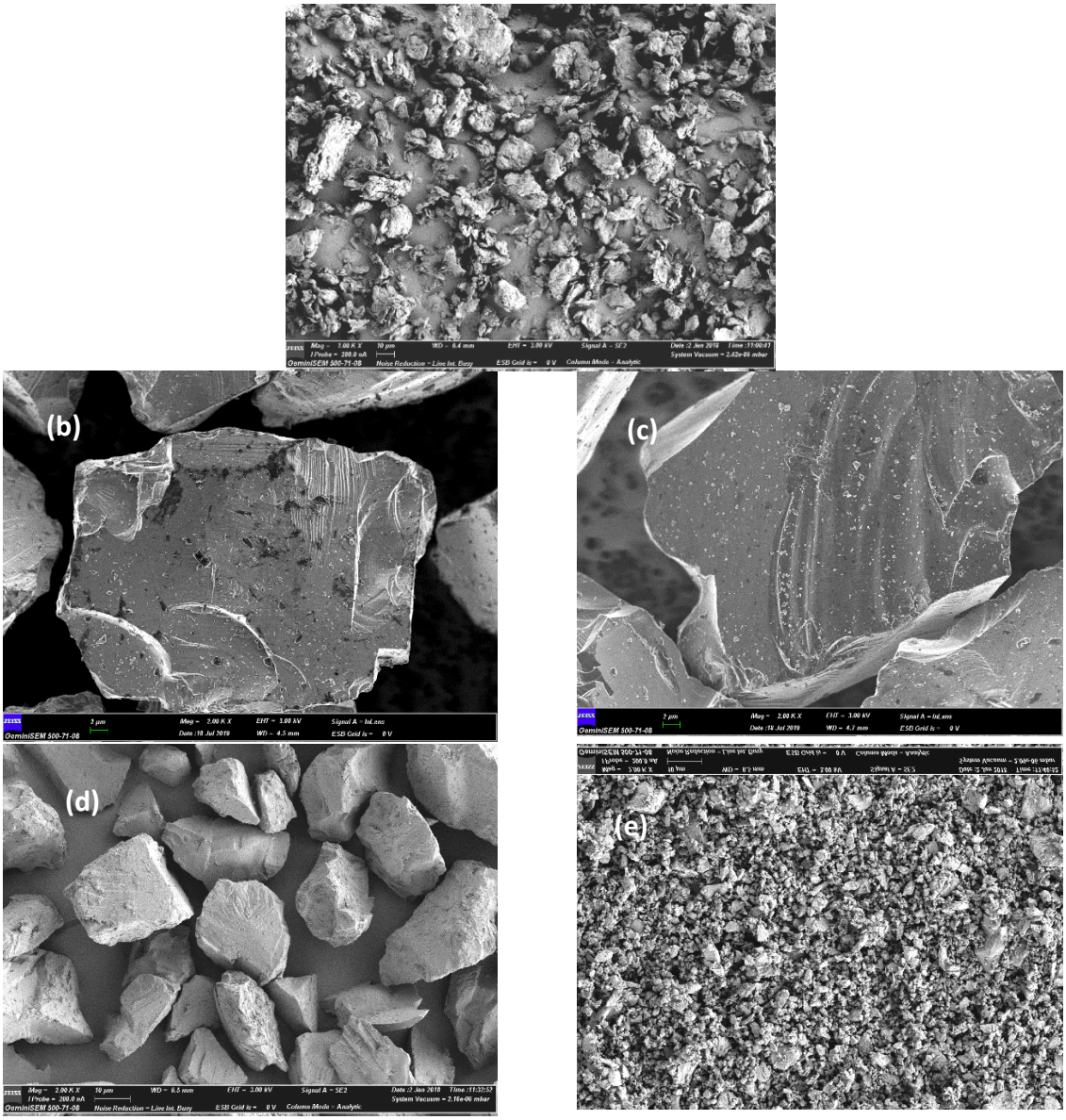

Figure 2. FESEM Images of as received (a) Al, (b) SiC, (c) B_4C, (d) Al_2O_3 and (e) ZrO_2.

Figure 3, illustrates microstructural evolution of the Specimen A (which contains 90 % wt. Al, 5 % wt. Al_2O_3 and 5 % wt. ZrO_2) due to milling time.

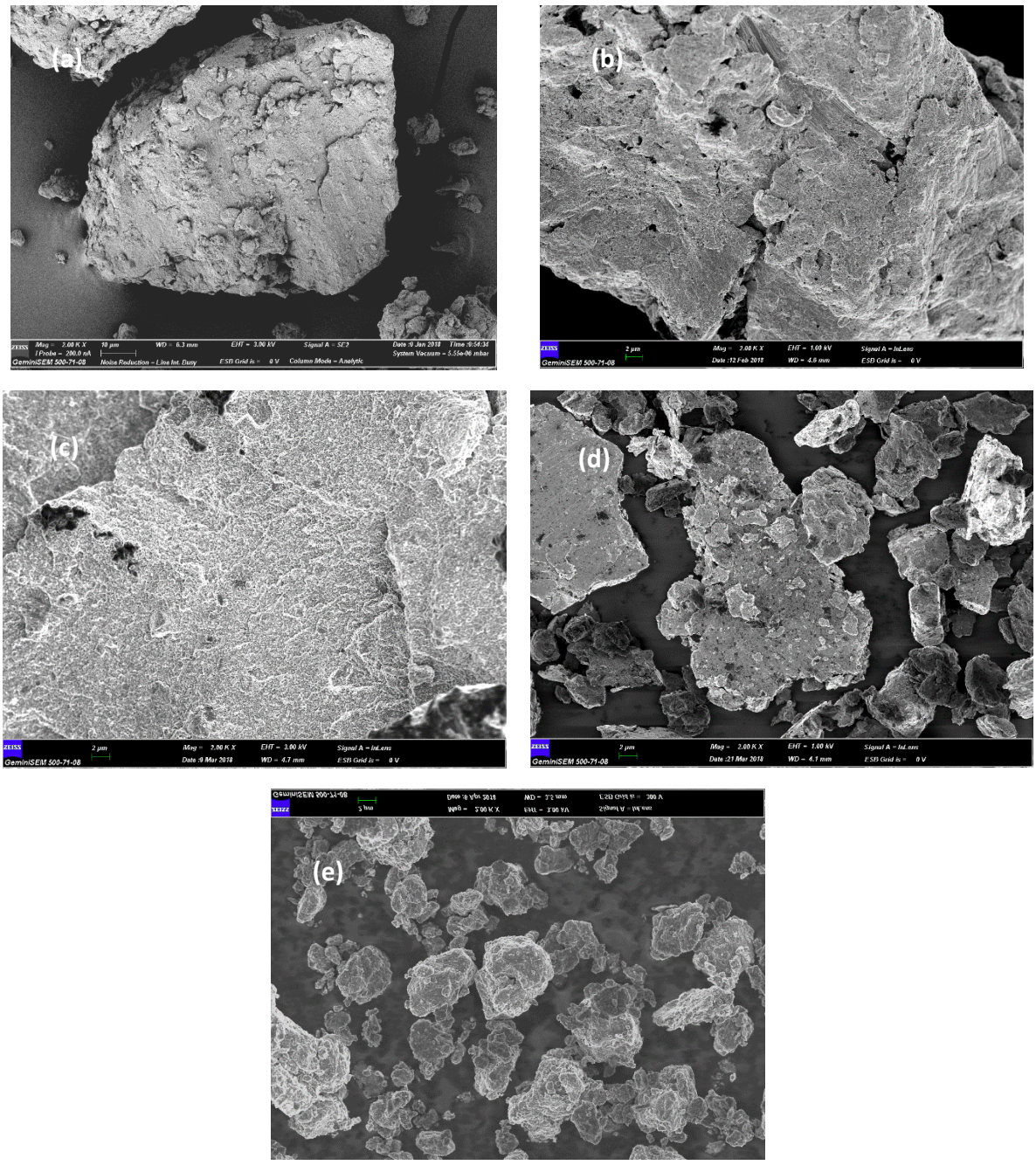

Figure 3. FESEM Images of Al, 5 % wt. Al_2O_3 and 5 % wt. ZrO_2 Powder Mixtures Milled for (a) 20, (b) 40, (c) 60 , (d) 80 and (e) 100 Hours.

Due to these images, it can be clearly said that, at initial stages of milling the brittle components like Al_2O_3 and ZrO_2 start to break into small pieces and some of the pieces cold welded onto the ductile component (Al). If milling continues to 40 hours cold welding and subsequent recovery takes place and particles collide. When milling time reaches 60 hours the powder mixture show tendency to flatten. As the milling time goes further, after 80 hours, the powder mixture breaks into small pieces again. After 100 hours, it is obvious that particles get homogenized by means of particle size and shape. Microstructures of Al-5 % wt. Al_2O_3-10 % wt. ZrO_2 composite powders (Specimen B) ball milled for 20, 40, 60,80 and 100 hours are given in Figure 4.

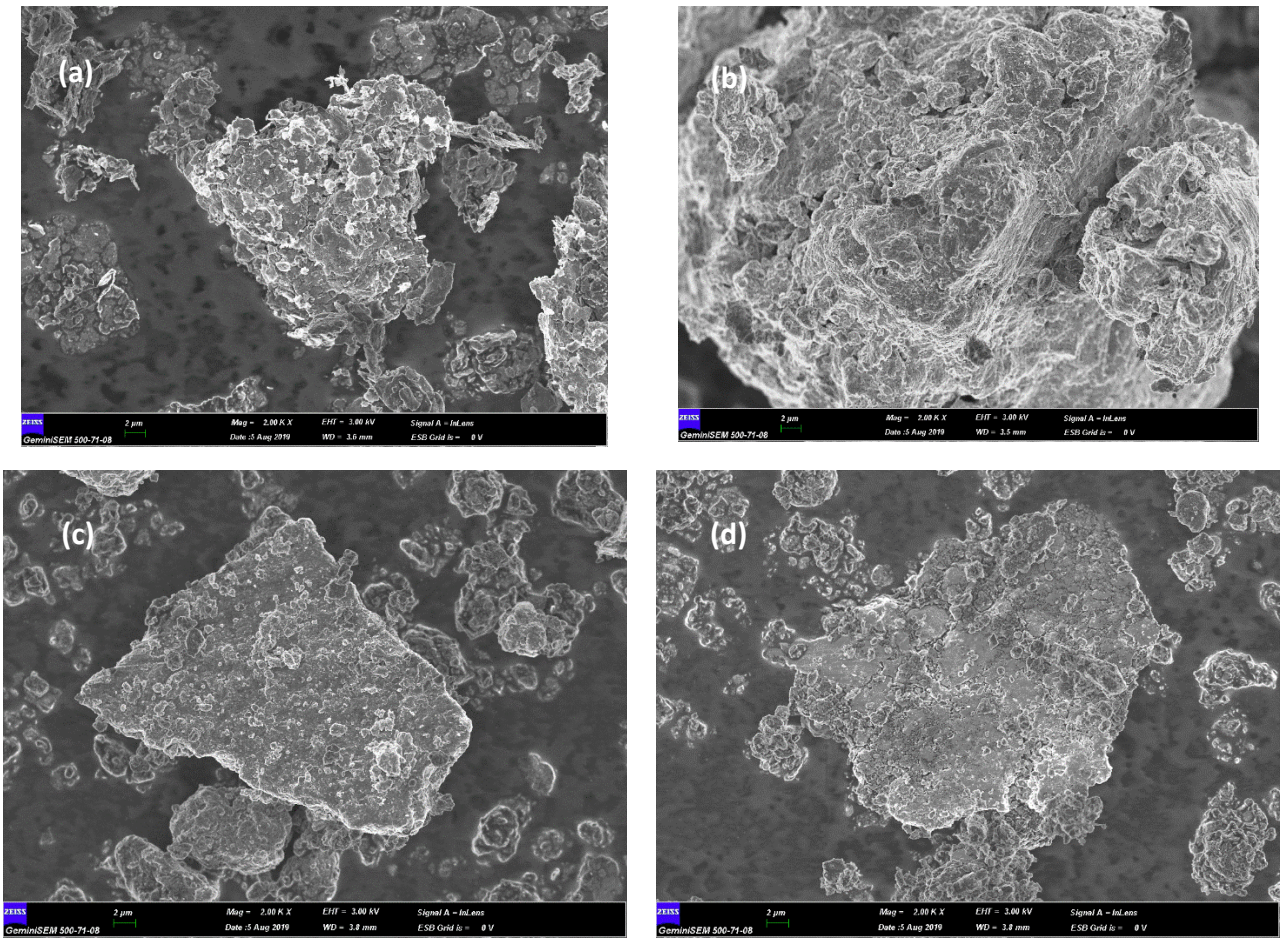

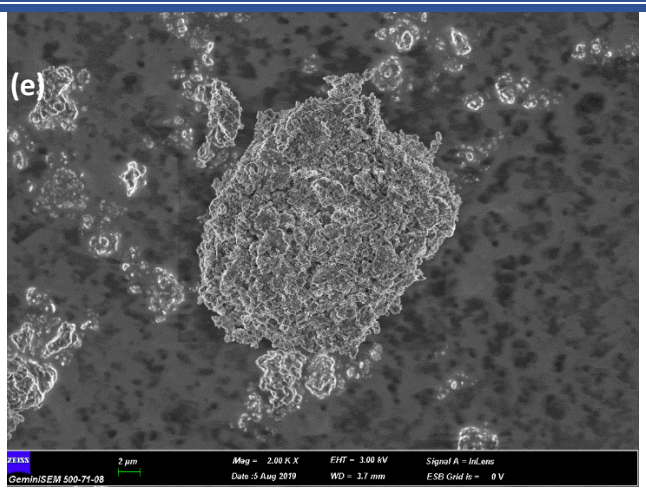

Figure 4. FESEM Images of Al, 5 % wt. Al_2O_3 and 10 % wt. ZrO_2 Powder Mixtures Milled for (a) 20, (b) 40, (c) 60, (d) 80 and (e) 100 Hours.

In Figure 4 (a), after 20 hours of ball milling process brittle Al_2O_3 and ZrO_2 particles broken can be observed, likewise Specimen A. As milling time increases from 20 to 40 hours, cold welding mechanism takes place instead of fracturing. At this step, particle size of the mixture is greater than Specimen A. After 60 hours of ball milling powder mixture gets flattened. It can also be seen that 60 hours milled powders start to break into pieces again. This result contributes to the general rule that explains during ball milling process fracturing and cold-welding mechanisms follow each other until the powder mixture reach a balance by means of particle size and shape. After 100 hours, Specimen B reaches a balance like Specimen A.

Figure 5 and Figure 6 illustrate microstructures of Specimen C and Specimen D powder mixtures (90 % wt. Al, 5 % wt. SiC and 5 % wt. ZrO_2 and 90 % wt. Al, 5 % wt. SiC and 10 % wt. ZrO_2) after various milling times, respectively.

By evaluating FESEM images of both powder mixtures, it can be easily deduced that at initial stages of the ball milling process brittle contents tend to fracture and broken particles are cold welded into the ductile Al particles. At further stages of milling, it is seen that the powder mixture break into small pieces. For both specimens milling time of 100 hours creates a homogeneous structure.

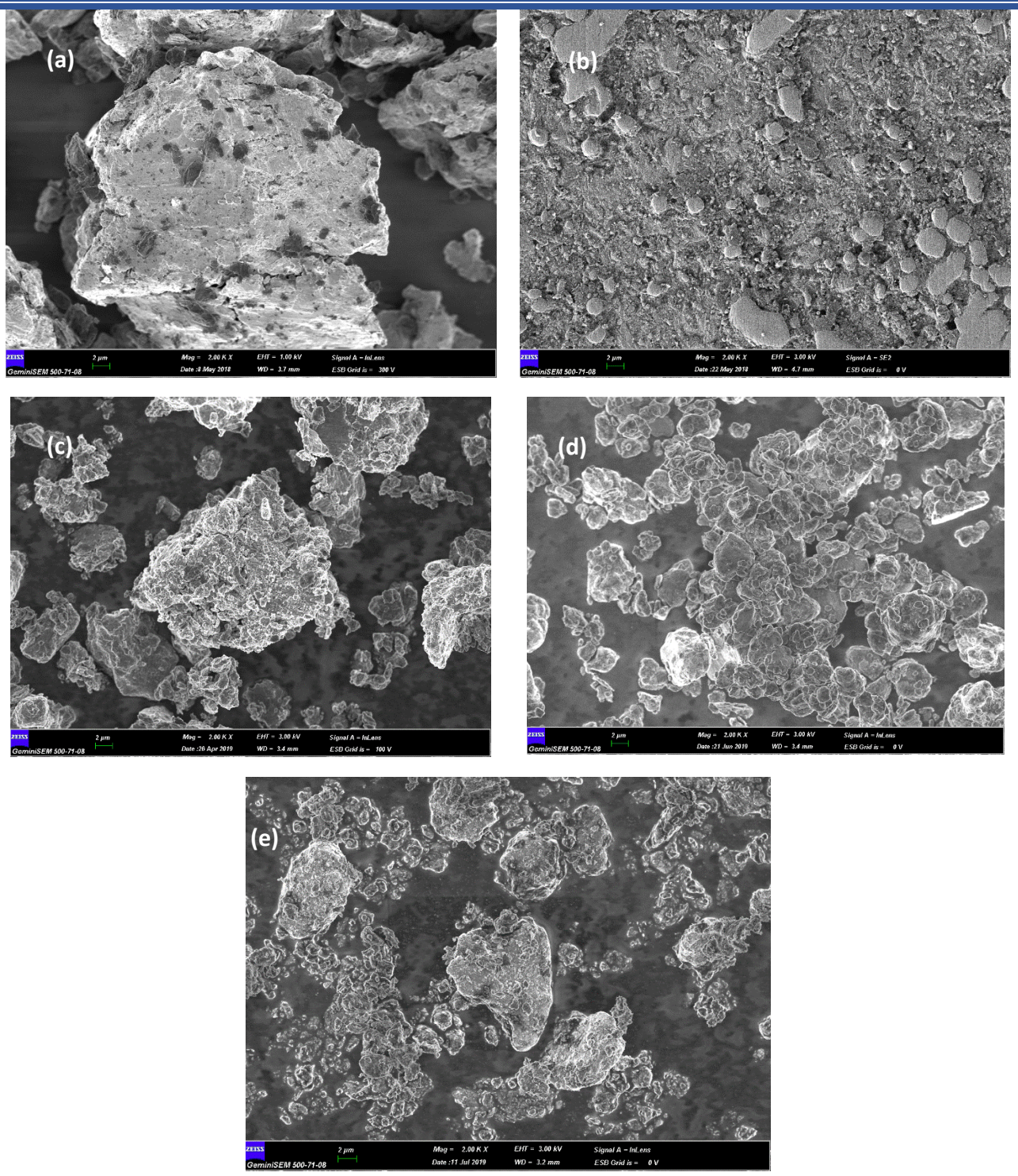

Figure 5. FESEM Images of Al, 5 % wt. SiC and 5 % wt. ZrO_2 Powder Mixtures Milled for (a) 20, (b) 40, (c) 60, (d) 80 and € 100 Hours.

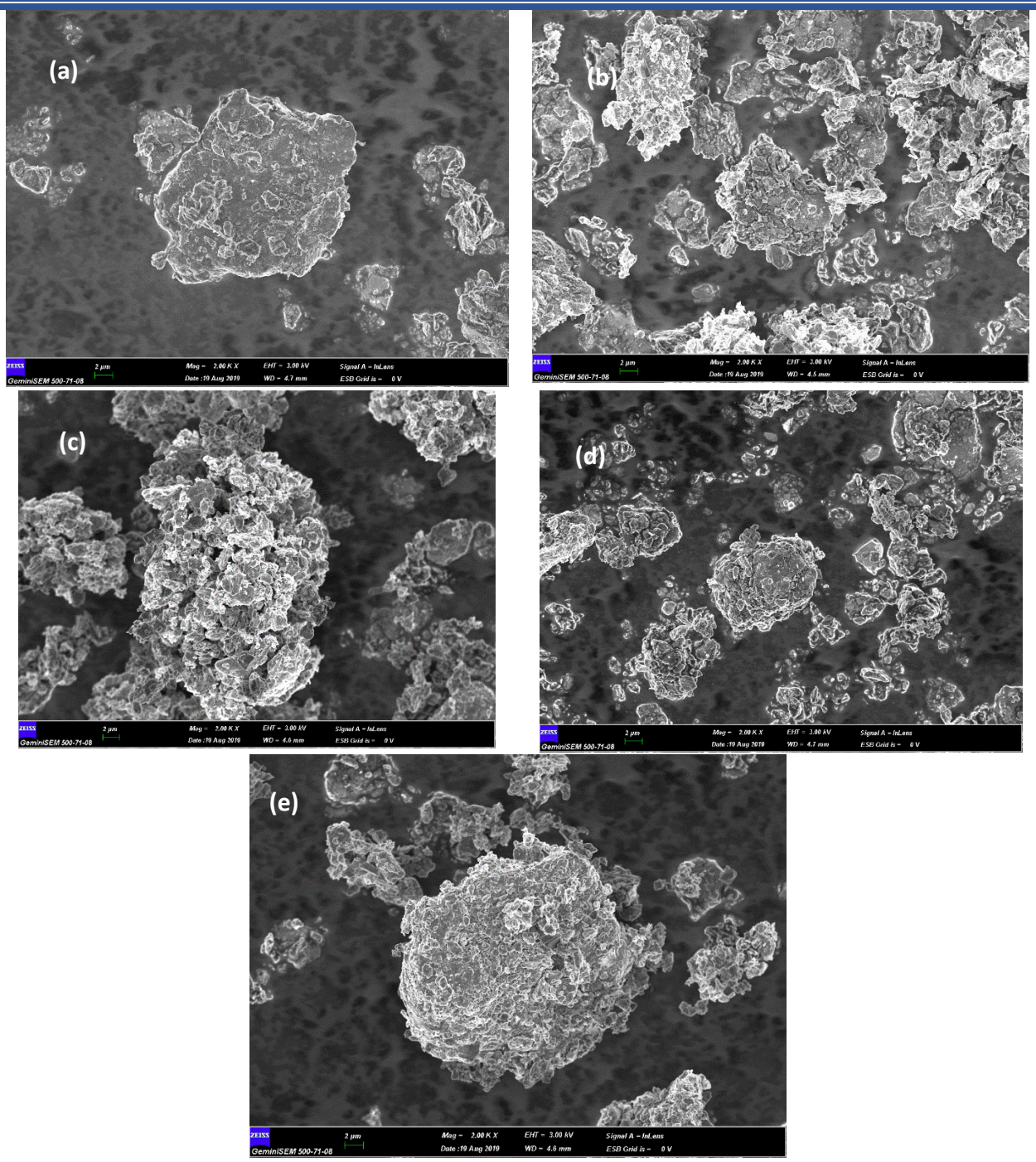

Figure 6. FESEM Images of Al, 5 % wt. SiC and 10 % wt. ZrO_2 Powder Mixtures Milled for (a) 20, (b) 40, (c) 60, (d) 80 and € 100 Hours.

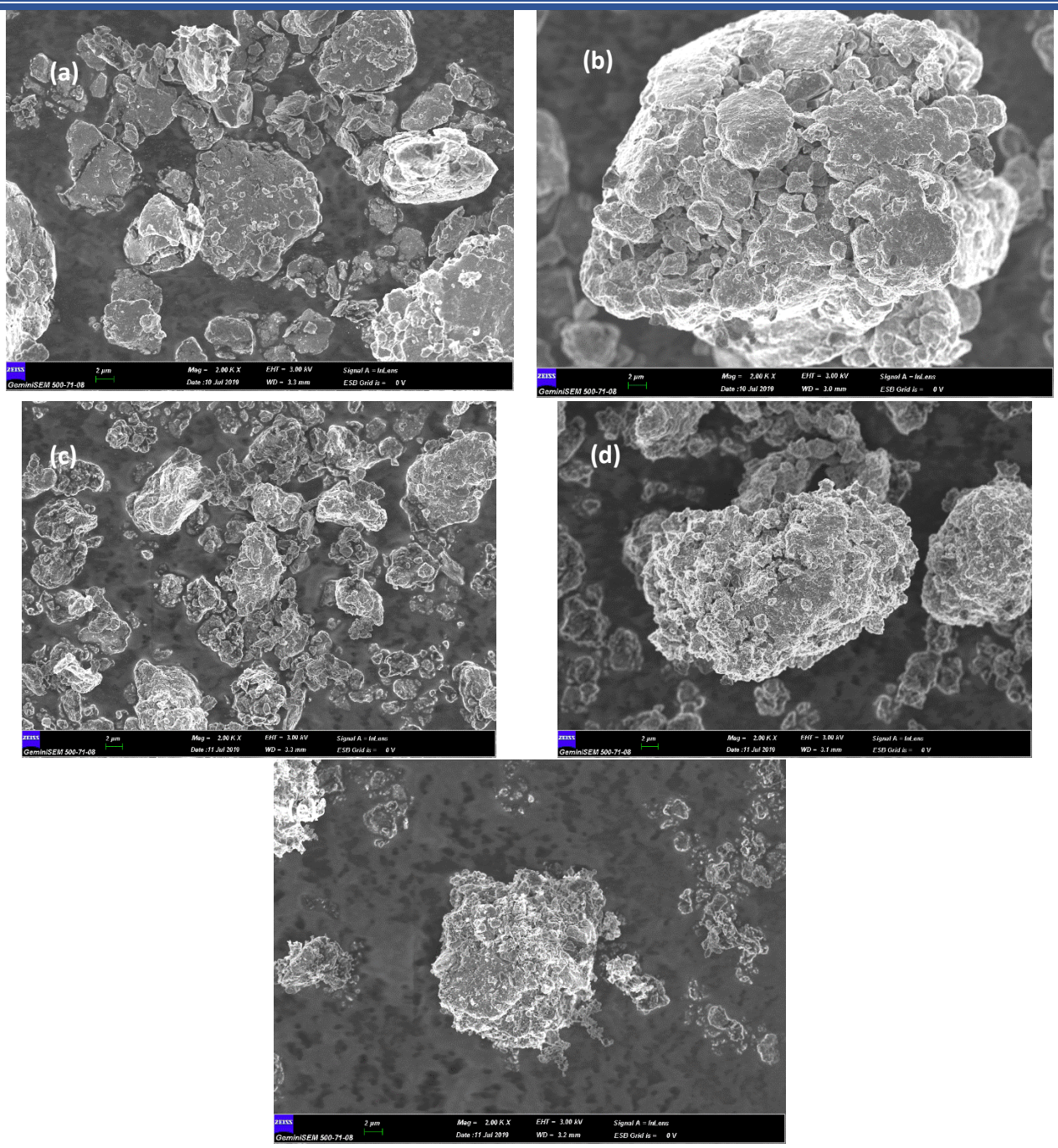

Figure 7. FESEM Images of Al, 5 % wt. B_4C and 5 % wt. ZrO_2 Powder Mixtures Milled for (a) 20, (b) 40, (c) 60, (d) 80 and (e) 100 Hours.

In Figure 7, morphological change in Al-5 % wt. B_4C and 5 % wt. ZrO_2 powder mixture can be seen. Like former powder mixtures, Specimen E that contains both 5 % wt. B_4C and ZrO_2 as brittle reinforcement,

tend to fracture at the first 20 hours period of milling. After 40 hours of milling, particles tend to come together and flatten. At this step a sponge-like structure can be observed (Figure 7.b). As the milling time reaches 100 hours a homogeneous microstructure by means of particle size and shape is achieved.

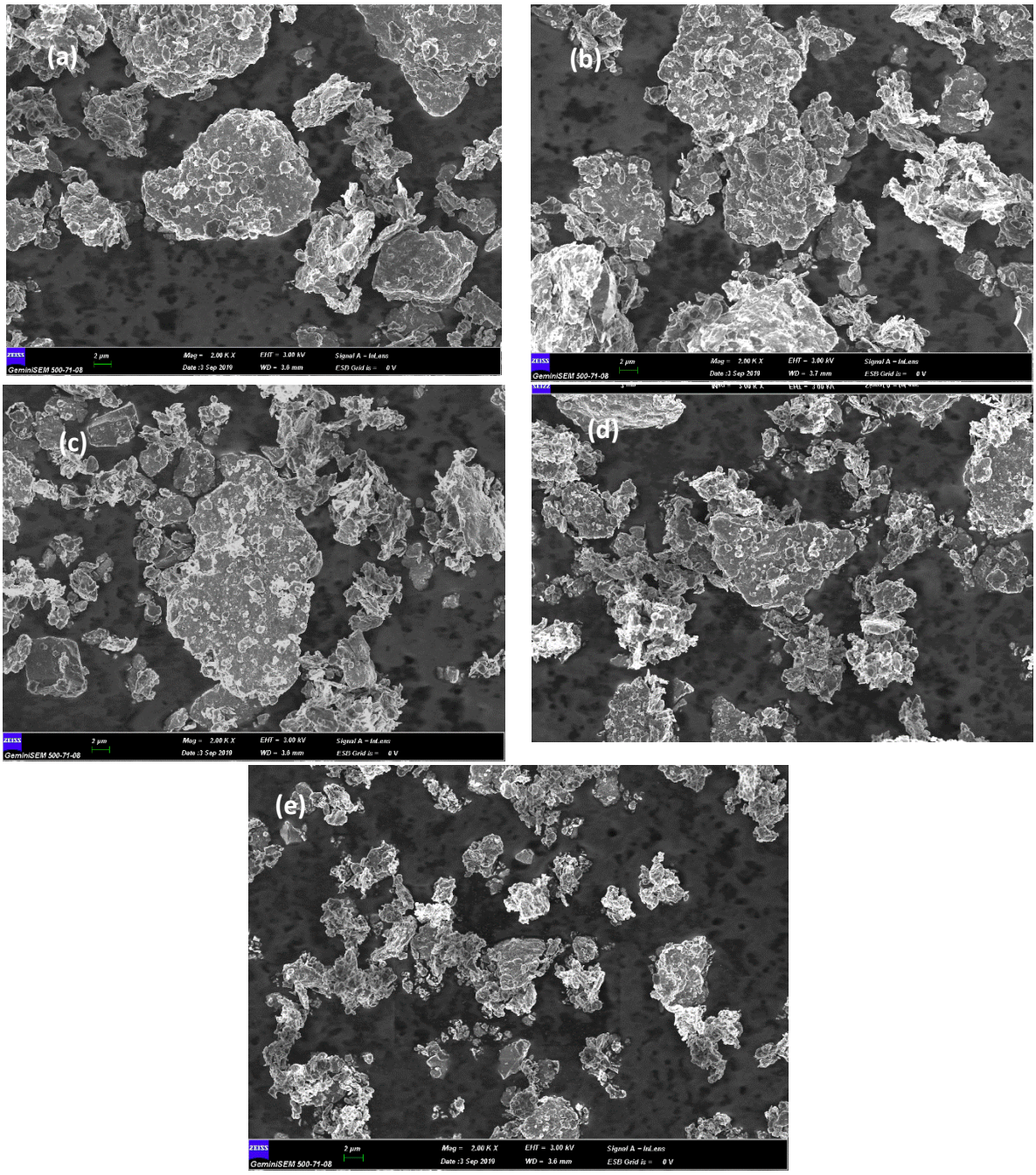

Figure 8. FESEM Images of Al, 5 % wt. B_4C and 10 % wt. ZrO_2 Powder Mixtures Milled for (a) 20, (b) 40, (c) 60, (d) 80 and (e) 100 Hours.

From Figure 8.a the brittle particles of B_4C and ZrO_2 which broke into small pieces and stuck on soft Al matrix can be clearly seen. After 40 hours of ball milling, particles come together and form bigger particles. As milling time increases from 40 hours to 60 hours particles of the mixture get bigger and flat. During the next 20 hours of milling fracturing mechanism again become effective and particles break into small pieces. However, the microstructure is not homogeneous at all.

Like former specimens 100 hours of ball milling process help to achieve a homogeneous morphology by means of particle size and shape.

3.2. Particle Size Analyzing Results

Figure 9 gives an example for particle size analyze by Image ProPlus.

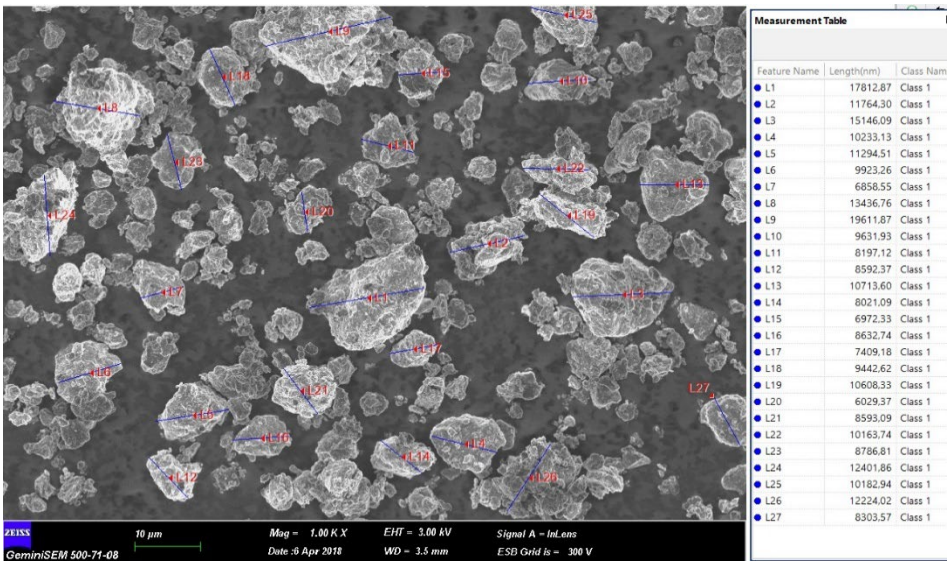

Figure 9. Average Particle Size Measuring by Image ProPlus.

Table 3 gives the change in particle size change of all specimens during milling time. And Figure 10 also summarizes particle size change of specimens graphically.

Table 3. Particle Size Change of Specimens versus Milling Time.

Specimen	Content	Milling Time (hrs)	Particle Size (µm)
Specimen A	Al-%5 Al_2O_3-%5 ZrO_2	20	58,56
		40	50,18
		60	21,32
		80	11,52
		100	10,41
Specimen B	Al-%5 Al_2O_3-%10 ZrO_2	20	53,01
		40	20,17
		60	20,09
		80	13,39
		100	9,96
Specimen C	Al-%5 SiC-%5 ZrO_2	20	27,05
		40	20,70
		60	12,18
		80	11,71
		100	7,80
Specimen D	Al-%5 SiC-%10 ZrO_2	20	26,67
		40	14,35
		60	11,67
		80	11,07
		100	7,94
Specimen E	Al-%5 B_4C-%5 ZrO_2	20	20,18
		40	20,06
		60	12,10
		80	11,85
		100	8,09
Specimen F	Al-%5 B_4C-%10 ZrO_2	20	19,49
		40	11,62
		60	12,37
		80	9,91
		100	2,32

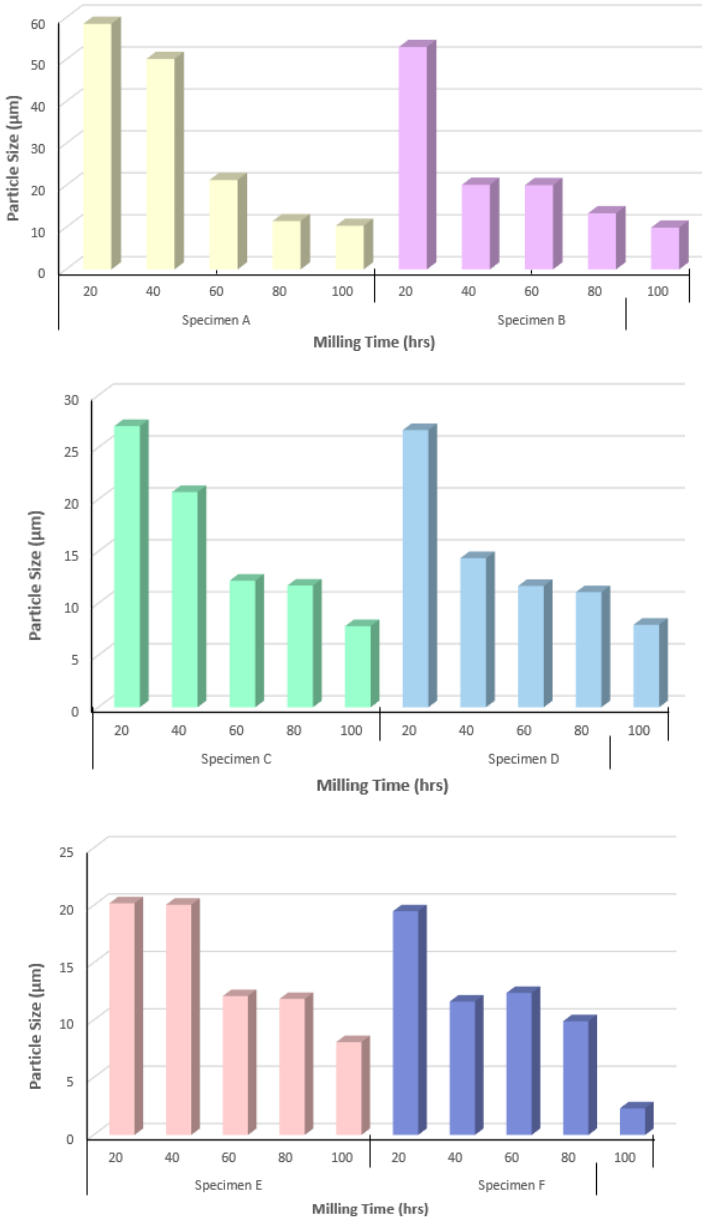

Figure 10. Particle Size Change of Powder Mixtures vs Milling Time.

From particle size analyzes and graphical abstract following results are achieved;

- As expected, for all specimens, particle size decreases by increasing milling time,
- After 100 hours of milling, final particle sizes of the composite powders are smaller than 10 µm,

- After 100 hours of milling, final particle sizes of specimens vary between 2,32-10,41 µm. That result due to the difference of initial particle sizes of the particles,
- After early stages of milling (20 hours) average particle size of the samples changes in a wide range between 19,49 –53,56 µm. That result may be due to the dominant cold welding mechanism at early stages of ball milling.
- For all powder mixtures, Besides Specimen F, particle size decreases significantly after the first 20 hours of milling. This is due to the increasing energy need to break the powders as the particle size decreases.
- As supported by the FESEM images, as milling goes further to 60 hours same trend still goes on. But at the progressive stages, -because a steady state is reached between cold welding and fracturing mechanisms- particle sizes of the specimens become steady. Thus, final particle sizes of the samples are more close to each other.
- The smallest particle size is achieved for Specimen F which consists of 5 % wt. B_4C and 10 % wt. ZrO_2 as reinforcement (Figure 11).
- The biggest particle size is determined for Specimen A. Because the biggest reinforcement particle size belongs to as received Al_2O_3,
- It can be said that increasing ZrO_2 content -accordingly increasing reinforcement powder wt.- decreases final particle size of the powder mixture. That's because ZrO_2 particles have the smallest particle size distrubition among all reinforcement powders.

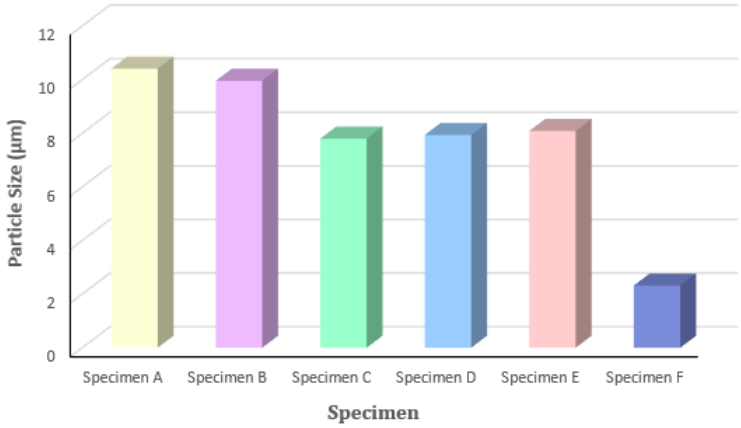

Figure 11. Particle Size of the Specimens After 100 Hours of Milling.

3.3. XRD Results

According to the XRD results, we can see 5 significant peaks for as-received pure Al. Those peaks which appear at 2θ angles 35,5 °, 44,8 °, 65,22 °, 78,32 ° and 82,62 ° refer to atomic planes (111), (200), (220), (311) and (222), respectively. Figure 12, shows XRD powder patterns of the specimens. Significant Al_2O_3 peaks that belong to atomic planes (012), (104), (110), (113), (024), (116), (214), (300) and (1010) [13] appear at diffraction angles of 25,54°, 35,14 °, 37,76°, 43,34°, 52,56°, 57,5°, 65,52°, 68,2° and 76,86 °. Additionally, XRD powder pattern of ZrO_2 refer to 4 main peaks at 2θ angles of 30,2° for (111) plane, 35,14° for (200) plane, 50,32° for (220) plane and 60,12° for (311) plane [14].

By considering XRD results of Specimen A (Al-5% Al_2O_3-5% ZrO_2) we can see that significant peaks belong to Al, as Al is the matrix and the dominant component by means of weight. After 20 hours of milling XRD results show 5 main peaks at 2θ angles of 30,12°, 38,4°, 44,6°, 65,12° and 78,08°. The peak that appears at diffraction angle of 30,12° belongs to ZrO_2 and exists to the end of the MA process by keeping its intensity nearly constant and diffraction angle increasing. Other Al peaks also appear at smaller 2θ values than as received Al. It can be said that the intensities of all peaks are also smaller than as received components. And after 40 hours of milling same trend goes on and no new peaks were observed. But 60 hours of MA process makes an Al_2O_3 peak which belongs to (104) plane appear for the first time at 35,26°. The 5th peak of as-received Al appears after 80 hours of milling.

Unlike Specimen A, Specimen B shows all main peaks of as received Al from the beginning of MA. Also, 3 significant peaks of ZrO_2 can be observed from the beginning. That's due to the increasing % wt ratio of ZrO_2 in the powder mixture. And the former Al_2O_3 peak that belongs to the (104) plane also exists in the diffraction pattern. It first appears at 35,21°

As received SiC has 10 main peaks of all sizes. The most significant peaks appear at 35,56 ° and 38,08 ° and they refer to the (0110) and (0111) atomic plane [13].

As Al is the most dominant component, like former, we can detect Al peaks clearly at the X-RD powder pattern of Specimen C. After 20 hours mechanical alloying, all of the 5 main Al peaks are clear on the graph. Additionally, one peak for ZrO_2 (at 2θ=49,73°) and two SiC peaks (at 2θ=35,21°, 2θ=70,16 °) exist in the

structure. Same peaks can be observed to the end of the MA process. Additionally, after 100 hours of alloying we can see (111) peak of ZrO_2.

XRD powder pattern of the 20-hour mechanical alloyed Al-5% wt. SiC-10% wt. ZrO_2 mixture shows 9 main peaks. The graph points all 5 main peaks of Al. And also due to the increasing ZrO_2 content number of ZrO_2 peaks detected from the beginning also increases. Same peaks preserve their existence to the end of the mechanical alloying process.

XRD pattern of the initial B_4C figures 17 main peaks appearing at 2θ angles varying between 19,62° to 80,74°. The most intensive three peaks which appear at diffraction angles 37,76°, 34,92° and 23,42° refer to atomic planes (021), (104) and (012) atomic planes, respectively.

Specimen E, after 20 hours of mechanical alloying, shows 6 main peaks. 5 of these peaks are typical Al peaks and can be seen at lower 2θ values than as-received Al. The 6th peak belongs to (111) plane of ZrO_2 and can be detected at 2θ=30,19°. Same five peaks can be seen after 40 hours of ball milling. Additionally, (222) peak of ZrO_2 appears at a diffraction angle of 35,68°. Hereupon mentioned peaks remain their existence to the end of mechanical alloying and (110) peak of B_4C appears after 40 hours.

Similar to former Specimen F shows 5 main peaks of Al as the matrix material. All of those peaks appear at 2θ angles lower than the neat Al. Additionally, we can see all of the peaks of ZrO_2 from the beginning of the MA process -from 20 hours to 100 hours-. That is due to the increasing ZrO_2 content of the specimen.

Eventually, for all powder mixtures, it can be clearly said that MA process causes all peaks to broaden. This result is contributed to the common knowledge that mechanical alloying process forces atomic planes to get closer by the effect of impact caused by ball-vial-ball collisions.

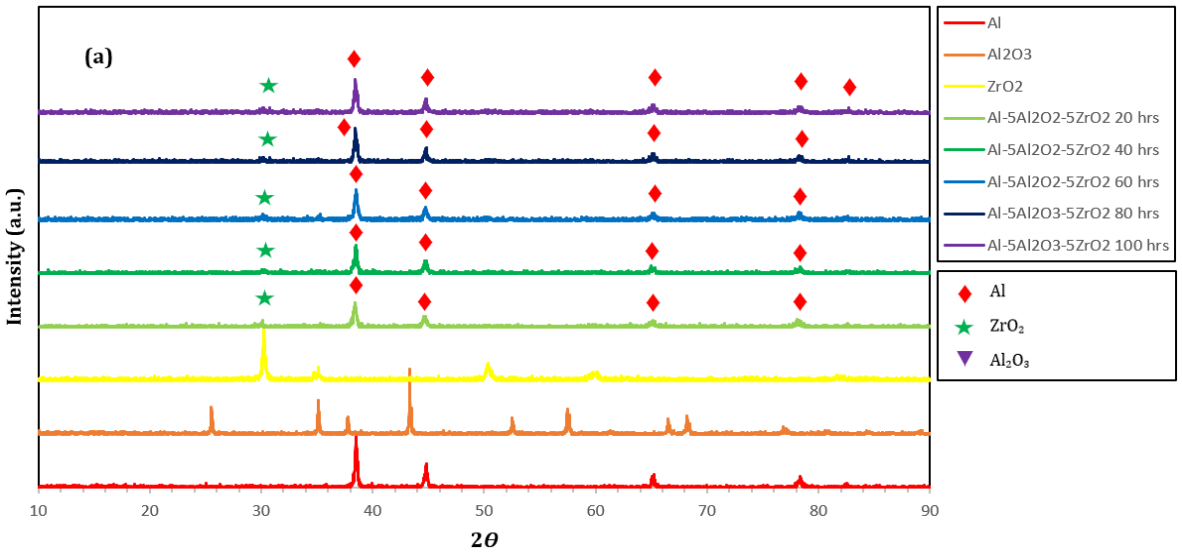
(a)
Intensity (a.u.)
2θ
10
20
30
40
50
60
70
80
90
Al
Al2O3
ZrO2
Al-5Al2O2-5ZrO2 20 hrs
Al-5Al2O2-5ZrO2 40 hrs
Al-5Al2O2-5ZrO2 60 hrs
Al-5Al2O3-5ZrO2 80 hrs
Al-5Al2O3-5ZrO2 100 hrs
Al
ZrO2
Al2O3

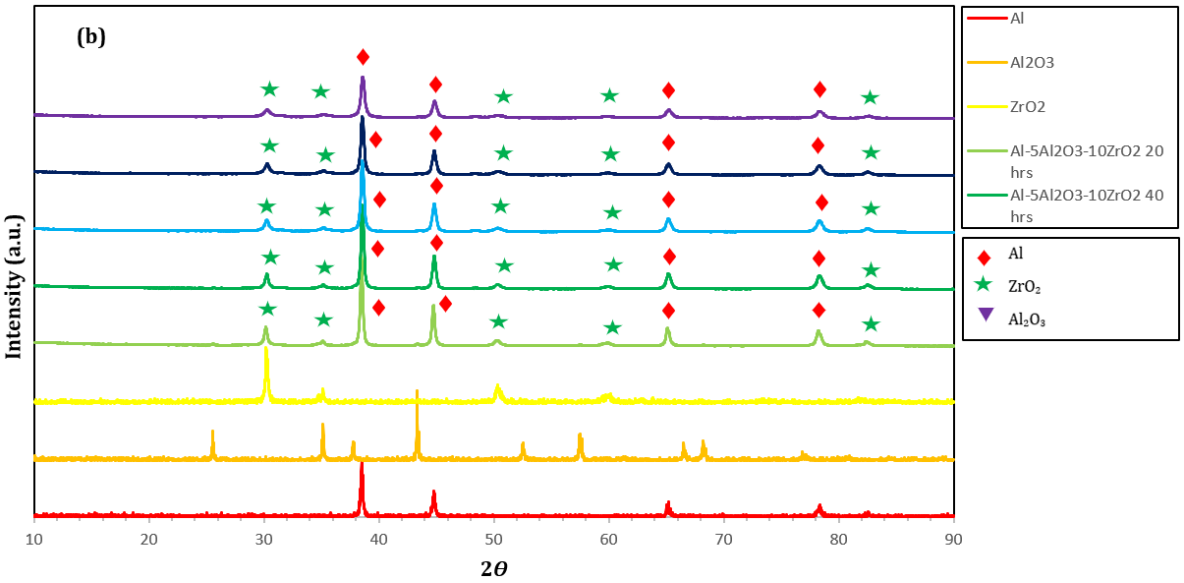
(b)
Intensity (a.u.)
2θ
10
20
30
40
50
60
70
80
90
Al
Al2O3
ZrO2
Al-5Al2O3-10ZrO2 20 hrs
Al-5Al2O3-10ZrO2 40 hrs
Al
ZrO2
Al2O3

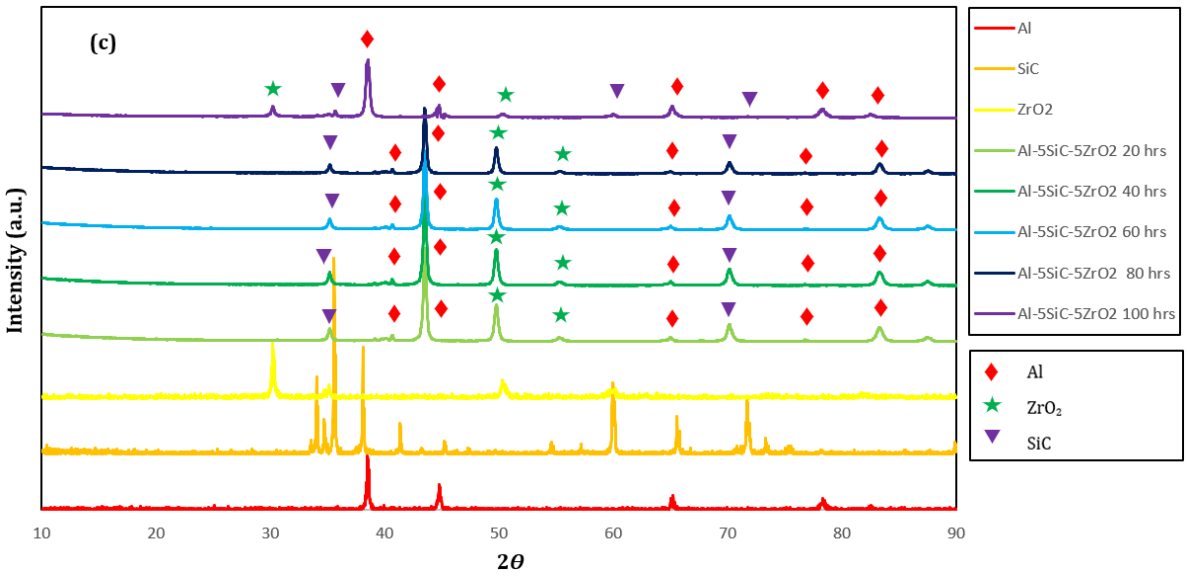
(c)
Intensity (a.u.)
2θ
10
20
30
40
50
60
70
80
90
Al
SiC
ZrO2
Al-5SiC-5ZrO2 20 hrs
Al-5SiC-5ZrO2 40 hrs
Al-5SiC-5ZrO2 60 hrs
Al-5SiC-5ZrO2 80 hrs
Al-5SiC-5ZrO2 100 hrs
Al
ZrO2
SiC

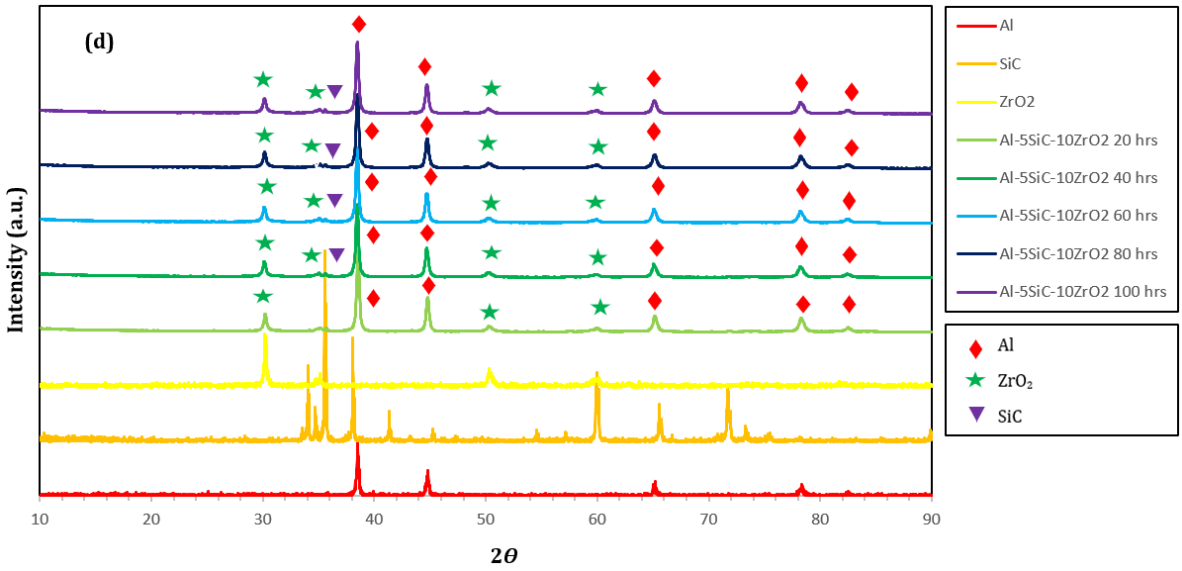
(d)
Intensity (a.u.)
2θ
10
20
30
40
50
60
70
80
90
Al
SiC
ZrO2
Al-5SiC-10ZrO2 20 hrs
Al-5SiC-10ZrO2 40 hrs
Al-5SiC-10ZrO2 60 hrs
Al-5SiC-10ZrO2 80 hrs
Al-5SiC-10ZrO2 100 hrs
Al
ZrO2
SiC

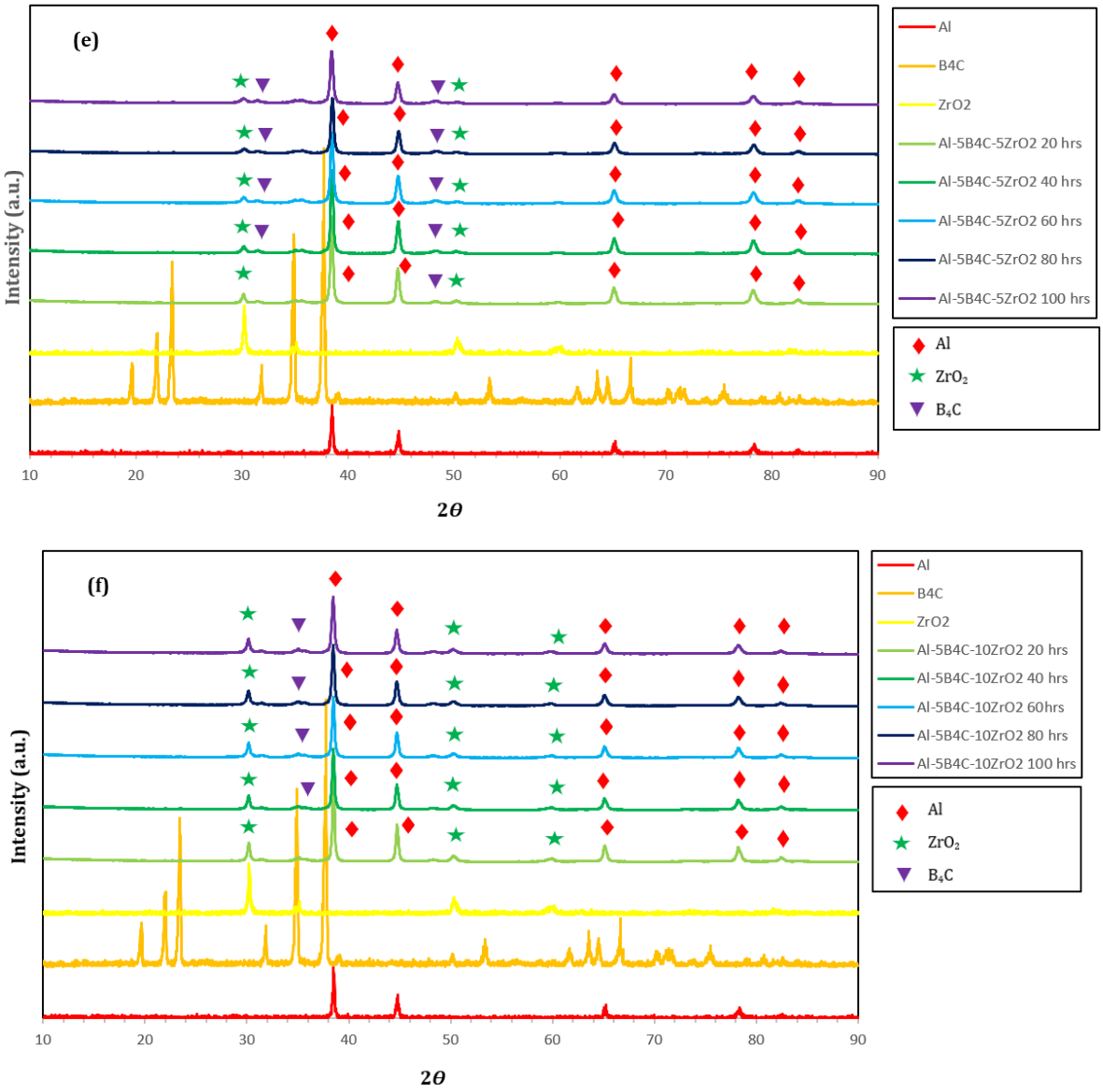

Figure 12. XRD Results of (a) Specimen A, (b) Specimen B, (c) Specimen C, (d) Specimen D, (e) Specimen E and (f) Specimen F.

4. CONCLUSION

As a result of the studies, we can sum up;

- 100 hours of mechanical alloying makes composite powder structure fine and homogeneous,
- Particle size decreases by increasing milling time and final particle sizes of the composite powders are smaller than 10 µm,
- For most powder mixtures particle size decreases significantly after the first 20 hours of milling,

- The smallest particle size is achieved for Specimen F and The biggest particle size is determined for Specimen A after 100 hours,
- XRD results indicate mostly Al peaks because as Al is the matrix and the dominant component by means of weight,
- Specimens with higher (10 % wt. ZrO_2) show more peaks of Al because of increasing ZrO_2 content,
- For all powder mixtures, MA process causes all peaks to broaden.

Due to these results the authors advice some important points for further studies;

- In order to achieve a finer particle distribution mechanical alloying time can be increased and effect of alloying time can be studied detailly.
- By considering that the ZrO_2 increases fracture toughness, conducting impact tests on cold pressed and sintered specimens after mechanical alloying is advised for further studies.

ACKNOWLEDGEMENTS

This research was supported by Erciyes University Scientific Research Projects Unit (EU-BAP) with the project number FBA-2018-8474. The authors are also grateful to Erciyes University Technology Research and Application Center (TAUM) and Erciyes University Nanotechnology Research Center (ERNAM) for their contribution during characterization of the powder mixtures.

REFERENCES

[1] Arik, H., 2008. Effect of mechanical alloying process on mechanical properties of a-Si_3N_4 reinforced aluminum-based composite materials. Materials & Design, 29 (9): 1856-1861.

[2] Kostka A., Lelatko J., Gigla M., Moraviec H., Janas A., 2003. TEM study of the interface in ceramic-reinforced aluminum-based composites. Materials Chemistry and Physics 81:323–325.

[3] Nie, C., Gu, J., Liu, J., Zhang D., 2008. Investigation on microstructures and interface character of B_4C particles reinforced 2024Al matrix composites fabricated by mechanical alloying. Journal of Alloys and Compounds, 454 (1-2): 118-122.

[4] Monazzah A.H., Simchi A., Relhani S.M.S., 2010. Creep behavior of hot extruded Al-Al_2O_3 nanocomposite powder. Materials Science and Engineering A, 572:2567-2571.

[5] El-Eskandarany, M.S., 1998. Mechanical solid state mixing for synthesizing of SiCp/Al nanocomposites. Journal Of Alloys and Compounds, 279: 263-271.

[6] Prabhu B., Suryanarayana C., An L., Vaidyanathan R., 2006. Synthesis and characterization of high volume fraction Al-Al_20_3 nanocomosite powders by high-energy milling. Materials Science and Engineering A, 425:192-200.

[7] Wang, J., 2008. Mechanical alloying of amorphous Al–SiO_2 powders. Journal of Alloys and Compounds, 456 (1-2): 139-142.

[8] Topcu, I., Gulsoy, H.O., Kadioglu, N., Gulluoglu, A.N., 2009. Processing and mechanical properties of B_4C reinforced Al matrix composites. Journal of Alloys and Compounds, 482 (1-2): 516-521.

[9] Suryanarayana, C. 2001. Mechanical alloying and milling. Progress in Materials Science, 46:1-184.

[10] Suryanarayana, C., 2008. Recent developments in mechanical alloying. Reviews on Advanced Materials Science, 18:203-211.

[11] M. Sherif El-Eskandarany, Mechanical Alloying for Fabrication of Advanced Engineering Materials. Noyes Publications, 2001.

[12] Benjamin, J.S., 1992. Fundamentals of Mechanical Alloying. Materials Science Forum 88-90: 1-18.

[13] Dagasan, E., 2014. Production and Characterization of Alumium Matrix Ceramic Reinforced Sub-Micron Composites by Mechanical Alloying. Erciyes University, Graduate School of Natural and Applied Sciences, PhD Thesis, Kayseri.

[14] Ramirez, L., Mecartney, M.L., Krumdieck, S.P., 2008. Nanocrystalline ZrO_2 thin films on silicon fabricated by pulsed-pressure metalorganic chemical vapor deposition (PP-MOCVD). Journal of Materials Research 23(08):2202 – 2211.

2nd International Natural Science, Engineering and Material Technologies Conference
Sep 15-17, 2022, İğneada-Kırklareli / TÜRKİYE

PREDICTION OF SOFTWARE FAULTS WITH BILSTM DEEP LEARNING MODEL

T. B. Alakus

Department of Software Engineering, Faculty of Engineering, Kırklareli University, Kırklareli, TÜRKİYE

E-mail: talhaburakalakus@klu.edu.tr

Abstract

In the technology industry and software sector, the detection of software faults is of great importance and plays a role in the effectiveness of the software. In the methods performed with traditional approaches, past experiences or various programs are used to identify software faults. This causes the process to be slow and, in many cases, the late delivery of the software to the end user. For these reasons, the importance of autonomous applications using artificial intelligence has increased. Such applications enable the software to work more effectively and are both time and cost efficient by minimizing errors. In this study, software faults were predicted using deep learning model and faults were classified using various features. The study consisted of four different stages: obtaining data, pre-processing the data, classifying the data, and evaluating the classification results. Three different data sets, JM1, PC1 and CM1, were used and classified in the study. BiLSTM was used in the classification process and the performance of the classifier was determined by accuracy, F1-score, and AUC score. While 82.00% accuracy was obtained in the prediction process made with the CM1 data set, a 0.7 AUC score was calculated. In the JM1 dataset, the accuracy and AUC score were 80.66% and 0.6, respectively. The most successful classification process was obtained with the PC1 dataset. In the classification process using this data set, an accuracy score of 91.89% was obtained, while a 0.84 AUC score was calculated. In line with the results obtained, it has been seen that the deep learning model used performs an adequate classification process.

Keywords: Deep learning, Software faults, Artificial intelligence, Software engineering, Fault prediction

1. INTRODUCTION

Software quality assurance is expressed as a series of activities and processes performed to ensure that a final product is of the desired quality. Software quality assurance not only detects errors and defects, but also tries to prevent them. For this, it carries out a series of activities such as providing a suitable development environment, defining the processes and procedures to be followed, defining how the effectiveness of processes and procedures will be measured and improved [1]. In addition, it uses verification and validation to detect software errors. Software errors refer to errors that occur at any stage of the software development process. Quickly responding to errors is effective in preventing errors from affecting users or others. In addition, the correct management of the errors can reduce the number of faults. Software errors are divided into three categories. These are syntax errors, runtime errors, and logical errors. Syntax errors are among the errors that can be encountered due to the presence of some expressions in the coding program that are against the rules of the programming language. Fixing such errors is quite simple. Runtime errors occur during program execution. For runtime errors, the error message is generally given using the language of the running operating system. It is very difficult to predict where and how runtime errors will occur. Logical errors are among the most dangerous errors that can be encountered during software [2]. These errors are due to some misconceptions in programming logic. It occurs during the testing of the software or its use by end users. To solve the logical errors, it is necessary to go back to the analysis stage. Finding out where logical errors originate is sometimes more difficult than ever to predict. Code audits, software tests and code explanations are generally used to identify and fix software errors and faults [3]. However, since these methods are based on the experience of the people who will find the fault, the process usually takes time and is costly [4]. For this reason, software fault prediction is also used in the software quality assurance process today. Software fault prediction is an economical and resource-optimal method based on predicting the fault proneness of software modules [5]. The potential of software fault prediction studies to identify faulty software modules early in the software development lifecycle is of great interest today. In previous prediction studies, mostly fault proneness of software modules was estimated and various classification algorithms were used for this. The results obtained from these studies have shown that the potentials of the algorithms are limited, and their reliability is questioned [6]. Therefore, researchers have begun to classify software faults rather than the fault proneness of software modules [7]. Artificial intelligence algorithms are used for software fault prediction and both machine learning and deep learning are applied. In this study, BiLSTM (Bidirectional Long/Short Term

Memory), one of the deep learning algorithms, was used and software faults were predicted. The study consists of four stages. In the first stage, data were obtained, and three different data sets were used in this direction. Then, the data were normalized, and the Z-score method was used for this purpose. In the next stage, the classification process was performed, and the results of the classifier were evaluated. In the last stage, the performance of the classifier was measured by accuracy, F1-score, and AUC scores.

The remainder of the study is organized as follows. In the second section, related works were examined. In the third section, information about the data set and classifier is given. In the fourth section, classification results are provided, analysed, and discussed. In the last section, the results of the study are given, and future studies are mentioned.

2. RELATED WORKS

In this part of the study, some of the studies carried out in the literature were examined. The data sets used in these studies and the classification results obtained are mentioned. In the study [4], researchers classified and predicted software faults with various machine learning algorithms. Three different data sets, JM1, CM1 and PC1, were used in the study and these data sets were analysed separately. The data were obtained from the PROMISE Software Engineering Repository. After the data were obtained, feature extraction was performed and for this purpose covariance analysis, minimum-maximum normalization, rescaling, PCA (Principal Component Analysis) were used. After feature extraction, classification was performed and DT (Decision Tree), NB (Naive Bayes), SVM (Support Vector Machines), RF (Random Forest), KNN (K Nearest Neighbour) and LR (Logistic Regression) classifiers were used. The performances of the classifiers were determined by precision, recall, accuracy, and F1-score. The highest accuracy score for the JM1 dataset was obtained with DT, SVM, RF and KNN and the score was calculated as 99%. In the CM1 dataset, 100% accuracy was obtained with DT, NB, SVM and RF algorithms. When classifying the data of the PC1 data set, the highest accuracy score of 99% was obtained with DT, SVM and RF algorithms. In the study [8], the researcher used various machine learning algorithms to predict software faults and compared them. Two different data sets, AR1 and AR6, were used in the study. After the data sets were obtained, feature extraction was performed and various statistical features such as minimum value, maximum value, mean value and standard deviation were used. In the classification stage, seven different methods were used, namely LR, SVM, DT, ANN (Artificial Neural Networks), CCN (Cascade Correlation Network), GMDH (Group Method

of Data Handling Polynomial Method) and GEP (Gene Expression Programming). The performance of the classifiers was determined by precision, recall and AUC scores. While the highest AUC score for AR1 dataset was obtained with DT classifier with 0.865, the highest AUC score in AR6 dataset was obtained with DT again and the result was 0.948. In the study [9], researchers predicted software faults and efforts using various data mining approaches. A total of seven different data sets, KC1, PC3, PC4 and four different Android data sets, were used in the study. C4.5 and RT (Regression Tree) were used for classification. To measure the performance of the classifiers, fidely, accuracy and recall evaluation metrics were used. While an average accuracy of 86.06% was obtained with the C4.5, this rate was 88.20% with the RT. In the study [10], the researchers predicted the software faults using deep learning methods. Four different data sets, CM1, KC1, KC2 and PC1, were used in the study. The data obtained from these data sets were then normalized and made ready for classification. MLP (Multi Layer Perceptron) and CNN (Convolutional Neural Networks) algorithms were used in the classification step. The performances of the classifiers were measured by the accuracy evaluation criterion. In the classification process with PC1 dataset, the highest accuracy score was obtained with CNN and the result was 97.8%. In the KC1 dataset, the most successful classification process was obtained with CNN and the accuracy score was calculated as 99.6%. The results did not change in the KC2 and CM1 data sets, and the most successful classification was done with CNN. With this algorithm, accuracy scores of 99.3% and 97.3% were obtained, respectively. In the study [11], the researchers developed a hybrid model and predicted software faults. Four different data sets were used in the study and these data sets are PC1, JM1, KC1 and KC3 data sets. Then the data were normalized, and minimum-maximum normalization was used for this process. After the normalization stage, a hybrid model including ANN and PSO (Particle Swarm Optimization) was designed, and the data were classified. The performance of the hybrid model was determined only by the accuracy score. While an accuracy score of 90.08% was obtained in the classification process of the data of the PC1 dataset, this score decreased to 86.06% in the data of the JM1 dataset. While the accuracy score was 92.03% in the KC1 dataset, it was 89.13% in the KC3 dataset.

The results obtained from these studies have shown that deep learning and machine learning can be applied in these areas.

3. MATERIAL AND METHODS

3.1. Dataset

The datasets used in this study were obtained from the PROMISE Software Engineering Repository [12]. Three different data sets were used in the study. These datasets are CM1, JM1 and PC1 datasets. There are 21 features in total in each data set. These attributes are numeric count, branch count, cyclomatic complexity, design complexity, essential complexity, Halstead blank line count, Halstead comments count, Halstead difficulty, Halstead effort, Halstead intelligence, Halstead line count, Halstead operands and operators, Halstead program length, Halstead time estimator, Halstead volume, IO code and comments, line of code, total operands, total operators, unique operands, and unique operators.

In addition, while there are 498 data in total in the CM1 data set, there are 1,109 data in total in the PC1 data set. The most data is in the JM1 data set, and this data set consists of 10,885 data in total.

3.2. Deep Learning Model

Deep learning is a sub-branch of machine learning that provides the opportunity to work with multidimensional data in multi-layered architectures using artificial neural network algorithms. Deep learning algorithms have a very important role in software engineering. In recent years, deep learning has begun to achieve significantly higher performance in real-world problems and have attracted the attention of researchers. Deep learning is nowadays used in bioinformatics [13, 14], object detection [15, 16], natural language processing [17, 18], emotion prediction [19, 20], disease detection [21, 22] etc., and significant successes are achieved. In this study, the BiLSTM model, which is one of the deep learning methods, was used. BiLSTM is a model that processes any neural network bidirectionally (both forward and backward). In the BiLSTM model, the inputs flow in two directions. This reveals the difference of this architecture from the LSTM. In the LSTM model, the input only moves in one direction, either forwards or backwards. However, in BiLSTM, both past and future information is retained as the input moves in both directions. This makes the BiLSTM model more effective than the LSTM model [23]. The fact that the BiLSTM deep learning model is more effective and deep learning algorithms are effective in software fault prediction studies has led to the use of this approach in this study. The parameters of the designed BiLSTM model are given below:

- In the input layer, values of 498 * 21 for the CM1 dataset, 1,109 * 21 for the PC1 data set and 10,885 * 21 for the JM1 data set are used.
- In the first layer, 256 units of BiLSTM were used and the activation function of this layer was determined as ReLU (Rectified Linear Unit).
- Then the data was made flattened.
- In the next step, batch normalization was performed.
- After the batch normalization step, 20% of the data was forgotten and memorization of the model was prevented.
- Two fully connected layers were used, and the neurons of these layers were 512 and 256, respectively.
- In the last layer, classification was made, and the activation function was determined as Softmax.
- To validate the model, the training and test datasets were split and 80% of the data was trained, while the rest was used for testing.
- The Adam function is used for optimization.
- The training process was carried out with 250 epochs.
- The parameters were determined by trial-and-error approach.

The flow chart of the proposed study is given in Figure 1.

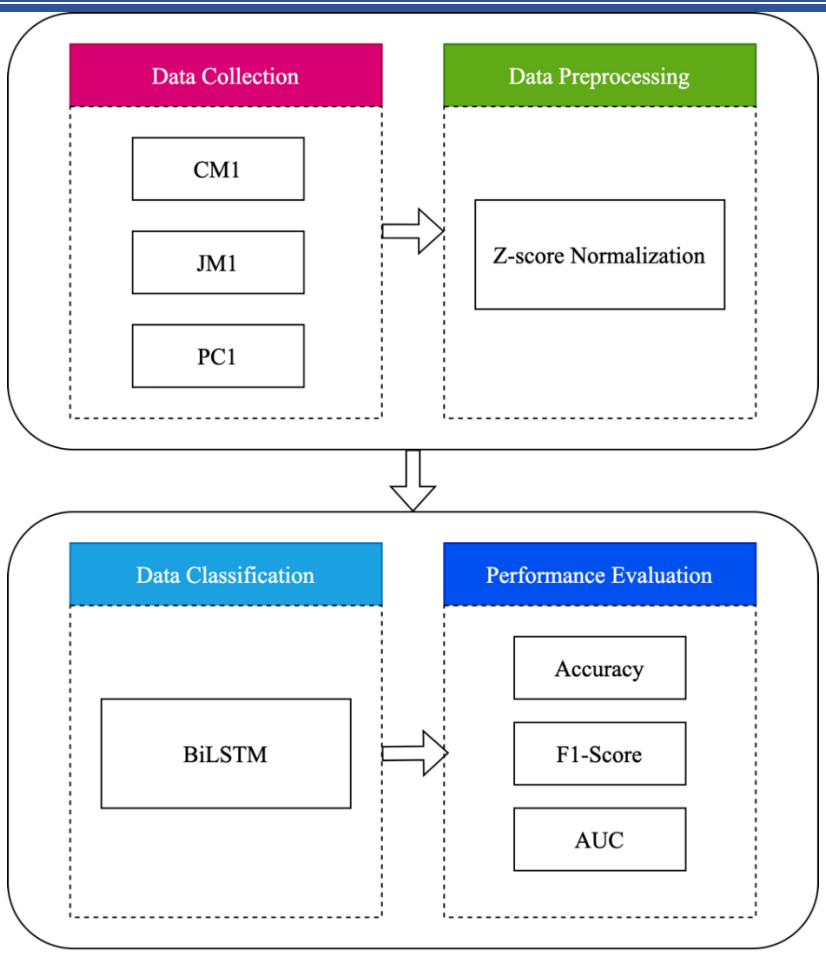

Figure 1. Flow chart of the study.

4. APPLICATION RESULTS AND DISCUSSION

In this study, software faults are classified and predicted. In this direction, the BiLSTM deep learning model was used, and the performance of the classifier was determined by accuracy, F1-score, and AUC scores. Classification results are given in Table 1.

Table 1. Application results

Dataset	Accuracy	F1-Score	AUC
CM1	82.00%	17.00%	0.70
JM1	80.66%	33.00%	0.60
PC1	91.89%	49.82%	0.84

When the results in Table 1 were examined, it was seen that the most effective classification process was performed with the PC1 data set. While the accuracy score obtained with the PC1 dataset was 91.89%, the AUC score was 0.84. Then, the most successful classification process was obtained with the CM1 data set, while 82.00% accuracy was observed with this data set, the AUC score was 0.70. The most ineffective classification process was seen in the JM1 dataset. The accuracy score in the classification performed with JM1 was 80.66%. The AUC score of this data set was calculated as 0.60. When the results are analysed according to the accuracy scores, it is seen that the designed classifier classifies the JM1, CM1 and PC1 data sets effectively. Figure 2 shows the ROC curves of the data sets. In Figure 3, the confusion matrices of the data sets are given.

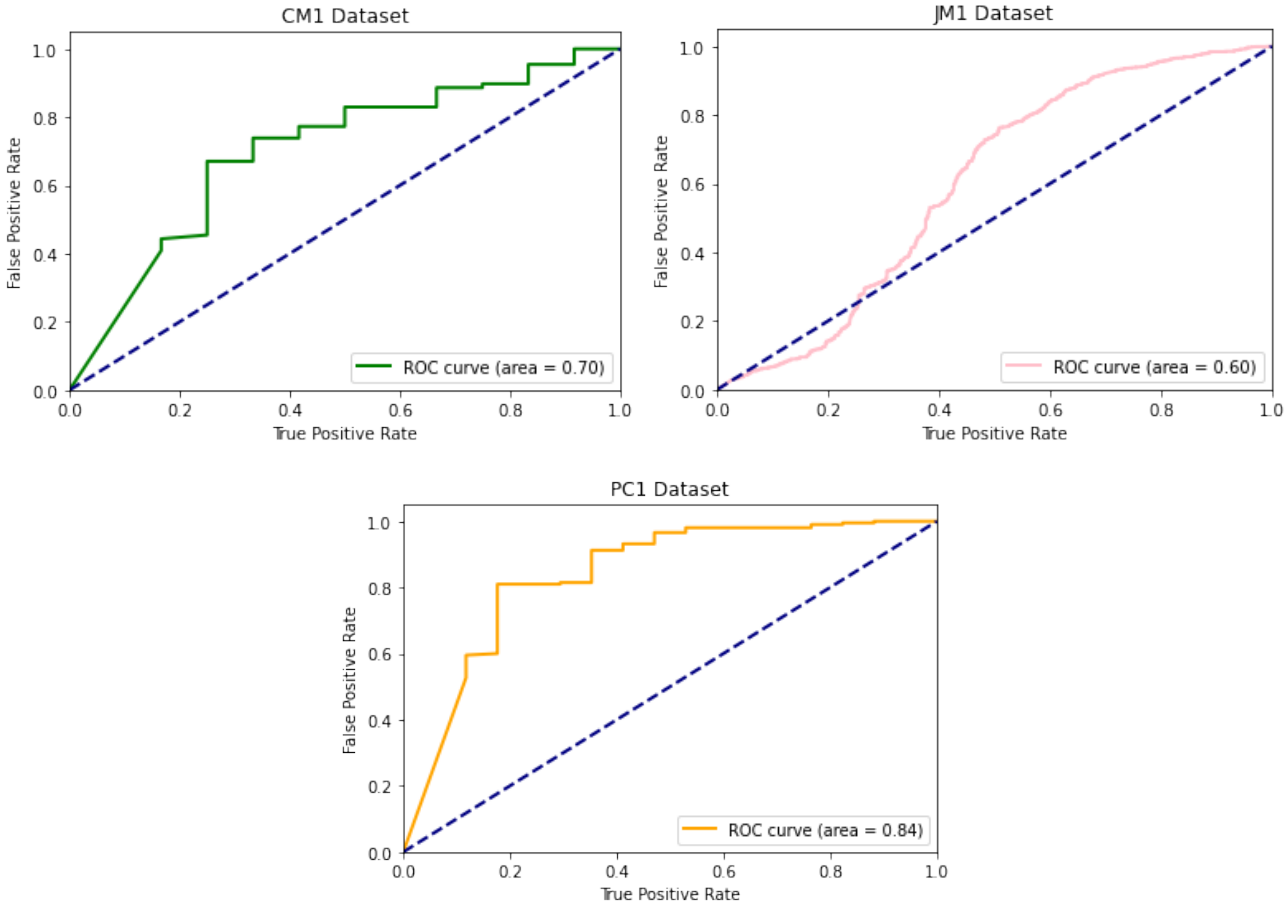

Figure 2. ROC curve for each dataset.

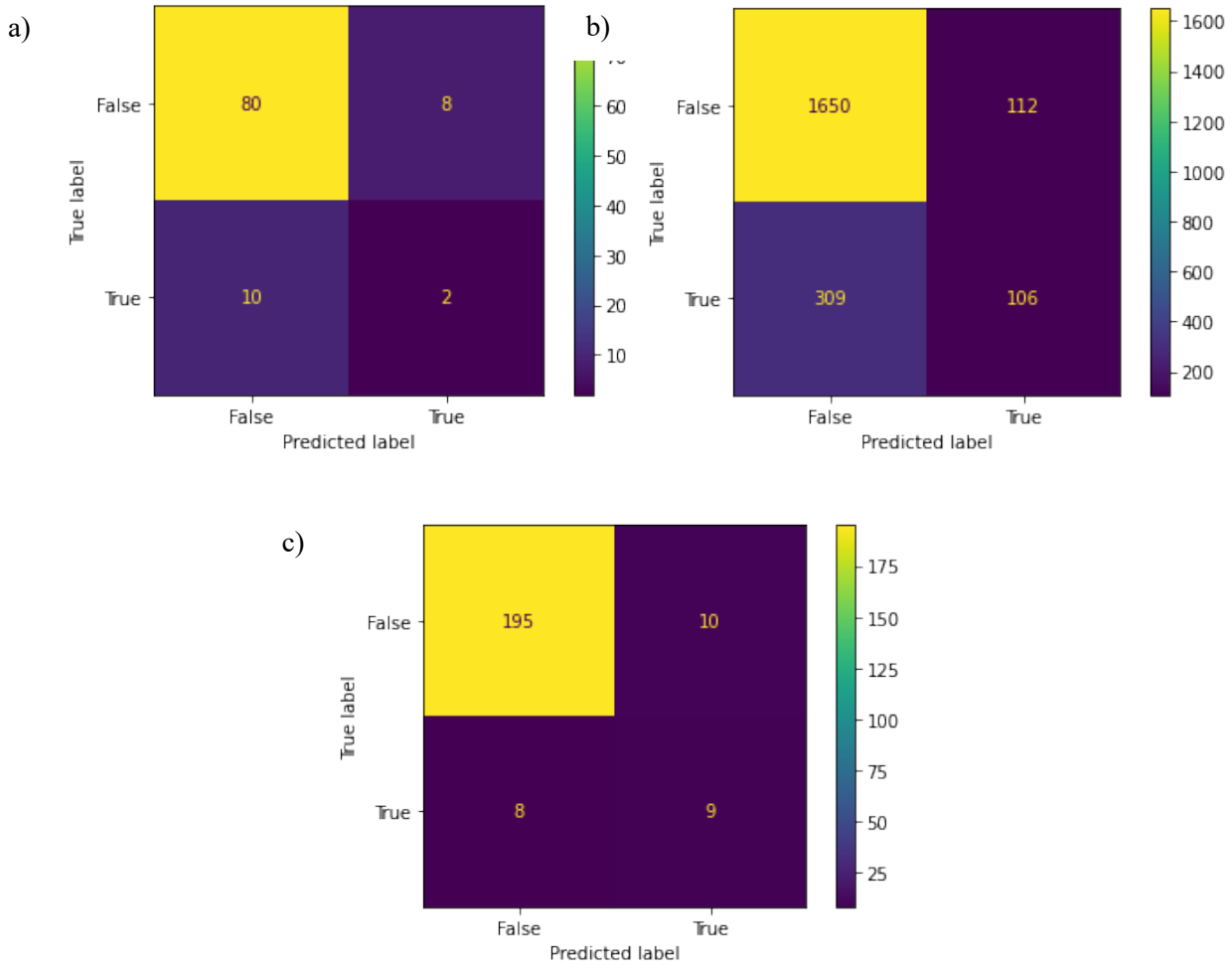

Figure 3. Confusion matrices of data sets. a) CM1, b) JM1 and c) PC1

When the results in Figure 3 were examined, the precision value obtained with the CM1 data set was 0.2, while the recall value was 0.16. The precision value of the JM1 data set was 0.48. In addition, the recall value is 0.25. In the PC1 data set, which is the most successful data set, a precision value of 0.47 was obtained, while a recall value of 0.53 was calculated. The F1-score is a better evaluation criterion than the accuracy, as it includes the harmonic mean of precision and recall values. When evaluated according to F1-scores, it was observed that the classifier was not successful. Contrary to other studies in the literature, it was observed that the BiLSTM model was ineffective. The main reasons for this situation may be due to parameters. Changing the parameter of the model or using different optimization methods can positively affect the performance of the method. In addition, the use of different deep learning models can make the classification process more

effective. Also, changing the dataset can increase the performance of the designed BiLSTM model. All these restrictions need to be considered.

5. CONCLUSION

In this study, software faults were predicted and BiLSTM deep learning model was used for this. The study consisted of four stages. In the first stage, data sets were determined, and data were collected. Three different data sets were used. After obtaining the data, the data were normalized, and Z-score normalization was used. Then, a deep learning model was designed, and the data were classified. In the final stage, the performance of the classifier was measured with accuracy, F1-score, and AUC scores. The lowest accuracy score was obtained with the JM1 dataset, and the value was 80.66%. The F1-score and AUC scores obtained from this data set were 33.00% and 0.60, respectively. Then, the highest accuracy score was observed in the CM1 dataset. While the accuracy score of this data set is 82.00%, the F1-score value is 17.00%. The AUC score of the CM1 data set was calculated as 0.70. At the end of the study, the highest accuracy, F1-score, and AUC score were obtained from the PC1 dataset. The accuracy score of this data set was calculated as 91.89%, while the F1-score and AUC scores were 49.82% and 0.84, respectively. Although the designed deep learning model did not make a very effective classification, it can be improved by changing its various parameters. The use of different data sets in future studies, the evaluation of different deep learning algorithms, the creation of a hybrid structure or the application of different pre-processing methods may increase the performance of this model.

REFERENCES

[1] Buckley, F.J., Poston, R., Software quality assurance, IEEE Transactions on Software Engineering, 10, 36-41, 1984.

[2] Al-Ashwal, D., Al-Sewari, E.Z., Al-Shargabi, A.A., A CASE tool for JAVA programs logical error detection: static and dynamic testing, International Arab Conference on Information Technology, 1-6, Werdanye, Lebanon, 2018.

[3] Rathore, S.S., Kumar, S., A study on software fault prediction techniques, Artificial Intelligence Review, 51, 255-327, 2019.

[4] Ahmed, R., Ali, A., Ahmed, N., Zamal, F., Shamrat, F.M.J.M., The impact of software fault prediction in real-world application: an automated approach for software engineering, 6th International Conference on Computing and Data Engineering, 247-251, Sanya, China, 2020.

[5] Menzies, T., Milton, Z., Turhan, B., Cukic, B., Jiang, Y., Bener, A., Defect prediction from static code features: current results, limitations, new approaches, Automated Software Engineering, 17, 375-407, 2010.

[6] Catal, C., Software fault prediction: a literature review and current trends, Expert Systems with Applications, 38, 4626-4636, 2011.

[7] Bhandari, G.P., Gupta, R., Machine learning based software fault prediction utilizing source code metrics, 3rd International Conference on Computing, Communication and Security, 40-45, Kathmandu, Nepal, 2018.

[8] Malhotra, R., Comparative analysis of statistical and machine learning methods for predicting faulty modules, Applied Soft Computing, 21, 286-297, 2014.

[9] Moeyersoms, J., Fortuny, E.J., Dejaeger, K., Baesens, B., Martens, D., Comprehensible software fault and effort prediction: a data mining approach, Journal of Systems and Software, 100, 80-90, 2015.

[10] Qasem, O., Akour, M., Software fault prediction using deep learning algorithms, International Journal of Open Source Software and Process, 10, 1-19, 2019.

[11] Pahal, A., Chillar, R.S., A hybrid approach for software fault prediction using artificial neural network and simplified swarm optimization, International Journal of Advanced Research in Computer and Communication Engineering, 6, 601-605, 2017.

[12] Shirabad, S.J., Menzies, T.J., The PROMISE repository of software engineering databases, School of Information Technology and Engineering, 2005.

[13] Alakus, T.B., Turkoglu, I., A comparative study of amino acid encoding methods for predicting drug-target interactions in COVID-19 disease**,** Studies in Systems, Decision and Control, 619-643, 2021.

[14] Alipanahi, B., Delong, A., Weirauch, M.T., Frey, B.J., Predicting the sequence specificities of DNA- and RNA-binding proteins by deep learning, Nature Biotechnology, 33, 831-838, 2015.

[15] Bayram, F., Automatic license plate recognition based on deep learning, Journal of Polytechnic, 23, 955-960, 2020.

[16] Aktas, A., Dogan, B., Demir, O., Tactile paving surface detection with deep learning methods, Journal of the Faculty of Engineering and Architecture of Gazi University, 35, 1685-1700, 2020.

[17] Baydogan, C., Alatas, B., Metaheuristic ant lion and moth flame optimization-based novel approach for automatic detection of hate speech in online social networks**,** IEEE Access, 9, 110047-110062, 2021.

[18] Kucuk, D., Arici, N., A literature study on deep learning applications in natural language processing, International Journal of Management Information Systems and Computer Science, 2, 76-86, 2018.

[19] Abdulrahman, A., Baykara, M., A comprehensive review for emotion detection based on EEG signals: challenges, applications, and open issues, Traitement du Signal, 38, 1189-1200, 2021.

[20] Toraman, S., Dursun, O.O., GameEmo-CapsNet: emotion recognition from single-channel EEG signals using the 1D capsule networks, Traitement du Signal, 38, 1689-1698, 2021.

[21] Zhu, W., Xie, L., Han, J., Guo, X., The application of deep learning in cancer prognosis prediction, Cancers, 12, 1-19, 2020.

[22] Hossain, M.S., Amin, S.U., Alsulaiman, M., Muhammad, G., Applying deep learning for epilepsy seizure detection and brain mapping visualization, ACM Transactions on Multimedia Computing, Communications, and Applications, 15, 1-17, 2019.

[23] Liu, G., Guo, J., Bidirectional LSTM with attention mechanism and convolutional layer for text classification, Neurocomputing, 337, 325-338, 2019.